MPHIL

Towards Understanding the Thermodynamic Properties of Magnesium Rich Minerals Using Atomistic Simulations

Tse, Joshua

Award date:
2018

Awarding institution:
University of Bath

Towards Understanding the Thermodynamic Properties of Magnesium Rich Minerals Using Atomistic Simulations

Joshua S Tse

A thesis presented for the degree of
Master of Philosophy

Department of Chemistry
University of Bath
22 September 2017

Contents

Abstract

The aim of this thesis is to use atomistic simulation to provide insight in to the structures and thermodynamic properties of magnesium rich mineral phases. The $MgO-H_2O-CO_2$ system has been chosen due to its relevance in the area of nuclear waste storage, where corroded Magnox cladding has formed a complex waste, mainly comprising of magnesium rich phases. Chapter 1 outlines previous experimental and computational research conducted, relevant to the identification and classification of Magnox nuclear sludge. A number of magnesium mineral phases have been identified that are likely to be present *e.g.* Brucite ($Mg(OH)_2$), Magnesite ($MgCO_3$), Hydromagnesite ($Mg_5(CO_3)_4(OH)_2.4H_2O$). Chapter 2 describes the computational methodology and validation of the simulation parameters used within this work.

The results are presented and discussed in Chapters 3 to 5, where Chapter 3 evaluates various DFT approaches for modelling magnesium phases and examines the effect of including van der Waals (vdW) forces using 3 different implementations. Results show that the inclusion of vdW is vital to obtaining an accurate representation of the structural and energetic properties of magnesium rich phases, particularly for the layered phases. Chapter 4 outlines a thermodynamic framework for producing high quality phase diagrams, where optB86b-vdW and optB88-vdW functionals compare well with the experimental phase diagram. All functionals produce similar phases diagrams, where each vdW correction has a constant shift in the pressures from experiment, potentially allowing for a correction factor to be determined. Chapter 5 presents the surface calculations and the interactions of Brucite surfaces with H_2O/CO_2 and radio-nuclei (^{90}Sr). It can be concluded that $\{100\}$ surfaces of Brucite displays evidence of being more reactive than $\{001\}$ surfaces. The stability of strontium defects is heavily dependent on the coordination that the surface ions can achieve. Additionally, ^{90}Sr only shows favourable adsorption on to the $\{001\}$ surface in the presence of CO_2 is also present. Finally, an overview of the conclusions and possible areas for future research can be found in Chapter 6.

Acknowledgements

I would first like to personally thank my supervisor, Professor Steve Parker who has been my inspiration during my time at the University of Bath, his support, encouragement, guidance and brilliant sense of humour has been invaluable and without which I would not have been able to complete my thesis. Secondly, I would like to express my gratitude to Dr Marco Molinari who personally drove me through both his constructive and demanding challenges, he kept me on the straight and narrow, even though I did not always deliver to his time scales.

In addition I would like to extend my sincere thanks to the Parker Group, especially Dr James Grant, for making me think outside the box and to persue my own thoughts and ideas whilst also sanity checking my methodologies. Joe, Andrew and Adam have also been instrumental in helping me on this journey, being friends, social drinking buddies, brilliant quiz champions and who have helped me with what have been sometimes constructive thoughts.

CCP5, MCC, Archer, and Bath HPC all of whom have supported me with resources and financial funding, my thanks goes to you all.

Finally thanks to my Mum and Dad who have supported me through thick and thin, along with my brother, wider family and friends, especially my late Auntie Carol who challenged my primary school headteacher who at one time questioned my ability, and my late Auntie Sandra who encouraged me from a young age to do my very best in everything. Also my thanks to Molly, Emlyn, Edie and Dickie who sadly are no longer with us to see my achievements.

"With magic, you can turn a frog into a prince. With science, you can turn a frog into a Ph.D and you still have the frog you started with."

Sir Terry Pratchett

1 Introduction

Factors controlling formation and surface properties of hydroxides and hydrated Magnesium rich (Mg-rich) phases are important for a wide range of applications, from waste products of nuclear storage, use as fire retardants [1] and dolomitic lime cement [2]. One example where an understanding of the effect of external conditions is critical and yet is extremely challenging to study is in the radioactive sludge derived from Magnox fuel, currently stored underwater at the Sellafield facility (UK). As the Magnox cladding corrodes, a complex waste forms, mainly comprising of Mg-rich phases and radio-nuclei [3, 4]. Characterisation of the waste is critical and currently poorly understood, hence it is not clear how to devise a safe and successful treatment strategies. The safe treatment of nuclear effluent is important, however, it is extremely expensive. The cost can be mitigated by understanding which phases are present and how they can be modified by adjusting the external conditions.

Atomistic simulations have not yet been fully exploited to investigate the effect of the storage conditions on the composition of Mg-rich phases. This work focuses on modelling the formation of Mg-rich mineral phases and investigates the interactions with an important radio-nuclide for one of the major phases.

1.1 Magnox Nuclear Reactors

The year 1956 marked the opening of the UK's first Magnox type reactor. The design was based on earlier prototype gas cooled reactors and continued to be built in the UK, until 1971, when they were superseded by a more efficient design [5, 6]. Magnox reactors are named after the alloy (Mg with 0.8 wt% Al and 50ppm Be [7]) used to encase the fissionable material. Originally, the reactor was designed with dual purpose; the generation of energy and the production of plutonium for use in nuclear devices [5].

Figure 1.1 is a schematic representation of a Magnox reactor and is comprised of a steel pressure vessel which is encased in concrete, to act as a radiation shield. In the reactor, uranium metal cores are encased in the Magnox alloy and the neutrons are moderated by graphite. The core is cooled by flowing CO_2 gas over the fuel elements, which in turn is used to generate steam to drive a turbine.

In order to achieve reasonable cost efficiency the operating temperature of the reactor needs to be significantly higher than other reactors. This in turn requires high pressures of coolant, increasing the risk associated with this reactor design and

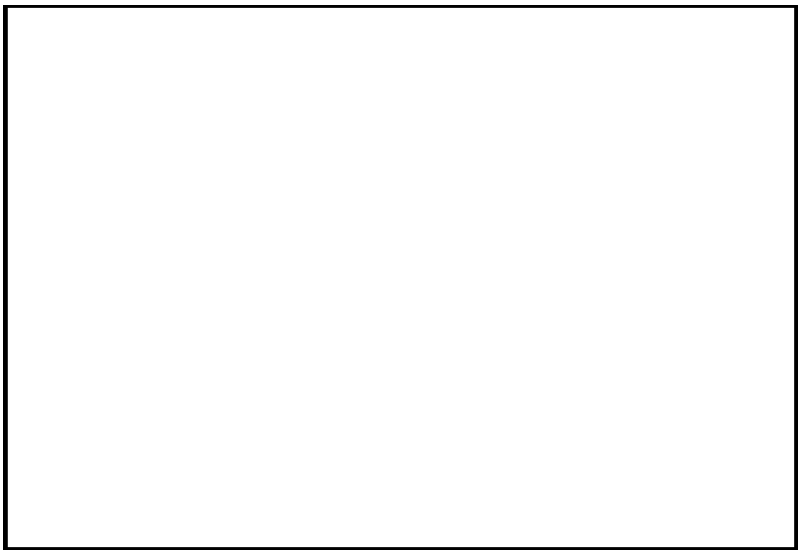

Figure 1.1: Magnox gas cooled reactor schematic [6].

consequently it has been superseded by liquid cooled reactors [8]. However, there is still the issue of legacy waste from Magnox reactors. Spent reactor cores need to first be stored under water until they have cooled. They are then able to be reprocessed [9]. Reprocessing involves removing the metal cladding and each component is separately processed to ensure safe disposal/storage.

1.2 Magnox Sludge

Spent Magnox reactor cores are currently being stored underwater at Sellafield. The ponds were constructed in 4 stages between 1960-1984 and have gradually been filled [3, 10, 11]. Poor record keeping between 1960-1980 has resulted in uncertainty as to the exact composition of the waste stored in the ponds [4, 10, 12]. Additionally, a lengthy shut-down of the Magnox reprocessing plant, led to a backlog of waste stored [12]. Prolonged storage has resulted in the corrosion of the Magnox cladding, producing large quantities of sludge (Figure 1.2), with uncertainty over its composition [10].

There are several major concerns for those monitoring the ponds. Firstly, the under water visibility is dramatically reduced [12] preventing visual inspection. The small sludge particles hinder the ability to filter the pond water to improve visibility. Secondly, corrosion of the Magnox cladding has exposed some of the uranium cores [4]. This has resulted in an increase to local radiation levels and release of radio-isotopes in to the pond system, increasing the risk of release in to the wider environment [4]. Studies have concluded that the majority of the radio-isotopes present are ^{137}Cs and ^{90}Sr [3, 4]. In an attempt to slow the corrosion of the Magnox cladding the ponds are being treated with sodium hydroxide, inducing raising the pH dramatically [4, 14]. The result is some of the most complex radiological and chemical waste that exists.

The storage facility is now long past its designed lifetime, which has resulted in

Figure 1.2: Magnox sludge sample [13].

questions on the structural integrity of the pond walls and an increased risk of radio-active material contaminating areas close to the plant [4]. Hence, the removal of the waste and decommissioning of the storage facility is considered to be of vital importance. However, before the removal process can begin the composition of the sludge needs to be identified and a detailed inventory of the pond needs to be conducted [13]. In order to obtain an inventory and location of Magnox reactor cores Jackson *et al.* [15] demonstrated a method to detect radiative sources. One method of locating the radiative sources is the rad-line gamma detector, which has been demonstrated to locate Magnox fuel rods with great success. This detector has the unique advantage of not requiring an electrical charge so can be fully submerged in water and has been shown to detect Magnox cores within 20 cm. Once the precise location of the fuel rods has been identified they can be removed, leaving the Magnox sludge behind.

The current approach focuses on removing the sludge and storing in stainless steel silos [11, 16]. Additionally Sellafield Ltd. has investigated suspending the Magnox sludge in grout before storing in the silos [11]. Once the sludge has been removed, the reactor cores can be reprocessed, which involves de-canning the uranium metal fuel rod from the Magnox cladding and processing both separately [12]. The decommissioning process for the first generation Magnox storage ponds has been estimated to take around 100 years to complete [4].

Sludge Mineral Phases

Due to the inherent risk associated with background radiation of the ponds, there are limited experimental studies using actual sludge samples [3, 10]. Work by Parry *et al.* [16] conducted an X-ray diffraction (XRD) analysis of a sludge sample. Results showed that the sludge in mainly compromised of Brucite ($Mg(OH)_2$) and Artinite ($Mg_2CO_3(OH)_2.3H_2O$). Further studies used environmental scanning electron microscope (ESEM) and energy-dispersive X-ray (EDX) methods to investigate the sludge [17], show that Brucite was the primary phase with smaller quantities of Hydrotalcite ($Mg_6Al_2(CO_3)(OH)_{16}.4H_2O$) and evidence of some Magnesium hydrated-carbonates. Overall, the sludge appears to be mainly comprised of Brucite with small quantities of Mg-carbonates.

Two different experimental approaches have been used to investigate the composition of sludge. The first method involves manufacturing non-radiative sludge samples from commercially available Brucite. Work by Blackburn *et al.* [18] has shown promising results in producing a sample with similar visual characteristics of Magnox sludge. The second method, takes the known pond conditions and then analyse the Mg phase diagram, at these conditions. However, due to the complexity of the phases present and the often slow kinetics of crystallisation, which is particularly evident for Magnesite ($MgCO_3$), this is still and area of active concern. Indeed, the slow kinetics may also be an important consideration for storage, as the solubility of a particular radio-nuclide in one mineral phase may be different in another phase. Thus if the solubility is lower in the phase that crystallises last, then it may lead to a greater release into the environment.

In the next sections we examine the previous work on the thermodynamic and kinetic data to identify the most likely mineral phases.

1.3 Thermodynamics of Mg-Rich Phases

Figure 1.3 shows two different experimental phase diagrams of Mg-rich phases at 1 bar p_{H_2O}, where solid lines represent phase transitions and dashed lines are metastable phases. Both phase diagrams build on the work of Langmuir *et al.* [19], but use new thermodynamic data to improve the phase diagram. Schott *et al.* [20] predicts that Magnesite is unstable and only forms at high p_{CO_2} and high temperatures. However, more recent studies have found that Magnesite is the most thermodynamically stable phase but is kinetically inhibited [21, 22]. The phase diagram of Schott also predicts a small region of Artinite that is not present in the phase diagram of Hill [22]. More recent work by Parry *et al.* [16] also shows it to be stable at certain conditions. Artinite is a rare low temperature phase of Mg, with limited thermodynamic data. It is difficult to verify whether Artinite's presence in the phase diagram is accurate, and demonstrates that there is still experimental uncertainty over the precise phase stability.

Computational modelling offers a safe alternative in characterising Magnox nuclear sludge. Chaka *et al.* [23] used density functional theory (DFT) to produce thermodynamic data of Mg-rich phases. This work outlines a thermodynamic framework that can be used to predict properties of Mg-rich phases. In testing this framework Chaka *et al.* concluded:

- The inclusion of zero point energy (ZPE) has a significant effect on the free energy and is vital to produce accurate thermodynamic data.
- There is a debate in the literature over the exact molecular formula for Hydromagnesite. DFT was used to examine the different proposed molecular formula for Hydromagnesite, concluding $4MgCO_3.Mg(OH)_2.4H_2O$ was accurate.
- Assessed the different thermodynamic properties reported for Lansfordite ($MgCO_3.5H_2O$), where the experimental entropy value ranges from $S°$=180.67-249.52 J/mol [20, 24, 25, 26], concluding that the reported value of $S°$=249.52 J/mol by

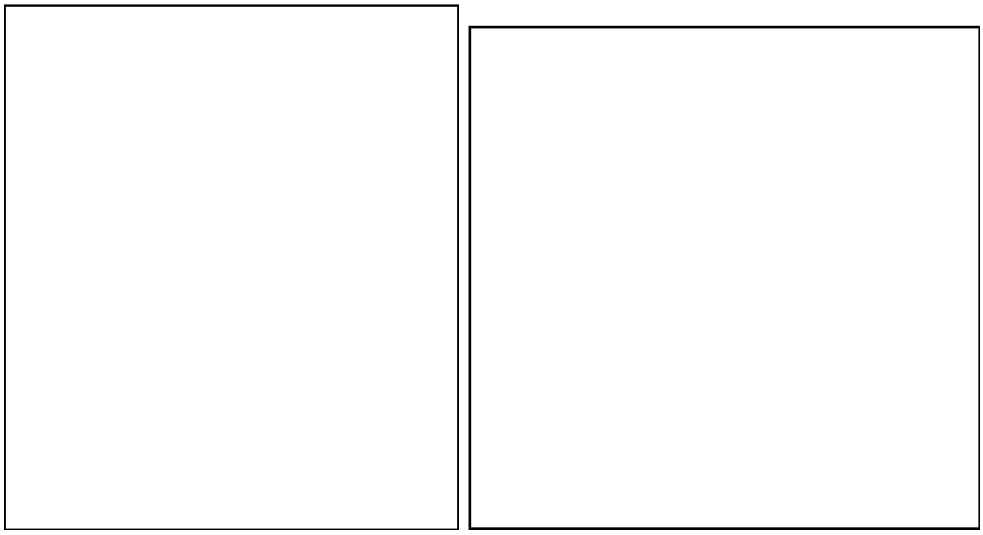

(a) Schott *et al.* [20] **(b)** Hill *et al.* [22]

Figure 1.3: Experimentally determined phase diagrams: Temperature vs - Log p_{CO_2}. Where solid and dashed lines represent thermodynamic and meta-stable phase transitions respectively.

Königsberger matches that obtained through DFT [25], showing that theory can provide clarity, where there is uncertainty in experimental data.

- The framework can also be used to predict properties of theoretical structures (*e.g.* Monohydromagnesite and Mg-Ikiate). Examination of these structures found that Monohydromagnesite was the least stable of all conformers and that Mg-Ikiate is very stable at low temperatures (0-275 K) but quickly destabilises when the temperature is increased. In both cases the instability is due to the decrease in the coordination that Mg can obtain (6-fold coordination), due to its smaller size, compared to Ca (8-fold coordination). The importance that coordination has on stability is extremely significant and is a dominate component of surface stability, where highly coordinated Mg surfaces are more stable. Computational approaches allows for an exploration of the properties of theoretical structures, providing a greater understanding of the system in question.

So far we have examined the literature for work on the thermodynamics of Mg-rich phases. However, as noted above kinetics play a large role in the formation of these minerals. Therefore, in the role of kinetics on formation for Mg-rich phases will be reviewed.

1.4 Kinetics of Mg-Rich Phases

Under CO_2-rich conditions, Magnesite is the most thermodynamic stable phase [27]. However, even if the external conditions favour the formation of Magnesite ($MgCO_3$) due to the poor kinetics of the formation [21] it is worth considering the reactions of other mineral products or intermediates as they will also be a signifi-

cant component of the sludge. Hence, in addition to studying the thermodynamic properties of Mg-rich phases, it is also important to understand the kinetic formation of different phases. Magnesite production has potential for CO_2 capture, due to its high theoretical carbon capacity (1:1 ratio of MgO:CO_2) [28], additionally it is non-toxic. Magnesite can be synthesized from silicate minerals (Serpentine $Mg_3Si_2O_5(OH)_4$, Olivine $(Fe, Mg)_2SiO_4$ and Forsterite Mg_2SiO_4) through various methods (*e.g.* direct and indirect) discussed in the following sections.

Direct Formation of Magnesite

The direct carbonation of silicates proceeds through a three step process: CO_2 dissolves in H_2O forming slightly acidic solution (Equation 1.1), followed by the dissociation of the silicate (Equation 1.2) and finally the precipitation of Magnesite (Equation 1.3). This method suffers from extremely slow reaction kinetics and with the high operating temperatures makes it impractical for industrial usage [29, 30].

$$CO_{2(g)} + H_2O_{(l)} \rightarrow H^+_{(aq)} + HCO^-_{3(aq)} \tag{1.1}$$

$$Mg - Silicates(s) + 2H^+_{(aq)} \rightarrow Mg^{2+}_{(aq)} + SiO_{2(s)} + H_2O_{(l)} \tag{1.2}$$

$$Mg^{2+}_{(aq)} + HCO^-_{3(aq)} \rightarrow MgCO_{3(s)} + H^+_{(aq)} \tag{1.3}$$

Indirect Formation of Magnesite

Alternatively, Magnesite can be generated through indirect methods, involving the formation of two or more Mg phases *e.g.* Periclase (MgO) or Brucite ($Mg(OH)_2$) from Mg-silicates before carbonating. Zevenhoven *et al.* [30] highlights an indirect reaction pathway for a lower energy synthesis of Magnesite from Serpentine [29]. First Serpentine is thermally decomposed to form Periclase (MgO) and SiO_2. Periclase is then hydrated to form Brucite. Finally, Brucite is carbonated forming Magnesite. Work by Schaef *et al.* [31] has shown how the formation of Magnesite from Brucite transitions via formation of Nesquehonite ($MgCO_3.3H_2O$). This method has been shown to have much faster reaction kinetics compared to direct methods with a much lower energy cost [29, 30], making it potentially attractive for industrial processes.

$$Mg_3Si_2O_5(OH)_{4(s)} \rightarrow 3MgO_{(s)} + 2SiO_{2(s)} + 2H_2O_{(l)} \tag{1.4}$$

$$MgO_{(s)} + 2H_2O_{(l)} \rightarrow Mg(OH)_{2(s)} \tag{1.5}$$

$$Mg(OH)_{2(s)} + CO_{2(g)} \rightarrow MgCO_{3(s)} + H_2O_{(l)} \tag{1.6}$$

HCl Extraction

Forsterite and Serpentine have been demonstrated to dissolve in HCl, which is an effective method for extracting Mg from Mg-Silicate minerals [28, 29, 32, 33, 34, 35]. Both minerals react exothermically in a rapid reaction forming magnesium chloride (Equation 1.7). Some of the HCl can be recovered through heating the solution to temperatures of 200-300 ℃. At these temperatures the hydrated magnesium chloride becomes unstable and dissociates (Equation 1.8) [34].

$$Mg_2SiO_{4(s)} + 4HCl \rightarrow 2MgCl_2 + 2H_2O + SiO_2 \tag{1.7}$$

$$MgCl_2.H_2O \rightarrow Mg(OH)Cl + HCl_{(g)} \tag{1.8}$$

Dissolving the mono-hydroxide in water will form magnesium chloride and Brucite (Equation 1.9). Brucite can now be used to remove CO_2 and form Magnesite (see Equation 1.6). $MgCl_2$ can be recycled back in to Equation 1.7, recovering the majority of the HCl. However, the energy required to loop the reaction and the cost associated with the evaporation of the solvent, makes this method impractical for use industrially, as overall it produces more CO_2 than it captures [36].

$$2Mg(OH)Cl \rightarrow MgCl_2 + Mg(OH)_2 \tag{1.9}$$

Alternatively, Noranda's process [37] can be used to produce anhydrous magnesium chloride. This involves sustaining a high pressure of HCl over the hydrated chloride melt [34, 37], followed by the evaporation of the excess solvent producing anhydrous $MgCl_2$. This can then undergo a reaction with Na_2CO_3 to form a range of hydrated Magnesium Carbonates, via variation in the p_{CO_2} and temperature. At 25℃ and 1 bar p_{CO_2} Nesquehonite is the primary product. Increasing the temperature to 120 ℃ and p_{CO_2} to 3 bar forms Hydromagnesite, which decomposes to form Magnesite with 5-15 hours. Finally, keeping the temperature at 120℃ and increasing p_{CO_2} to 100 bar results in the direct formation of Magnesite [32, 33]. However, due to the high temperatures and long time scale, this method is also impractical for industrial applications.

Reaction with Salt Brine

Periclase is being trialled for use in nuclear waste isolation plants in the USA, as a barrier to absorb excess CO_2 produced from the degradation of organic materials [38]. The interaction of Periclase and Brucite with varying salt brine solutions has been investigated to determine how the complex interactions lead to different Mg-rich phases being formed, under varying p_{CO_2} [39]. They have found that by varying the composition of the salt solutions and p_{CO_2}, different Mg-rich phases can be formed. At atmospheric p_{CO_2}, the reaction with Na-Cl based brine solutions proceed according to Equation 1.10.

$$\underset{\text{Periclase}}{MgO} \rightarrow \underset{\text{Brucite}}{Mg(OH)_2} \longrightarrow \underset{\text{Hydromagnesite}}{Mg_5(CO_3)_4(OH)_2.4H_2O} \tag{1.10}$$

Decreasing the $p_{CO_2} = 5 \times 10^{-2}$ atm, induces a secondary reaction forming Nesquehonite (Equation 1.11).

$$\begin{array}{ccccc} \underset{\text{Periclase}}{MgO} & \rightarrow & \underset{\text{Brucite}}{Mg(OH)_2} & \longrightarrow & \underset{\text{Hydromagnesite}}{Mg_5(CO_3)_4(OH)_2.4H_2O} \\ & & \searrow & & \\ & & \underset{\text{Nesquehonite}}{MgCO_3.3H_2O} & & \end{array} \tag{1.11}$$

Changing the brine solution to be comprised of mainly Mg-Na-Cl ions (*e.g.* Generic Weep Brine) at atmospheric p_{CO_2} causes the reaction to follow the pathway in Equation 1.12. Where formation of $Mg_3(OH)_5Cl.4H_2O$ can be induced by increasing the pH of the solution.

$$\begin{array}{ccccc} \underset{\text{Periclase}}{MgO} & \rightarrow & \underset{\text{Brucite}}{Mg(OH)_2} & \longrightarrow & \underset{\text{Hydromagnesite}}{Mg_5(CO_3)_4(OH)_2.4H_2O} \\ & \searrow & \downarrow & & \\ & & Mg_3(OH)_5Cl.H_2O & & \end{array} \tag{1.12}$$

Using the brine solution comprised of mainly Mg-Na-Cl ions and decreasing the $p_{CO_2} = 5 \times 10^{-2}$ atm changes the reaction back to that shown in Equation 1.10. This demonstrates that varying the p_{CO_2} results in the formation of different Mg-rich phases. Within the time-scale for the nuclear waste isolation all products may decompose to form Magnesite. However, in the interim time period kinetically stabilised products will form, depending on the storage conditions. Understanding which metastable phases form and there interactions can inform a long term storage plan.

1.5 Aims of Thesis

In summary from Chapter 1 a number of key magnesium mineral phases have been identified and are likely to be present *e.g.* Brucite ($Mg(OH)_2$), Magnesite ($MgCO_3$) and Hydromagnesite ($Mg_5(CO_3)_4(OH)_2.4H_2O$). The background radiation associated with the nuclear waste storage plant, acts as a barrier to experimental investigations. The use of computational techniques offers an alternative approach. Therefore, the work described in this thesis will use DFT to model the structure and stability of known crystalline phases for the $MgO - CO_2 - H_2O$ system and how external conditions modify their relative stability. Using ^{90}Sr as an example, begin to predict the effect of external conditions on radio-nuclei solubility.

The main goals are:

- Establish whether the standard DFT approach (PBE) is sufficient for the modelling of Mg-rich phases and examine the effect of including van der Waals (vdW) forces.
- Outline a thermodynamic framework for use in producing phase diagrams, and assess their accuracy when compared to experiment.
- Use the framework to determine thermodynamically stable phases under a range of conditions relevant to Magnox sludge storage.
- Extend the capability of the framework to predict surface phase diagrams.
- Begin to identify the effect of radio-nuclei on surface stability, using ^{90}Sr as a model system.

Chapter 2 describes the computational methodology and validation of the simulation parameters used within this work. The results of the simulations are presented as follows; bulk comparison of different DFT functionals for the inclusion of vdW interactions, for magnesium oxides hydroxides and carbonates (Chapter 3). A thermodynamic framework is outlined and applied to produce bulk phase diagrams (Chapter 4). Chapter 5 presents the surface calculations and the interactions of the surfaces with H_2O/CO_2 with the chosen radio-nuclei ^{90}Sr. Finally, the thesis is concluded with a summary of the major conclusions and possible areas for future development (Chapter 6).

2 Methodology

The computational simulation of atomic systems, can generally be categorised into two approaches: classical and quantum mechanical methods. Classical methods use a set of parametrised equations to describe the energy of interactions between atoms, and the parameters can be derived by fitting to experimental and/or QM data *e.g.* lattice parameters, bulk modulus and energies. By not treating the electrons explicitly it is possible to simulate a large number of atoms relatively quickly if the derived parameters are reliable then the approach can represent real system.

Quantum mechanical (QM) methods predict properties by explicitly simulating the electrons. QM calculations in principle, only require an initial structure, which is considerably less information than classical methods. However, QM methods have a much longer simulation time per atom compared to classical methods and hence generally only applied to smaller simulation cells. This work focuses primarily on QM methods and therefore this chapter will describe the methods used throughout this work.

2.1 Quantum Theory

Quantum theory can be expressed through the time independent Schrödinger equation. Where $\hat{H}$ is the Hamiltonian operator, E is the total energy and Ψ is the wave-function for system.

$$\hat{H}\Psi = E\Psi \tag{2.1}$$

The Hamiltonian can be split in to nuclear and electronic components. Where $\hat{T}_{\mathrm{n}}$, $\hat{T}_{\mathrm{e}}$ are the nuclei and electron kinetic operators and $\hat{V}_{\mathrm{nn}}$, $\hat{V}_{\mathrm{ee}}$ and $\hat{V}_{\mathrm{ne}}$ are the potential operators for nuclei-nuclei, electron-electron repulsion and nuclei-electron interactions.

$$\hat{H} = \hat{T}_{\mathrm{n}} + \hat{T}_{\mathrm{e}} + \hat{V}_{\mathrm{nn}} + \hat{V}_{\mathrm{ee}} + \hat{V}_{\mathrm{ne}} \tag{2.2}$$

It is only possible to solve Equation 2.2 for two body systems, as $\hat{V}_{\mathrm{ee}}$ hinders the many body interactions from being calculated. However we can use the Born-Oppenheimer (BO) approximation to decouple the electronic and nuclear degrees of freedom. The BO approximation states that the nuclei and electron degrees of freedom can be treated separately. This is based on the fact that the nuclei have far greater masses

than electrons. Therefore, it can be assumed that the nuclei are stationary with respect to the electrons and can now be treated as part of the external potential in the form of point charges,

$$\hat{H} = \hat{T}_{\mathrm{e}} + V_{\mathrm{ext}}(R_i) + \hat{V}_{\mathrm{ee}} \tag{2.3}$$

where V_{ext} is the external potential imposed by the nuclear positions (R_i).

2.1.1 Density Functional Theory

Density functional theory (DFT) was first developed by Thomas [40] and Fermi [41] and is a method in which Schrödinger's equation and the N-electron wave function are replaced with the electron density. This effectively reduces the calculation from 4N degrees of freedom ($(r_1, s_1; ... : r_N, s_N)$ for every electron (N)) to only the 3 spatial parameters (r_x, r_y, r_z) (Equation 2.4).

$$\rho(\vec{r}) = |\Psi(r_1, s_1; ... : r_N, s_N)|^2 \tag{2.4}$$

DFT was further developed by the work of Hohenberg and Kohn [42]. Their pivotal work is outlined in two key theorems. The first theorem states that the external potential (v_{ext}) is a unique functional of the electron density. As v_{ext} forms part of the Hamiltonian, the wave function Ψ is also a unique function of electron density. Hence, all the ground state properties can be determined with respect to electron density. The second theorem proposes a functional in which the electron density can be used to calculate the total electron energy (Equation 2.5).

$$E[\rho] = \int \nu_{\mathrm{ext}}(r)\rho(r)\delta r + F[\rho(r)] = E_{\mathrm{ne}}[\rho(r)] + F[\rho(r)] \tag{2.5}$$

Where $E_{\mathrm{ne}}[\rho(r)]$ is the energy of nuclear-electronic interaction and is shown to form part of the external potential $\nu_{\mathrm{ext}}(r)$ in Equations 2.2 to 2.3. $F[\rho(r)]$ is known as Hohenberg-Kohn functional and is defined as the kinetic energy $T[\rho(r)]$ plus the electron-electron interactions $E_{\mathrm{ee}}[\rho(r)]$ (Equation 2.6). This functional calculates the true electronic energy only when the input density matches the true ground state density. It is important to note that no approximations have been made to get to this stage.

$$F[\rho(r)] = T[\rho(r)] + E_{\mathrm{ee}}[\rho(r)] \tag{2.6}$$

2.1.2 Kohn-Sham

Work by Kohn-Sham moves beyond the limitations of the Hohenberg-Kohn theory and improves the accuracy of DFT. This is achieved by imaging a fictitious set of non-interacting electrons that have the same density as the real system. The fictitious reference system recreates the same ground state energy, as the interacting

system, when given the true ground state electron density. The main issue of the Hohenberg-Kohn theory is that we do not know $F[\rho(r)]$, Kohn-Sham suggest that the functional can be expressed by Equation 2.7.

$$F[\rho(r)] = T_{\text{Ref}}[\rho(r)] + J[\rho(r)] + E_{\text{xc}}[\rho(r)] \tag{2.7}$$

Where $T_{\text{Ref}}[\rho(r)]$ is the kinetic energy for a system of non-interacting electrons, $(J[\rho](r))$ is the Coulomb interaction (Equation 2.9) and $E_{\text{xc}}[\rho(r)]$ is the exchange correlation energy (Equation 2.7). The kinetic energy of this fictitious system is not the same as the real system, as only the known components are calculated. The rest of the kinetic energy is approximated and is incorporated in to the exchange correlation energy.

$T_{\text{Ref}}[\rho]$ is expressed in Equation 2.8. Where φ_i are the Kohn-Sham orbitals containing non-interacting electrons.

$$T_{\text{Ref}}[\rho(r)] = -\frac{1}{2}\sum_{i=1}^{N}\int \varphi_i^* \bigtriangledown^2 \varphi_i \delta r \tag{2.8}$$

The second term in Equation 2.7 is the Coulomb interaction $(J[\rho](r))$ and is defined in the Equation 2.9.

$$J[\rho(r)] = \frac{1}{2}\int\int \frac{\rho(r_1)\rho(r_2)}{|r_1 - r_2|}\delta r_1 \delta r_2 \tag{2.9}$$

The final term in Equation 2.7 is the exchange correlation energy $E_{\text{xc}}[\rho(r)]$. This term contains all the exchange and correlation interactions and also includes the difference in kinetic energy between the reference and real systems (Equation 2.10). Where $E_{\text{ncl}}[\rho]$ is a non-classical contribution containing the exchange and correlation interactions.

$$\begin{aligned} E_{\text{xc}}[\rho(r)] &= (T[\rho(r)] - T_{\text{Ref}}[\rho(r)]) + (E_{\text{ee}}[\rho(r)] - J[\rho(r)]) \\ &= T_{\text{Corr}}[\rho(r)] + E_{\text{ncl}}[\rho(r)] \end{aligned} \tag{2.10}$$

Combining Equations 2.5, 2.8 and 2.9 we get a complete expression for the energy of a Kohn-Sham system (Equation 2.11). All unknown properties are now contained in the exchange correlation energy $E_{\text{xc}}[\rho(r)]$.

$$E_{\text{KS}}[\rho(r)] = T_{\text{Ref}}[\rho(r)] + J[\rho(r)] + E_{\text{xc}}[\rho(r)] + E_{\text{ne}}[\rho(r)] \tag{2.11}$$

The electron density can be defined as the sum of the squares of the non-interacting orbitals (KS-orbitals) (Equation 2.12).

$$\rho(r) = \sum_{i=1}^{N} |\varphi_i(r)|^2 \tag{2.12}$$

As the Kohn-Sham orbitals contain only non-interacting electrons, it is possible to solve them independently. This is done through a Schrödiner like Kohn-Sham equation (Equation 2.13). An initial 'guess' for the electron density can now be used to to generate a set of Kohn-Sham orbitals (φ). These Kohn-Sham orbitals can then be used in Equation 2.12 to generate a new density closer to the true ground state density. This process is then repeated until convergence of the density is achieved. The total electronic energy can now be calculated using the true ground state electron density (ρ) using Equation 2.11.

$$\left[-\frac{1}{2} \bigtriangledown_i^2 + \nu_{\text{Ref}}(r) \right] \varphi(r_i) = \varepsilon_i \varphi_i \tag{2.13}$$

The final requirement is to generate a reference potential $\nu_{\text{Ref}}(r)$, which accurately produces the same electron density as the real system. From Equation 2.13 ε_i is the orbital energy and $\nu_{\text{Ref}}(r)$ is the reference potential which is calculated using Equation 2.14.

$$\nu_{\text{Ref}}(r) = \nu_{\text{ext}}(r) + \int \frac{\rho(r')}{|r - r'|} \delta r' + \nu_{\text{xc}}(r_i) \tag{2.14}$$

The exchange correlation functional $\nu_{\text{xc}}[r]$ defined in Equation 2.15.

$$\nu_{\text{xc}}(r) = \frac{\delta E_{\text{xc}}[\rho(r)]}{\delta \rho(r)} \tag{2.15}$$

Finally the only thing left to do is choose an approximation method for calculating the exchange correlation energy, which will be discussed in the next section.

2.1.3 Exchange-Correlation Functional

As defined in the previous section, the exchange correlation functional contains all the exchange and correlation interactions, and also includes the difference in kinetic energy between the reference and real systems. All unknown properties are now contained in the exchange-correlation functional and as such an accurate approximation is required. There are many different approximation methods for calculating the exchange-correlation functional. However, most modern functionals use either local density approximation (LDA) or the generalised gradient approximation (GGA), which is an extension to LDA.

Local Density Approximation

LDA is the simplest approximation of the exchange-correlation functional and is based on a uniform electron gas model, where the electron density is homogeneous over all space. Therefore, the total exchange-correlation energy can be obtained through integrating over all space (Equation 2.16),

$$E_{\mathrm{xc}}^{\mathrm{LDA}}[\rho(r)] = \int \rho(r)\varepsilon_{\mathrm{xc}}[\rho(r)]\delta r \tag{2.16}$$

where $\varepsilon_{\mathrm{xc}}[\rho(r)]$ is the exchange-correlation energy as a function of density for the uniform electron gas. The LDA approximation method assumes that the exchange-correlation energy is the same as the homogeneous electron gas of the same density. LDA is defined as being local and solely dependent on the density at point (r). This would require the density of the system to vary slowly, which is generally not the case in highly correlated systems (*e.g.* metals and semiconductors). Thus, LDA generally over-binds, leading to an overestimate of the binding energies and shorter bond lengths.

Generalised Gradient Approximation

GGA is an extension to LDA and incorporates the gradient of the density in the exchange-correlation functional and hence accounts for some of the inhomogeneity of the system.

$$E_{\mathrm{xc}}^{\mathrm{GGA}}[\rho] = \int \rho(r)\varepsilon_{\mathrm{xc}}^{\mathrm{GGA}}[\rho(r)]\delta r + \int F_{\mathrm{xc}}[\rho(r), \bigtriangledown\rho(r)]\delta r \tag{2.17}$$

Where F_{xc} is a correction which depends on both the gradient of the density. There are several different methods in which F_{xc} can be determined, resulting in many function being proposed in the literature. F_{xc} can be calculated via either fitting to experimental data of rare gas atoms (PW91) [43] or via a functional in which all components are computationally calculated (PBE) [44]. These functionals generally underbind and overestimate the bond lengths. In general GGA functionals outperform LDA functions, however, this varies depending on the system being modelled.

2.1.4 Van der Waals

LDA and GGA are considered to be local functionals and do not accurately represent van der Waals forces (vdW). These interactions arise from the shifting of charge distributions. This work compares two different approaches (DFT-D and vdW-DF) of including vdW interactions and will now discuss these in more detail.

DFT-D

The first technique, is a simple additive correction, applied to the Kohn-Sham energy (Equation 2.18),

$$E = E_{\mathrm{KS}} + E_{\mathrm{disp}} \tag{2.18}$$

where the E_{disp} is the energy of dispersion for the system and is calculated using Equation 2.19

$$E_{\text{disp}} = -\frac{1}{2}\sum_{A\neq B}\sum_{n=6,8,10,\ldots} s_n \frac{C_n^{AB}}{R_{AB}^n} + f_{\text{damp}}(R_{AB}) \tag{2.19}$$

where C_n^{AB} is the n^{th} order dispersion coefficient for the atom pair AB, R^n is the intermolecular distance and s_n is a scaling factor used to adjust the correction to repulsive behaviour. Finally f_{damp} is the damping function, which determines the short range behaviour of the dispersion correction and is fitted to both experimental and *ab initio* data. In this work we only use the implementation of Grimme D3 [45].

vdW-DF

The van der Waals density functional developed by Dion *et al.* [46], calculates the non-local contributions directly from the electron density. In VASP [47] the method is implemented using the algorithm of Roman-Perez and Soler [48]. The exchange correlation energy is now represented by Equation 2.20. Where E_c^{nl} is the non-local correlation energy and is expressed in terms of a density-density interaction formula.

$$E_{\text{xc}} = E_x^{\text{GGA}} + E_c^{\text{LDA}} + E_c^{\text{nl}} \tag{2.20}$$

Work by Klimes *et al.* [49, 50] proposes two different optimised vdW-DF functionals, which modify the way the exchange energy is calculated. The functional optB86b uses the theoretically derived, Becke 86b functional [51] to calculate the exchange energy. Whereas, optB88 is based on the experimentally fitted Becke 88 functional [52]. In this work we evaluate both optB86b [50] and optB88 [49].

2.2 Practical Implementation of DFT

This section will describe the practical considerations that are required when using DFT to study solid state systems.

2.2.1 Periodic Boundary Conditions

Periodic boundary conditions is a commonly used method in computational simulation and can be applied to a variety of different methods. Periodic boundary conditions work by surrounding a single simulation cell with images of itself. This allows infinite systems to be modelled with only a single cell simulated.

Figure 2.1 shows how 2D periodic boundary conditions work, where if a particle in the simulation cell moves in a direction, the same species in all other cells moves in an identical manner. If the blue particle was to leave the simulation cell through the top, an image of the blue particle enters from the opposite side. Periodic boundary conditions can be applied in different dimensions depending on the system that is

being modelling, for example 1D boundary for polymers, 2D boundaries for surfaces/slabs and 3D boundary for a crystal. This work uses 3D boundary conditions to simulate both surfaces and bulk structures.

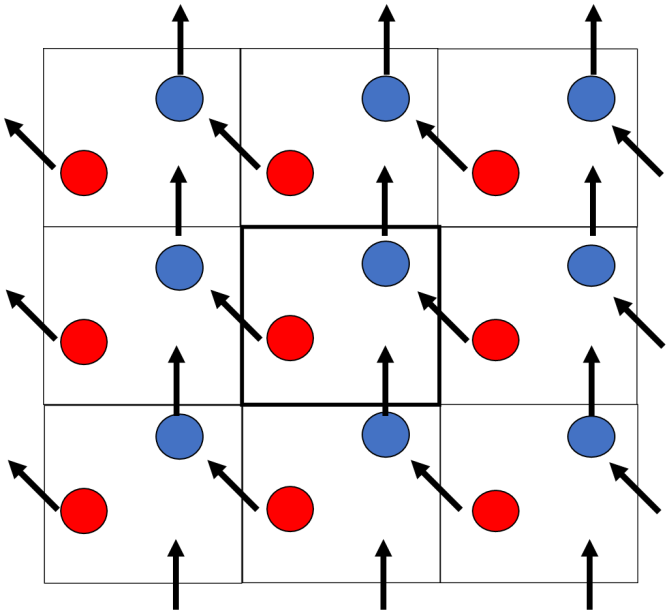

Figure 2.1: 2D Periodic Boundary Conditions. The simulation cell shown in bold and black arrows represent the movement of particles out and in to the simulation cell.

2.2.2 Reciprocal Lattice

The reciprocal lattice is a representation of the real lattice defined in reciprocal space, where the reciprocal lattice vectors (a^*, b^*, c^*) are related to the real space lattice vectors (a,b,c) through Equation 2.21.

$$a^* = 2\pi\frac{b \times c}{a.b \times c}; \quad b^* = 2\pi\frac{a \times c}{b.a \times c}; \quad c^* = 2\pi\frac{a \times b}{c.b \times c} \tag{2.21}$$

The primitive reciprocal lattice is known as the first Brillouion zone (BZ). Within the volume of the first BZ a complete description of the wave function can be produced. Once, a complete description of the wave function has been calculated then all ground state properties can be extrapolated.

2.2.3 Plane-wave Basis Sets

When simulating an infinite solid there are two main issue, in solving the Schrödinger equation. The first being that there will be an infinite number of wave functions to describe the infinite number of electrons. secondly, as each function is spread across the entire lattice, you need an infinite basis set to describe it. These limitations can be overcome through using Bloch theorem. Bloch theorem states that the Ψ of an electron in a periodic potential may be expressed as a Bloch Wave (Equation 2.22),

$$\Psi_i(r) = e^{(ik.r)} f_i(r) \tag{2.22}$$

where k is the wave vector, within the first BZ and represents the direction and wavelength of the Bloch wave and $f_i(r)$ is the cell periodic wave function and can be calculated from a plane wave basis set through Equation 2.23,

$$f_i(r) = \sum_G c_i, G \exp^{iG.r} \tag{2.23}$$

where G is the wave vectors and represents all possible translations to identical lattice points. The first issue can now be overcome by truncating the infinite plane wave basis set to only include plane waves with a kinetic energy less than a cut-off energy. Practically this cut-off energy is determined through convergence testing, where the cut-off energy is increased until it has minimal effect on the wave function. This is possible as plane waves with higher kinetic energy have minimal contribution to the wave function, so therefore can be excluded.

The second consideration is that it would be desirable to have an infinite number of k-points over the first BZ. This would result in an infinite number of vectors that need to be considered. However, wave-functions which are close together in k-space are nearly identical. Therefore, they can be represented by a single k-point. The denser the distribution of k-points the smaller the error, where the k-point density is practically determined through convergence testing.

In this work the k-points are distributed using the Monkhorst-Pack scheme. This scheme distributes k-points homogeneously in the BZ, centred on the Γ-point through Equation 2.24.

$$k = x_1 a^* + x_2 b^* + x_3 c^* \tag{2.24}$$

Where a^*, b^*, c^* are the reciprocal lattice vectors and x_i depends on the folding parameter, n_i (Equation 2.25).

$$x_i = \frac{l}{n_i} \qquad l = 1, ..., n_i \tag{2.25}$$

The density of the k-point mesh is dependent on the system being modelled. Conducting materials require a more dense mesh to fully represent there properties compared to insulating materials. Additionally, to maintain a constant k-point density, larger systems have a smaller reciprocal lattice and hence, require a smaller folding parameter to generate the same density. The choice for the folding parameter used in this work is discussed in Section 2.4.

2.2.4 Pseudo-potentials

Valence electrons are responsible for bonding and properties, hence, we are primarily interested in accurately representing them. Where as, core electrons close to the

nucleus have a Ψ which varies greatly spatially. This would require a large number of plane waves to accurately represent the wave function close to the core. However, they are stable in time and against external perturbation, overall charge and dispersion *i.e.* they do not respond much to changes in their environment. Therefore, pseudo-potentials replace the true potential, so that the core electrons are represented by a smooth slowly varying potential with fewer nodes, while the valence electrons are considered explicitly represented (Figure 2.2). This significantly reduces the number of plane waves required to reproduce the Ψ and thus reducing the computational cost of the calculation.

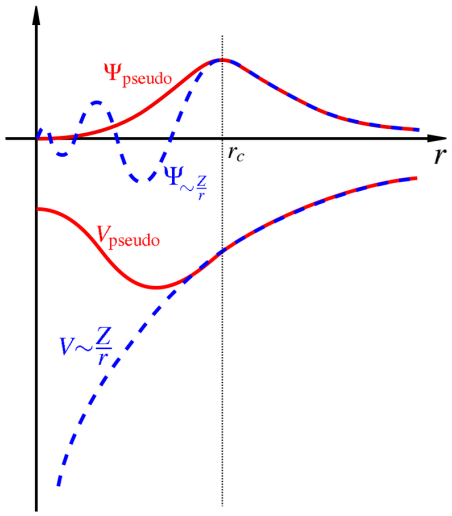

Figure 2.2: Schematic showing the all-electron (blue) and pseudo (red) for the potentials (ν) and wave function (Ψ) [53].

Pseudo-potentials are generally derived from all electron atomic calculations and can be defined by softness, which is a measurement of the smoothness and magnitude of the cut-off radius. Soft pseudo-potentials need fewer plane waves, however, this results in a larger cut-off radius, decreasing the atomic accuracy making the calculation less transferable. This work uses the PAW pseudo-potential method [54].

2.3 Energy Minimisation

Energy minimisation (EM) is one of the three primary methods used to calculate the ground state energy of a structure. The other two are molecular dynamics and Monte Carlo, however, this work exclusively uses the EM approach. EM calculates the forces between atoms to adjust their atomic positions and decrease the structures energy. In this work we use the *ab initio* implementation of EM, using the VASP code [47]. The latest methods of implementing EM give good agreement with experimental crystal structures, however, there are several issues that must be considered.

- Requires a starting structure, which is close to the real structure. Usually requires some experimental data, which can introduce bias in the simulation.

- The process of EM only goes 'down hill' and finds the closest minima. If there are multiple minima then there is a high probability of only finding the local minima.
- EM does not consider the vibrational contribution. Therefore, simulations are calculated at 0K and neglect the zero point energy.

EM can be split in to two different approaches, those that use derivatives and those that do not.

2.3.1 Steepest Descent Minimisation

Steepest decent minimisation is the simplest first order method. Where each step moves parallel to the net force, which corresponds to going straight 'downhill'.

$$r_{i+1} = r_i + \alpha_i s_i \tag{2.26}$$

$$s_i = \frac{-g_i}{|g_i|} \tag{2.27}$$

Where r_i is the starting positions, s_i is the gradient vector, g_i is the gradient and α_i is the step length for step i. The choice of α_i is very important, if α_i is too small then calculation takes too long. However, if α_i is too large then there is a chance of going past the minimum and never reaching convergence.

2.3.2 Conjugate Gradient Minimisation

Conjugate gradient is the logical next step after steepest decent method. The initial step for a conjugate gradient minimisation is the same as steepest decent. However, all following steps are dependent on the information calculated in the previous step. Where the gradient vector (s_i) is now calculated using Equation 2.28

$$s_i = -g_i + \gamma_i s_{i-1}; \quad \text{Where} \quad \gamma_i = \frac{g_i \cdot g_i}{g_{i-1} \cdot g_{i-1}} \tag{2.28}$$

The gradient vector now considers both s_i and g_i from the previous step. This enable the convergence of structures, regardless of the shape of the potential surface. An added benefit of this approach is the increased efficiency over steepest decent. This results in an efficient EM technique.

2.3.3 Newton Raphson Minimisation

Newton Raphson minimisation uses both the first and second derivative of the lattice energy. This is more efficient than first derivative approaches, with convergence

being reached in fewer steps. However, each step requires substantially more computational resource. Taking a Taylor expansion of the lattice energy (U_L) to the second derivative we get the Equation 2.29.

$$U_L(r + \delta r) = U_L(r) + \frac{\delta U_L(r)}{\delta r}\delta r + \frac{1}{2!}\frac{\delta^2 U_L(r)}{\delta r^2}\delta r^2 + K \tag{2.29}$$

Increasing the number of terms in the Taylor expansion increases the accuracy of the lattice energy, where K represents further expansion to higher order terms. This can now be used to calculate a new set of lattice coordinates from an initial positions (Equation 2.30).

$$r_i = r_{i-1} - \frac{U'_L}{U''_L} \tag{2.30}$$

Where U'_L is the gradient (g_i) and U''_L is the curvature or alternatively known as the Hessian matrix (W_{i-1}). This process is repeated iteratively until convergence is reached *i.e.* when $g_i = 0$. One of the major flaws with this method is the lack of accuracy when the initial guess is far from the real value and results in pour convergence or it can fail to find the minimum. Practically this can be overcome by combining conjugate gradient for the first few steps with Newton Raphson. This produces a more robust minimisation technique.

2.3.4 Quasi-Newton Minimisation

The problem with DFT codes is that the analytical calculation of the second derivative or Hessian is normally to CPU costly. Hence, codes such as VASP use Quasi-Newton, which is a simplified version of the Newton-Raphson method, where the Hessian matrix is approximated.

There are a number of different implementations of the Quasi-Newton method, Davidon-Fletcher-Powell (DFP) [55], Broyden-Fletcher-Goldfarb-Shanno (BFGS) [56, 57, 58, 59] and the RMM-DIIS [60]. The DFP formula for updating the Hessian matrix:

$$W_i^{-1} = W_{i-1}^{-1} + \frac{\delta r \times \delta r}{\delta r.\delta g} - \frac{(W_{i-1}^{-1}.\delta g) \times (W_{i-1}^{-1}.\delta g)}{\delta g.W_{i-1}^{-1}.\delta g} \tag{2.31}$$

Where δr and δg represent the change between current and previous atomic coordinates and gradient respectively.

In theory as the energy approaches the minimum the method has a similar accuracy to that of Newton-Raphson. This work uses a combination of conjugate gradient and the VASP [47] implementation of Quasi-Newton RMM-DIIS method [60].

2.4 Selection Criteria

To ensure that DFT gives an accurate representation of the energy, we must first ensure that we are using a sufficiently high energy cut-off and k-point density. The cut-off energy has been varied between 300-700 eV and the k-point mesh is varied between 1x1x1-7x7x7. All phases have been tested through convergence tests, however, only Brucite (smallest unit cell) and Hydromagnesite (largest unit cell) are presented in this section.

Figure 2.3 presents the convergence tests for Brucite, where a 4x4x4 k-point mesh and 500 eV are sufficient high enough to reach convergence. Figure 2.4 is the convergence tests for Hydromagnesite, where a 3x3x3 k-point mesh and 500 eV cut-off ensures the energy is fully converged. To ensure consistency across all phases and that full convergence is achieved with minimal computer resources, all phases have been simulated using a k-point mesh of 4x4x4 and an energy cut-off of 500 eV.

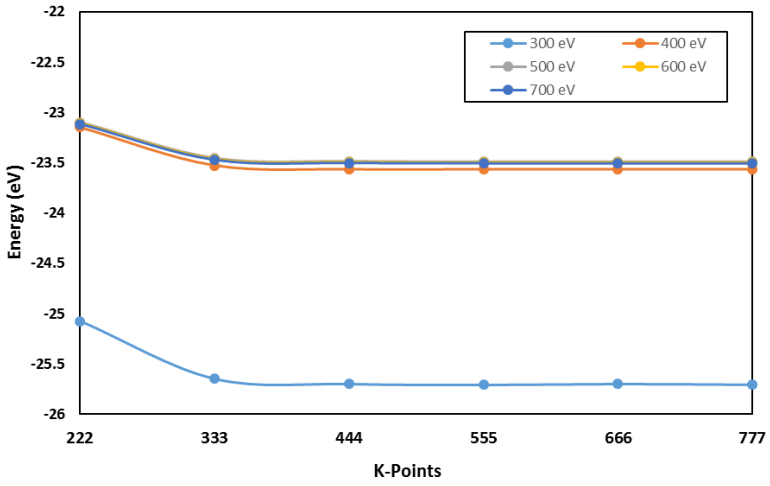

Figure 2.3: Convergence tests. Energy of fully minimised Brucite unit cell using optB86b-vdW as a function of k-points np grid for different energy cut-off.

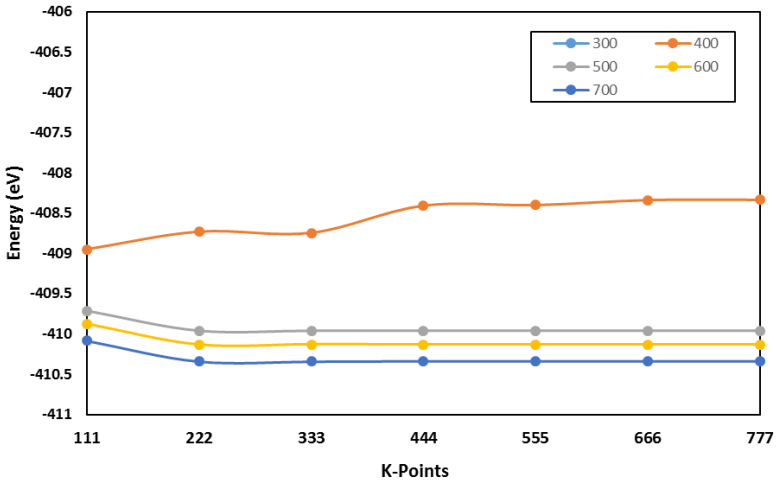

Figure 2.4: Convergence tests. Energy of fully minimised Hydromagnesite unit cell using optB86b-vdW as a function of k-points np grid for different energy cut-off.

3 Magnesium Oxides, Hydroxides and Carbonates

The use of DFT to simulate strong ionic and covalent bonding has been well studied [61, 62, 63, 64]. However, conventional DFT does not account for long range dispersion forces. Applying van der Waals (vdW) corrections to DFT has been demonstrated to improve the simulation of hydrated and carbonated magnesium phases [23]. However, it is unclear, which of the available methods gives the best representation across all Mg-rich phases. In this chapter, we present our simulations of Mg-rich phases including oxides, hydroxides and carbonates. The results are laid out detailing the representation of the structural properties and energies, followed by discussion of three different vdW corrections to DFT that have been tested.

The main aim of the chapter is to compare the methods of including vdW forces, with respect to crystal structures, elastic properties and enthalpies of formation of the known crystalline hydrated and carbonated magnesium phases and where no such data exist, to predict values.

3.1 Structure of Mg-Rich Phases

Periclase (MgO)

Periclase (Figure 3.1) has a face-centred cubic symmetry with the rock salt structure and space group Fm3m [65]. Upon minimization the structure and the symmetry are retained, for all functionals tested. Periclase is comprised of cubic close packed planes of oxygen atoms with magnesium in the face sharing MgO_6 octahedral sites. It has many applications from use as a refractory material to barrier for nuclear waste isolation plants. It is also believed to be one of the major minerals of the lower mantle (650-2900 km) [66].

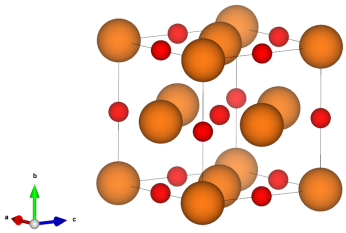

Figure 3.1: Periclase crystal structure with space group Fm3m: Mg in orange and O in red.

Magnesite ($MgCO_3$)

Magnesite (Figure 3.2) adopts a calcite structure of alternating layers of Mg^{2+} ions and carbonate CO_3^{2-} groups, where each CO_3^{2-} group is coordinated to three different Mg^{2+} ions. It is structurally related to the rock salt structure, with the carbonate ions sitting on the oxygen sites. This is coupled with a rhombohedral distortion which results in Magnesite having the space group R$\bar{3}$c [67], which is retained after minimisation. Magnesite has shown promising use as a long term CO_2 storage material [28].

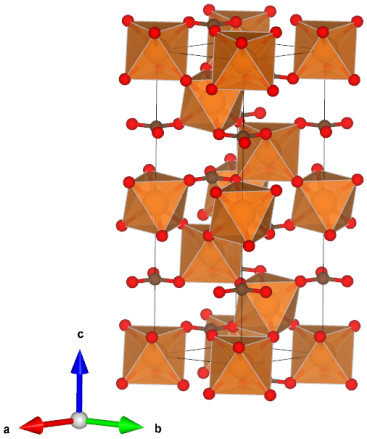

Figure 3.2: Magnesite crystal structure with space group R$\bar{3}$c: Mg in orange, C in grey and O in red.

Brucite ($Mg(OH)_2$)

Brucite (Figure 3.3) has a layered structure and comprises of hexagonally arranged edge sharing MgO_6 octahedra with hydroxyl (OH^-) ions. Brucite crystallises in the space group P$\bar{3}$m1 [68], which is retained upon minimisation. There is some debate in the literature concerning the nature of bonding between layers in Brucite. Work by Bushing *et al.* [69] and a more recent theoretical study by D'Arco *et al.* [70], suggest that the interaction between the layers is dominated by vdW-forces and hence these are required to obtain the correct interlayer spacing. However, in contrast Kruger *et al.* [71] suggests the interlayer spacing is controlled by H-bonding.

This highlights the complex interlayer bonding present in Brucite, and that further work is needed to evaluate the nature of this interlayer bonding.

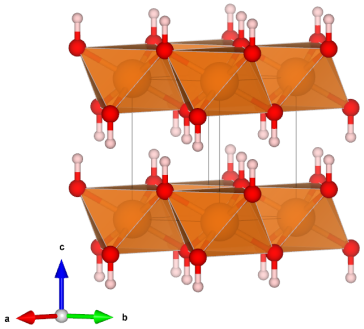

Figure 3.3: Brucite crystal structure with space group P$\bar{3}$m1: Mg in orange H in white and O in red.

Hydromagnesite ($Mg_5(CO_3)_4(OH)_2.4H_2O$)

Hydromagnesite (Figure 3.4) crystallises with in a monoclinic $P2_1/c$ structure [72, 73]. Hydromagnesite consists of a 3D framework formed of two unique MgO_6 octahedra. The first octahedron is coordinated to oxygen atoms of four carbonates, one hydroxyl and one water molecule, the second is coordinated to four carbonate and two hydroxyl ions. Hydroxyl groups in the structure have been shown to be shared between three MgO_6 octahedra and do not participate in H-bonding between octahedra [1]. In contrast the water molecules are not shared between the octahedra and form a 3D network of H-bonding.

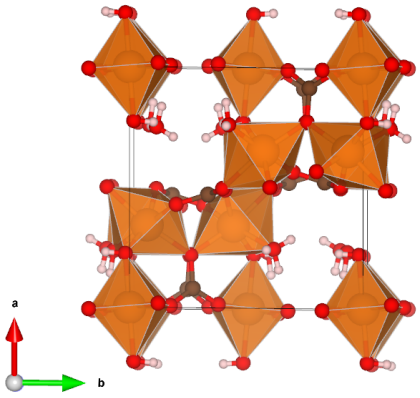

Figure 3.4: Hydromagnesite crystal structure with space group $P2_1/car$: Mg in orange, C in grey, H in white and O in red.

Hydromagnesite is used in some industrial fire retardants. When exposed to heat, hydromagnesite undergoes an endothermic reaction releasing H_2O at 395-515 ℃ forming Magnesite and effectively quenching a fire [1, 74, 75]. A further increase in the temperature to 515-640 ℃ induces a second decomposition reaction, forming MgO and CO_2.

Artinite ($Mg_2CO_3(OH)_2.3H_2O$)

Artinite contains both hydroxyl and carbonate groups similar to Brucite, Mg is octahedrally coordinated. The structure features 1D rods which are Brucite-like with equatorial Mg-OH bonds and apical $Mg-OH_2$ and $Mg-CO_3$ bonds. In naturally occurring Artinite, the apical ligand (H_2O and CO_3) are randomly placed. However, this is not feasible within the primitive unit cell used in our DFT calculations. Thus, we have constructed two models (Figure 3.6). Both models have rows of alternating CO_3^{2-} and H_2O in the b-direction. Structure A has alternating CO_3^{2-} and H_2O in the <011> direction (opposite octahedral faces), while structure B the rows in the <011> direction are either H_2O - H_2O or CO_3^{2-} - CO_3^{2-}.

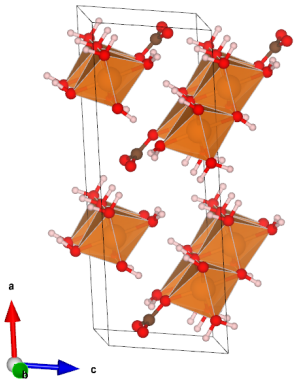

Figure 3.5: Artinite crystal structure with space group C2/m: Mg in orange, C in grey, H in white and O in red.

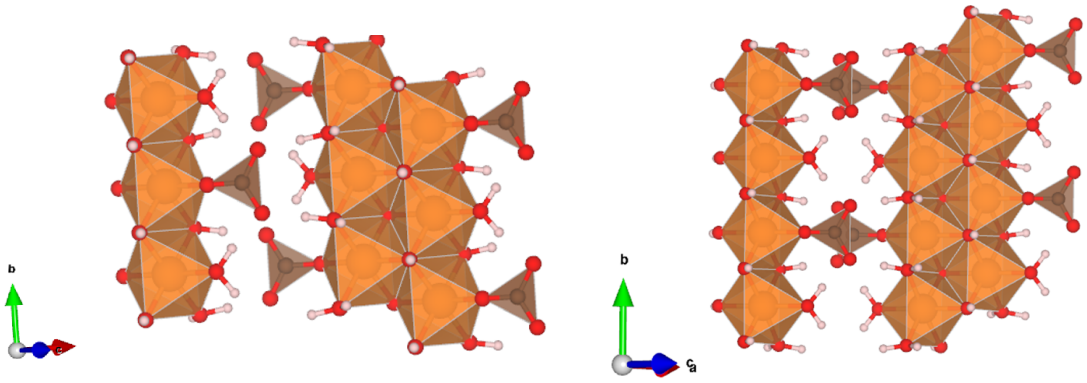

(a) Artinite A **(b)** Artinite B

Figure 3.6: Cross-section of Artinite Structures A and B with space group C2/m: Mg in orange, C in grey, H in white and O in red.

Nesquehonite ($MgCO_3.3H_2O$)

The structure of Nesquehonite (Figure 3.7) comprises of 2D infinite chains of corner sharing MgO_6 octahedra parallel to the b axis. Where each MgO_6 octahedra has two axially coordinated H_2O molecules. A third H_2O molecule is free and Hydrogen-bonds to CO_3^{2-} ions situated within the chains. Each CO_3^{2-} ion is coordinated to

three Mg^{2+} ions. Nesquehonite has the space group $P2_1/n$ [76], which is retained upon minimisation.

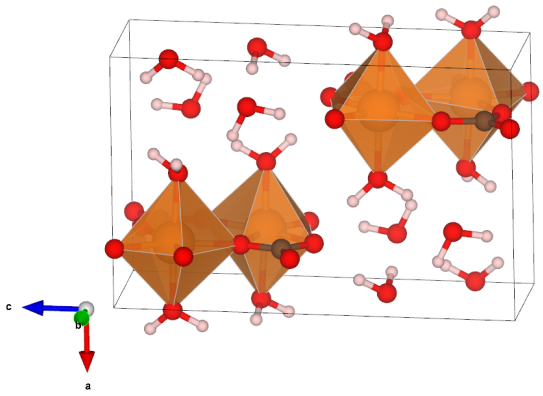

Figure 3.7: Nesquehonite crystal structure with space group $P2_1/n$: Mg in orange, C in grey, H in white and O in red.

Lansfordite ($MgCO_3.5H_2O$)

Lansfordite (Figure 3.8) is a low temperature phase which crystallises in the space group $P2_1/a$ [77], which is retained upon minimisation. The structure is comprised of two unique MgO_6 octahedra. The first is coordinated to six H_2O molecules and the second is coordinated to two carbonate ions and four H_2O molecules. There is a complex network of H-bonding between the two octahedra.

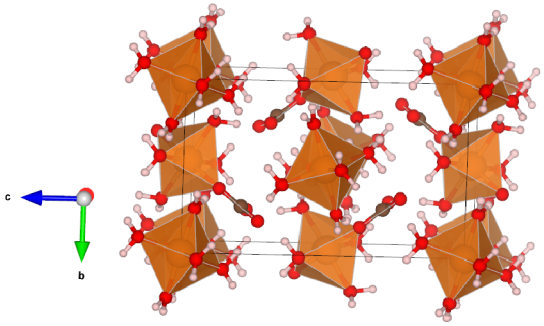

Figure 3.8: Lansfordite crystal structure with space group $P2_1/a$: Mg in orange, C in grey, H in white and O in red.

3.2 Structural Comparison

3.2.1 Lattice Parameters

Geometry optimisation was performed on all the phases using the cut-off and k-point density described in Section 2.4. The coordinate cell dimensions were minimised until the forces were below 0.01 eV/Å. Table 3.1 and Figure 3.9 summarise the calculated lattice parameters and percentage change from experiment of Mg-rich

phases. DFT without the inclusion of vdW corrections (PBE) shows a consistent overestimation of lattice parameters and volume, which is well documented in the literature due to the inherent under binding of the GGA functionals [78]. It is important to note that the experimental values are at 298 K, whereas simulated data does not account for temperature effects. It is known that in general, increasing the temperature induces an expansion in the volume. Hence, a slight underestimation of the lattice parameters would result in a more realistic comparison with experiment.

Hydromagnesite is an example where the inclusion of vdW greatly improves the structural representation compared to novdW, with optB86b-vdW and optB88-vdW both showing excellent agreement (within 1%). PBE-D3 behaves like PBE overestimating the volume of Hydromagnesite with a significant expansion along b. Chaka *et al.* [23] have shown that there is weak vdW interactions along the b direction which are not being fully represented.

The Artinite models considered in this work display a large change in the β angle of approximately 10%, perhaps suggesting that the random distribution of apical Mg-H_2O and Mg-(CO_3) has to be taken into account in the structural representation of Artinite.

Table 3.1: Unit cell parameters, a, b, c (Å), α, β, γ (°) and volume (Å^3) for all Mg-rich structures are calculated using PBE-D3, optB86b-vdW, optB88-vdW and PBE. Experimental structural parameters are provided in comparison.

	Experimental	**PBE-D3**	**optB86b-vdW**	**optB88-vdW**	**PBE**
Lansfordite					
a	7.364	7.188	7.203	7.215	7.247
b	7.632	7.568	7.573	7.578	7.670
c	12.488	12.520	12.443	12.438	12.650
α=γ	90.00	90.00	90.00	90.00	90.00
β	101.75	102.20	102.44	102.49	102.22
Volume	687.14	665.70	662.77	663.94	687.89
Nesquehonite					
c	7.701	7.600	7.561	7.562	7.755
a	5.365	5.416	5.383	5.382	5.461
b	12.126	11.874	11.904	11.919	11.912
α=γ	90.00	90.00	90.00	90.00	90.00
β	90.41	91.43	91.51	91.51	91.35
Volume	500.98	488.60	484.27	484.90	504.32
Artinite 1					
c	16.560	16.598	16.558	16.567	16.768
a	6.306	6.303	6.280	6.284	6.371
b	6.231	6.109	6.113	6.116	6.186
α=γ	90.00	90.00	90.00	90.00	90.00
β	90.10	97.87	97.77	97.75	98.69
Volume	642.50	633.01	629.82	630.88	653.27
Artinite 2					
c	16.560	16.547	16.499	16.505	16.709
a	6.306	6.314	6.293	6.298	6.380
b	6.231	6.140	6.147	6.151	6.223
α=γ	90.00	90.00	90.00	90.00	90.00
β	90.10	98.06	97.94	97.93	98.84
Volume	642.50	635.10	632.20	633.25	655.45
Hydromagnesite					
a	10.105	10.103	10.041	10.043	10.161
b	8.954	9.109	9.057	9.047	9.192
c	8.378	8.365	8.336	8.333	8.427
α=γ	90.00	90.00	90.00	90.00	90.00
β	114.44	114.21	114.12	114.05	114.34
Volume	690.12	702.07	691.94	691.47	717.16
Brucite					
c	6.277	6.320	6.310	6.312	6.374
a	5.437	5.470	5.464	5.466	5.519
b	9.007	9.130	9.254	9.310	9.535
α=β=γ	90.00	90.00	90.00	90.00	90.00
Volume	306.27	315.80	319.10	321.19	335.40
Magnesite					
a=b	4.637	4.671	4.661	4.663	4.693
c	15.023	15.077	14.937	14.935	15.180
α=β	90.00	90.00	90.00	90.00	90.00
γ	120.00	120.00	120.00	120.00	120.00
Volume	279.74	284.94	281.04	281.27	289.58
Periclase					
a=b=c	4.217	4.219	4.225	4.227	4.257
α=β=γ	90.00	90.00	90.00	90.00	90.00
Volume	74.99	75.11	75.42	75.54	77.16

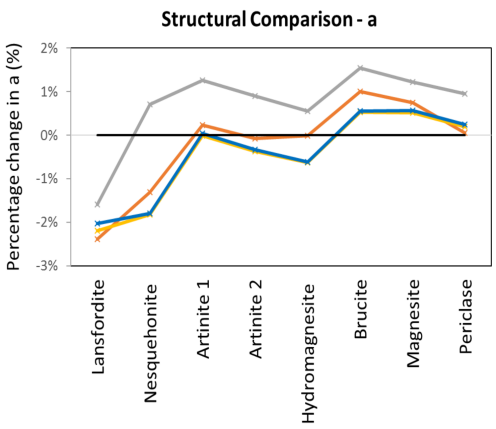

(a) Structural Parameter a

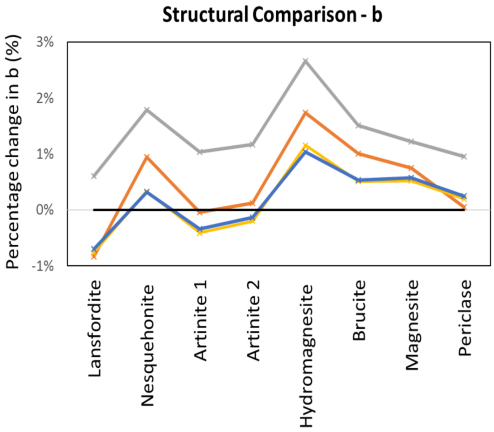

(b) Structural Parameter b

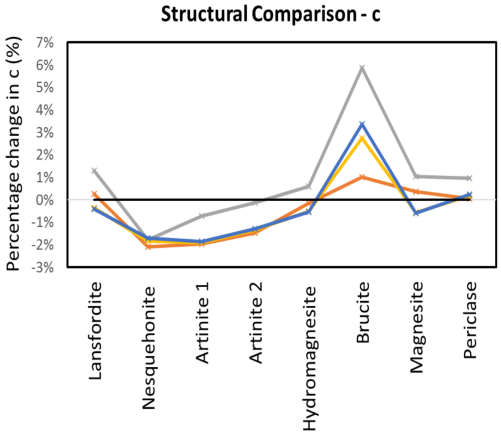

(c) Structural Parameter c

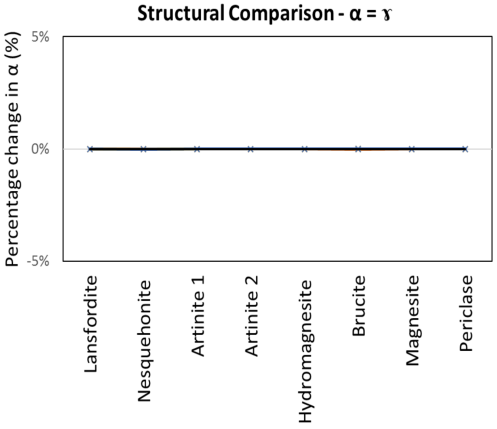

(d) Structural Parameter $\alpha = \gamma$

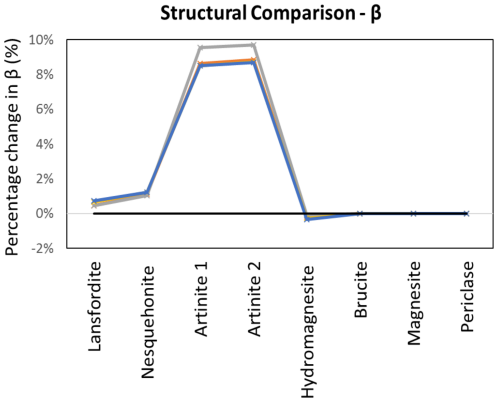

(e) Structural Parameter β

Figure 3.9: Percentage change in unit cell parameters between experimental and calculated values using PBE-D3, optB86b-vdW, optB88-vdW and PBE functionals for all Mg-rich phases.

Figure 3.10 shows the volume change from experiment for only those structures which contain water, the phases have been ordered from left to right in decreasing number of H_2O molecules per Mg ion. This highlights how the addition of H_2O results in a decrease in the predicted structural volumes compared to experiment, for all given vdW techniques. This decrease can be attributed to the increased number of hydrogen bonds present in each structure, increasing the interactions between species.

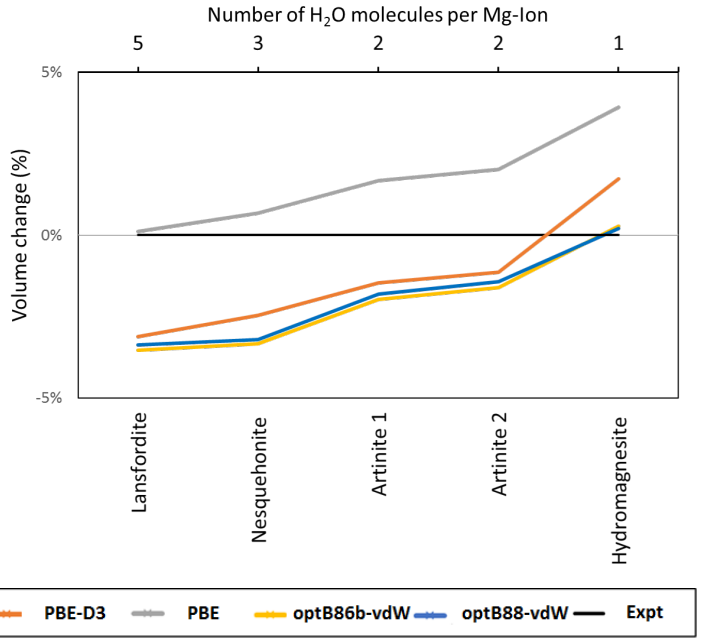

Figure 3.10: Percentage volume change between experimental and calculated values for all Mg-rich phases containing H_2O. Structures are ordered from left to right in increasing number of H_2O molecules per Mg ion.

Figure 3.11 depicts the change in volume from experiment, for the different Mg-O bonds, present in Mg minerals that do not contain H_2O (*i.e.* Mg-OH, Mg-O-CO_2 and Mg-O). Both Magnesite and Periclase have a similar calculated percentage volume change from experiment, regardless of the vdW correction applied. In contrast Brucite has a much larger variation in volume, compared to the other structures. This is a result of the layered structure which is particularly challenging to simulate, as the layers are held together by vdW forces [69]. This would imply that techniques which consider these interactions would excel over standard DFT. Indeed, PBE has the largest overestimation of the c axis ($\approx 9\%$) and as a consequence there is a large predicted expansion of the volume.

Comparison of the lattice parameters shows that all vdW corrections offer an improvement on the representation of volume and unit cell parameters for Mg-rich minerals. Where Figure 3.9 shows all values are within $\pm$ 5% of reported experimental values. This indicates that the application of vdW corrections to DFT is vital in generating accurate structural representations.

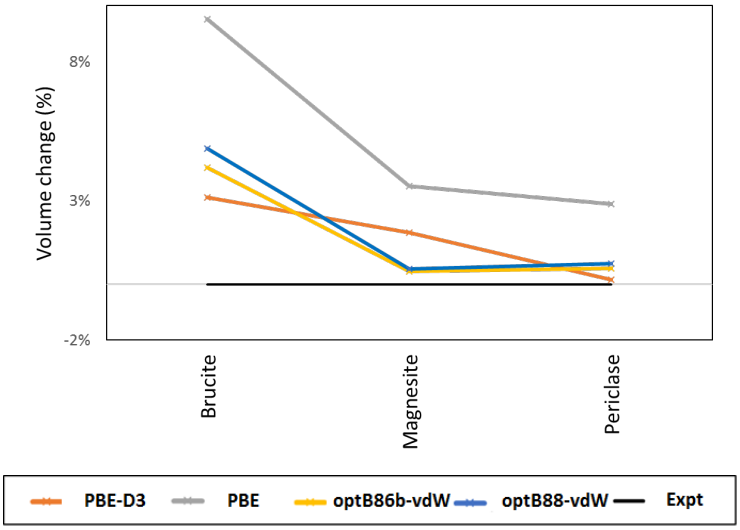

Figure 3.11: Percentage volume change between experimental and calculated values using PBE-D3, optB86b-vdW, optB88-vdW and PBE functionals for different Mg-O bonds (*i.e* Mg-OH, Mg-O-CO_2, Mg-O), in Brucite, Magnesite and Periclase.

3.2.2 Elastic Properties

Table 3.2 and 3.3 show the calculated bulk moduli and independent elastic constants for each structure compared to available experimental and theoretical literature data. The bulk modulus were calculated by averaging the first nine elastic constants (c_{11} : c_{33}) [79, 80].

Table 3.2: Calculated bulk moduli values B (GPa) and unique elastic constants (GPa) for Periclase, Magnesite and Brucite using PBE-D3, optB86b-vdW, optB88-vdW and PBE functionals. Experimental values are provided for comparisons.

	Literature				This Work			
	Experimental		Theoretical		optB86b-vdW	optB88-vdW	PBE-D3	PBE
Periclase								
B	163.9	[81]	158.0	[82]	157.90	159.09	157.30	150.89
c_{11}	299.0	[81]	291.0	[82]	297.09	295.19	299.04	272.52
c_{12}	96.4	[81]	91.0	[82]	87.96	90.75	86.00	89.74
c_{44}	157.1	[81]	139.0	[82]	146.16	147.83	144.05	140.91
Magnesite								
B	104.6	[83]	81.8 - 125	[84, 85, 86]	118.75	122.88	114.40	110.62
c_{11}	258.7	[83]	223 - 361	[84, 85, 86]	261.12	269.22	250.51	242.26
c_{12}	7.56	[83]	56.0 93.2	[84, 86]	74.71	78.07	72.29	72.72
c_{13}	5.88	[83]	35.9 77.7	[84, 86]	59.96	62.51	57.49	54.65
c_{33}	155.5	[83]	118 - 187	[84, 85, 86]	156.99	162.48	153.16	145.98
c_{55}	-	-	42.7	[84]	59.07	59.93	55.58	51.67
Brucite								
B	50.5 - 55.2	[87, 88]	52.3	[89]	67.82	67.94	65.42	58.24
c_{11}	154.0 - 159.0	[87, 88]	130.6	[89]	173.79	175.32	170.61	159.26
c_{33}	46.36 - 49.7	[87, 88]	48.5	[89]	80.22	79.23	87.83	53.81
c_{12}	42.1 - 44.4	[87, 88]	70.3	[89]	50.14	50.34	47.79	46.56
c_{13}	7.8 - 11.0	[87, 88]	10.0	[89]	20.14	19.98	19.34	14.64
c_{14}	0.2 - 1.3	[87, 88]	-	-	−0.24	−0.25	0.05	−0.19
c_{44}	21.3 - 22.8	[87, 88]	20.4	[89]	61.95	62.51	61.39	56.45

For Periclase, Magnesite and Brucite there is both experimental and theoretical bulk moduli values, with which to compare. Whereas for the other Mg-rich phases there

is no reported literature values and therefore each technique can only be compared to the other techniques presented here. All methods produce consistent bulk moduli values within 12 GPa of each other. Where comparison with literature values is possible, the values calculated here compare well. The individual elastic constants (c_{13}, c_{33}, c_{44}) for Brucite have a large deviation from literature values, the corresponding bulk modulus values is significantly larger. This is due to the sensitivity of elasticity of Brucite, on the interlayer bonding using DFT.

As the concentration of H_2O per Mg ion increases, the bulk modulus value decreases. Showing an indirectly proportional relationship between bulk modulus and the concentration of H_2O per Mg ion. This is due to the water expanding the structure and increasing the materials compressibility.

Table 3.3: Calculated bulk moduli values B (GPa) and unique elastic constants (GPa) for Hydromagnesite, Artinite 1, Artinite 2, Nesquehonite and Lansfordite in order of increasing H_2O concentration per Mg ion, using PBE-D3, optB86b-vdW, optB88-vdW and PBE.

	optB86b-vdW	**optB88-vdW**	**PBE-D3**	**PBE**
Hydromagnesite				
B	56.95	57.49	60.60	60.88
c_{11}	109.42	110.59	112.37	110.36
c_{12}	31.60	31.89	36.13	39.63
c_{13}	30.58	30.59	35.21	35.20
c_{15}	0.70	1.61	1.53	0.49
c_{22}	103.13	103.93	105.26	102.27
c_{23}	34.12	34.64	37.62	39.61
c_{25}	1.73	2.92	2.66	1.18
c_{33}	107.41	108.62	109.81	106.41
c_{35}	0.30	1.59	1.26	0.29
c_{44}	31.60	31.23	33.35	34.17
c_{46}	0.17	0.53	0.58	0.09
c_{55}	37.81	37.10	36.85	36.38
c_{66}	38.78	39.25	38.02	36.97
Artinite 1				
B	64.10	65.11	62.78	56.44
c_{11}	102.69	104.23	103.19	94.64
c_{12}	27.94	28.53	27.47	23.86
c_{13}	65.05	65.81	62.66	53.64
c_{15}	−0.12	−0.13	−0.17	−0.14
c_{22}	122.29	124.01	119.96	113.44
c_{23}	32.39	33.19	31.13	28.23
c_{25}	0.12	0.02	0.03	0.08
c_{33}	101.19	102.65	99.32	88.37
c_{35}	−0.18	−0.23	−0.23	−0.13
c_{44}	15.56	16.00	16.56	16.72
c_{46}	−0.14	−0.13	−0.11	0.02
c_{55}	23.16	23.87	23.87	24.46
c_{66}	40.23	41.11	39.36	34.71

	optB86b-vdW	optB88-vdW	PBE-D3	PBE
Artinite 2				
B	64.31	65.26	62.58	56.37
c_{11}	100.18	101.87	100.11	92.23
c_{12}	29.49	30.09	28.87	25.25
c_{13}	64.71	65.38	61.98	53.06
c_{15}	−0.05	−0.03	−0.05	−0.08
c_{22}	122.23	123.95	119.67	113.89
c_{23}	31.76	32.44	30.02	27.13
c_{25}	0.00	0.14	−0.18	0.09
c_{33}	104.51	105.76	101.73	90.36
c_{35}	−0.53	−0.38	−0.63	−0.27
c_{44}	13.73	14.22	14.96	16.17
c_{46}	−0.02	−0.04	0.02	0.06
c_{55}	19.93	20.77	20.92	22.64
c_{66}	41.47	42.47	40.57	35.48
Nesquehonite				
B	49.58	51.16	48.29	43.52
c_{11}	58.52	60.06	58.91	52.42
c_{12}	19.36	20.39	18.57	17.47
c_{13}	38.83	40.61	37.23	30.85
c_{15}	0.30	0.13	0.42	0.29
c_{22}	95.62	98.50	94.32	91.87
c_{23}	37.25	38.28	35.59	30.91
c_{25}	0.56	0.50	0.61	0.44
c_{33}	101.18	103.28	98.58	88.96
c_{35}	0.80	0.58	0.91	0.67
c_{44}	13.05	13.44	12.89	12.70
c_{46}	−0.07	−0.08	−0.02	−0.05
c_{55}	15.91	16.23	16.38	17.32
c_{66}	18.74	19.38	18.15	17.44
Lansfordite				
B	44.99	45.81	44.39	39.97
c_{11}	68.76	69.33	68.68	64.49
c_{12}	38.71	39.67	36.67	30.69
c_{13}	32.95	34.08	32.30	28.24
c_{15}	0.49	0.43	0.30	0.15
c_{22}	57.82	58.56	57.78	53.84
c_{23}	36.57	37.04	35.94	31.19
c_{25}	0.09	0.07	0.12	−0.10
c_{33}	61.88	62.80	63.24	61.19
c_{35}	−0.50	−0.36	−0.59	−0.38
c_{44}	26.56	26.79	26.46	25.31
c_{46}	0.33	0.22	0.33	0.23
c_{55}	19.18	19.30	20.09	19.41
c_{66}	15.89	15.85	16.78	16.74

3.3 Heat of Formation for Mg-Rich Phases

The heats of formation for the four approaches were calculated and compared to experimental values. Producing accurate and reliable energies is an important step towards being able to reproduce and predict thermodynamic properties. As such it is vital to choose a method which can reliably calculate the relative energies between all phases. The enthalpy of formations was calculated using Equation 3.1.

$$aM_{(s)} + bH_{2(g)} + cO_{2(g)} + dC_{(s)} \longrightarrow M_a.H_{2b}.O_{2c}.C_{d(s)} \tag{3.1}$$

The theoretical heats of formation have been calculated at without the inclusion of temperature effects (*i.e.* 0 K) whereas experimental values are at 298 K. Consequentially, absolute values can not be compared, but it is possible to compare trends.

Table 3.4 shows experimental and calculated heats of formation for Mg-rich minerals. Structures have been ordered, from top to bottom, with decreasing concentration of water molecules per Mg ion *i.e.* Hydromagnesite $Mg_5(CO_3)_4(OH)_2.4H_2O$ has lower water concentration per Mg ion than Nesquehonite $MgCO_3.3H_2O$.

Table 3.4: Calculated (0 K) enthalpies of formation (ΔH_f kJ/mol) for all Mg-rich phases using PBE-D3, optB86b-vdW, optB88-vdW and PBE functionals, and compared with experimental values at 298 K [90].

	Experimental	**PBE-D3**	**optB86b-vdW**	**optB88-vdW**	**NovdW**
Lansfordite					
	n/a	−2593.19	−2602.02	−2000.03	−2493.99
		n/a	*n/a*	*n/a*	*n/a*
Nesquehonite					
	−1977.30	−1944.80	−1976.76	−2000.03	−1882.08
		-2%	*0%*	*1%*	*-8%*
Artinite 1					
	−2920.60	−2844.29	−2896.12	−2943.26	−2738.62
		-3%	*-1%*	*1%*	*-6%*
Artinite 2					
	−2920.60	−2843.25	−2895.72	−2942.75	−2738.57
		-3%	*-1%*	*1%*	*-6%*
Hydromagnesite					
	−6514.90	−6151.75	−6376.57	−6504.92	−5987.67
		6%	*-2%*	*0%*	*-8%*
Brucite					
	−924.50	−874.94	−897.43	−922.28	−838.44
		-5%	*-3%*	*0%*	*-9%*
Magnesite					
	−1095.80	−1010.27	−1074.29	−1100.42	−983.79
		-8%	*-5%*	*0%*	*-10%*
Periclase					
	−601.70	−542.37	−572.01	−593.67	−522.70
		-10%	*-5%*	*-1%*	*-13%*

Correcting heats of formation to 0 K would result in a lower magnitude value, however, this commonly results in $\approx$ 1% change [90]. This is not possible for all

phases due to incomplete experimental data. As seen in Table 3.4 the application of vdW corrections improves the heats of formations for all Mg-rich phases. The inclusion of vdW corrections improves the representation compared to no-vdW as mesasured by the % difference, additionally the modified functionals (optB86b-vdW and optB88-vdW) improve the representation to a greater extent. Periclase has a large percentage change in the heat of formation (no-vdW, PBE-D3), however, this refers to only a small change in the absolute values.

Figure 3.12a depicts the difference in ΔH_f from experiment, where the structures are ordered from right to left in increasing number of hydrogen bonds per formula unit. H-bond has been defined as being less than 2.8 Å and having a bond angle between 90-180° [91]. This demonstrates that for all techniques increasing the number of H-bonds in a structure decreases the accuracy in the ΔH_f.

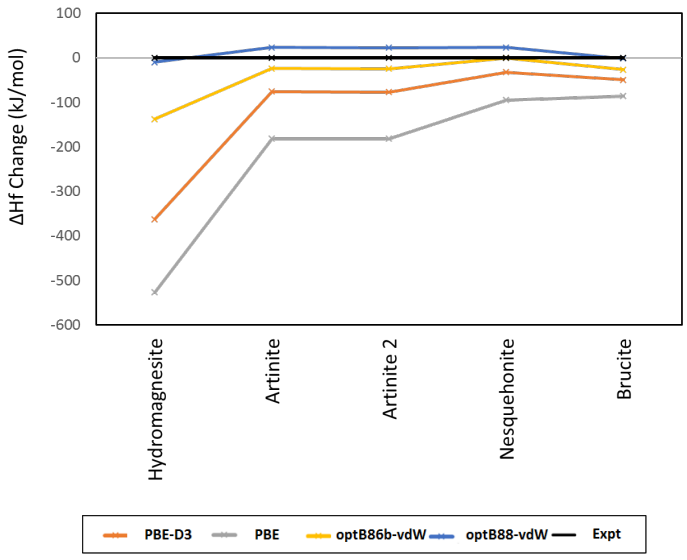

Figure 3.12(a): ΔH_f^{Phase} (kJ/mol) difference for all DFT techniques, for Mg-rich phases containing Hydrogen. Structures are ordered from right to left in increasing number of Hydrogen bonds per formula unit.

Figures 3.12b to 3.12c display the difference between calculated and experimental heat of formation, the values are corrected to give the energy difference per Mg ion (Equation 3.2), where n is the number of Mg ions per formula unit.

$$\Delta H_{Diff}^{Phase} = \frac{(\Delta H_f^{exp} - \Delta H_f^{calc})}{nMg} \tag{3.2}$$

Comparing only structures which contain H_2O (Figure 3.12b). Techniques which apply vdW corrections result in an increase in ΔH_{diff} for each H_2O molecule added (≈10-20 kJ/mol per H_2O). This is a result of hydrogen bonding between, an increased number of H_2O molecules, being simulated. In contrast no-vdW gives negligible result from the addition of H_2O molecules, which is to be expected.

Figure 3.12c compares the ΔH_{diff} for different Mg-O bonds (*i.e* Mg-OH, Mg-O-CO_2, Mg-O). The optB86b-vdW and optB88-vdW techniques produce a negligible different between the different Mg-O bonds. Whereas, PBE-D3 and no-vdW have a large negative shift for Magnesite, compared to Brucite and Periclase. This non-uniform shift for different Mg-O bonds makes it difficult to apply a constant correction to these methods.

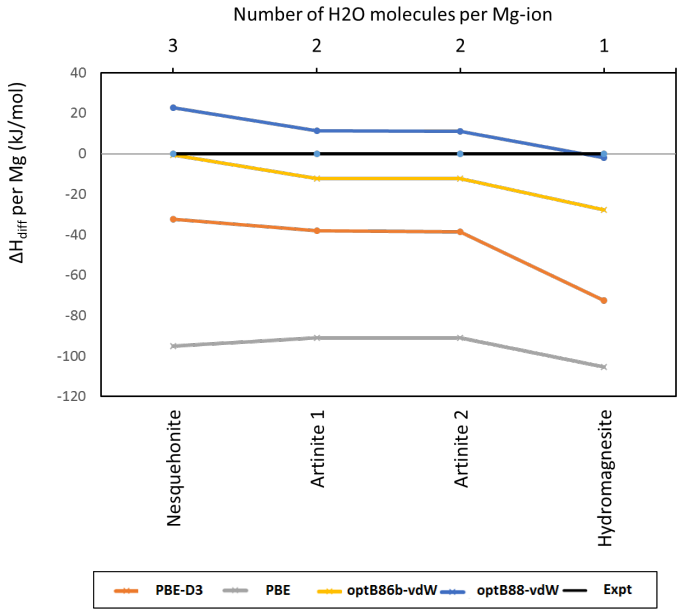

Figure 3.12(b): ΔH_{diff}^{Phase} (kJ/mol) per Mg ion using all DFT techniques, for Mg-rich phases containing H_2O. Structures ordered from left to right increasing H_2O molecules per Mg ion.

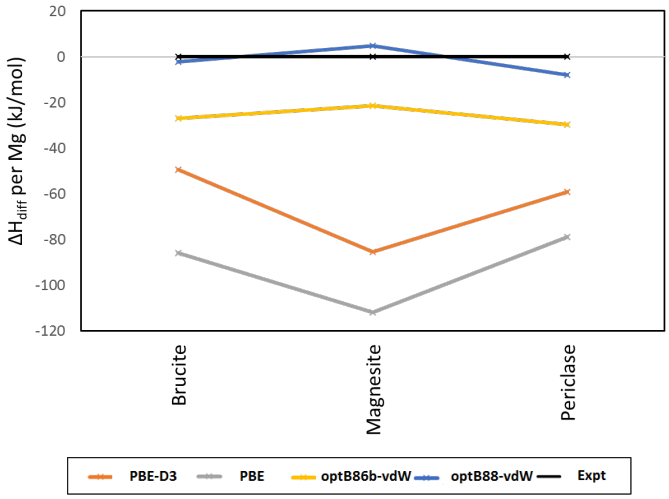

Figure 3.12(c): ΔH_{diff}^{Phase} (kJ/mol) per Mg ion using all DFT techniques, for different Mg-O bonds (*i.e* Mg-OH, Mg-O-CO_2, Mg-O) in Brucite, Magnesite and Periclase.

3.4 Conclusion

This chapter has evaluated three different methods for applying vdW corrections to DFT, through structural and energetic comparison. All vdW techniques improve the simulation compared to uncorrected DFT. This shows that the inclusion of vdW is vital to obtaining accurate representations of Mg-rich phases. To summarise:

- The inclusion of vdW dispersion forces offer an improvement over standard DFT for the structural properties.
  - vdW techniques have been demonstrated to reproduce the experimental lattice parameters (Table 3.1 and Figure 3.9), where all values are within $\pm$ 5%.
  - Where comparison with literature is possible, calculated elastic properties have been shown to reproduce literature values, for all techniques.
  - All DFT approaches produce consistent bulk moduli, where all values are within 12 GPa of the other techniques.
- All vdW techniques improve the representation of ΔH_f compared to PBE with no vdW correction.
  - optB88-vdW and optB86b-vdW give the best agreement with experimental values.

The next chapter will evaluate different DFT techniques and there ability to produce accurate thermodynamic properties and phase diagrams. This in turn will be used to gain valuable insight in to the composition and interactions of Magnox sludge.

4 Mg-Rich Mineral Phase Diagrams

One of the major challenges of atomistic modelling is to produce data which can be linked to macroscopic experiments and be used to inform experimentalists. This chapter presents a method to generate phase diagrams for Mg-rich phases using DFT calculated energies. This enables us to evaluate compositions of Mg-rich minerals at different temperatures (T), partial pressures of carbon dioxide (p_{CO_2}) and partial pressures of water (p_{H_2O}), which is of particular value in the determination of Magnox sludge composition.

The aims of this chapter are:

- To establish a straight forward approach for phase diagram generation.
- To assess the accuracy and reliability of the phase diagrams.
- Predict phase diagrams of under different conditions of p_{CO_2}, p_{H_2O} and temperature.

Identifying which phases are the most thermodynamically stable at various environmental conditions (*i.e.* p_{CO_2}, p_{H_2O}), will enable us to predict the composition of Magnox sludge stored over long time scales.

4.1 Methodology

To begin we assume that the Mg-rich phases in this work are the most probable phases present and can be defined through a generic reaction scheme (Equation 4.1). This enables the comparison of Mg-rich phases through a common reaction scheme.

$$xMgO + yH_2O + zCO_2 \rightarrow A \tag{4.1}$$

The system will be in equilibrium, when the chemical potentials are equal *i.e.* the change in free energy $\delta G_{T,p} = 0$.

$$\delta G_{T,p} = \mu_A - x\mu_{MgO} - y\mu_{H_2O} - z\mu_{CO_2} = 0 \tag{4.2}$$

Assuming that H_2O and CO_2 are gaseous species,

$$\mu_{H_2O} = \mu^0_{H_2O} + \Delta\mu_{H_2O} \tag{4.3}$$

$$\mu_{CO_2} = \mu^0_{CO_2} + \Delta\mu_{CO_2} \tag{4.4}$$

where for an ideal gas $\Delta\mu_x = RT \ln (p_x/p^{\ominus})$, where $p^{\ominus}$ is the standard state at 1 bar and μ^0_x is the partial molar free energy of compound x at its standard state. As both MgO and A (*i.e.* the product) are solids we assume,

$$\mu_{MgO} = \mu^0_{MgO} \tag{4.5}$$

$$\mu_A = \mu^0_A \tag{4.6}$$

Substituting Equations 4.3 to 4.6 in to Equation 4.2 we get,

$$\mu^0_A - x\mu^0_{MgO} - y\mu^0_{H_2O} - z\mu^0_{CO_2} = y\Delta\mu_{H_2O} + z\Delta\mu_{CO_2} \tag{4.7}$$

As μ^0_A corresponds to the partial molar free energy of compound A, we can replace the left hand side of Equation 4.7 by ΔG^0.

$$\delta G_{T,p} = \Delta G^0 - y\Delta\mu_{H_2O} - z\Delta\mu_{CO_2} \tag{4.8}$$

where at equilibrium $\delta G_{T,p} = 0$, and hence, at equilibrium we get,

$$\Delta G^0 = y\Delta\mu_{H_2O} + z\Delta\mu_{CO_2} \tag{4.9}$$

In the case of an ideal gas,

$$\Delta G^0 = RT\ ln(p^y_{H_2O} \cdot p^z_{CO_2}) \tag{4.10}$$

Thus we can find the values of $\Delta\mu_{H_2O}$ and $\Delta\mu_{CO_2}$ (or $p^y_{H_2O}$ and $p^z_{CO_2}$), when compound A is in equilibrium *i.e.* is more or less stable than MgO. The procedure can then be applied to all phases to identify which is the most stable, provided ΔG^0 is known for each Mg phase.

4.1.1 Calculating the Free Energy ΔG^0

The free energy can be calculated using Equation 4.11.

$$\Delta G^0 = \sum \Delta G^{0,products}_f - \sum \Delta G^{0,reactants}_f \tag{4.11}$$

In this work we calculate the free energy of each component using the calculated DFT energy.

$$\Delta G_f = U_0 + U_{ZPE} + A_{vib} \tag{4.12}$$

where U_0 is the calculated internal energy from the DFT optimisation, U_{ZPE} is the zero point energy (Equation 4.13) and A_{vib} is the vibrational Helmholtz free energy (Equation 4.14).

$$U_{ZPE} = \sum_{i}^{3n} \frac{R\theta_i}{2} \tag{4.13}$$

$$A_{vib} = \sum_{i}^{3n} RT \ln\left(1 - e^{-\theta_i/T}\right) \tag{4.14}$$

where 3n is the total number of vibrational modes, θ_i is the characteristic vibrations temperature (frequency of the vibrational mode in Kelvin) (Equation 4.15).

$$\theta_i = \frac{h\nu_i}{k_B} \tag{4.15}$$

For the solid phases the entropy contribution is calculated from first principles with two approximations:

- Only the zone centre vibrational frequencies are calculated and hence the acoustic modes are neglected.
- The vibrational frequencies do not vary with volume.

In the case of the gaseous species the standard free energy will vary significantly with temperature. Furthermore, as the DFT simulations are designed for condensed phase systems, we use the experimental data to determine the temperature dependent free energy term (Equation 4.16), where $\delta H(T)$ is calculated using Equation 4.17, $\delta H_{expt}(T)$ is the change in enthalpy from 298 K to T, for which values can be obtained from the NIST database [90].

$$\Delta G_f^0 = U_0 + U_{ZPE} + \delta H_{expt}(T) - TS_{expt}(T) \tag{4.16}$$

$$\delta H_{expt}(T) = \Delta H_{expt}(298\ K) - \Delta H_{expt}(298\ K \rightarrow T) \tag{4.17}$$

Thus the phase boundaries can be identified provided the free energies of the solid phases can be calculated.

4.2 Brucite, Periclase and Magnesite Phase Diagram: Neglecting Temperature Dependence of ΔG^0

Using Equations 4.11 to 4.17 it is possible to produce phase diagrams for Mg-rich phases. However, it is important to first test this methodology to ensure that the

phase diagrams produced are an accurate representation of the experimental data. This can be achieved by producing phase diagrams of experimentally well defined phases. Figure 4.1 shows the phase diagrams of Brucite, Magnesite and Periclase for both experimental and DFT techniques. These phase diagrams have been constructed at 0 K. Therefore, the A_{vib} terms outlined in Equation 4.12 become zero. The use of 0 K was chosen to produce a simpler expression for the Gibbs free energy. The Gibbs free energy can now be defined Equation 4.18, for both solid and gaseous phases.

$$\Delta G_f^0 = U_0 + U_{ZPE} \tag{4.18}$$

The values for $\Delta\mu_{H_2O}$ and $\Delta\mu_{CO_2}$ are varied between -3 eV and 2 eV, which is equivalent to pressures of 10^{-51} bar and 10^{34} bar (assuming ideal gas behaviour).

For the experimental phase diagram the ΔG_f^0 is calculated using enthalpies that have been corrected to 0 K (Equation 4.19). Where $\Delta H_{expt}(298 \rightarrow 0\text{K})$ is the change in enthalpy from 298 to 0 K. The values were obtained from the NIST database [90].

$$\delta H_{expt}(0\ K) = \Delta H_{expt}(298\ K) - \Delta H_{expt}(298 \rightarrow 0\ K) \tag{4.19}$$

The inclusion of the ZPE for the theoretical methods is essential for reproducing the experimental values. All techniques agree with the experimental phase diagram, with small constant shifts in the values for each method. This implies that a correction factor may be calculated for each technique to better reproduce experimental values.

The first test for the model was to evaluate the relative stability of Brucite ($Mg(OH)_2$), Periclase (MgO) and Magnesite ($MgCO_3$), following the procedure outlined in Section 4.1, but for each pair of phases. Table 4.1 shows the calculated and experimental triple point for all techniques used. The optB86b-vdW and optB88-vdW functionals show excellent agreement with the experimental triple point, where all three phases exist (Table 4.1). Therefore, validating the chosen methodology and the use of the optB86b-vdW method.

Table 4.1: Calculated and experimental triple point (eV) for Brucite, Periclase and Magnesite phase diagram.

	Experimental	**optB86b-vdW**	**optB88-vdW**	**PBE-D3**	**PBE**
$\Delta\mu_{CO_2}$	-1.25	-1.30	-1.20	-0.95	-0.85
$\Delta\mu_{H_2O}$	-0.85	-0.90	-0.88	-0.83	-0.68

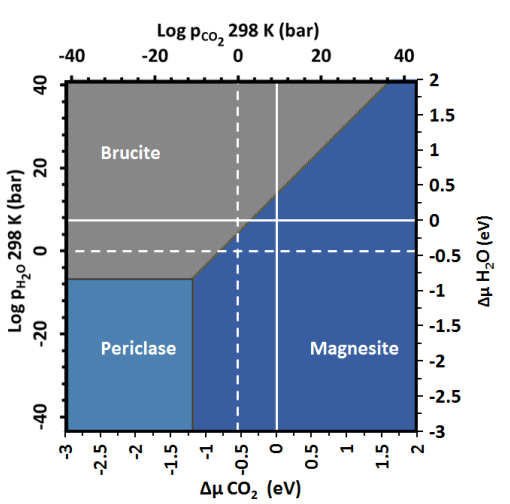

(a) Experimental (0 K)

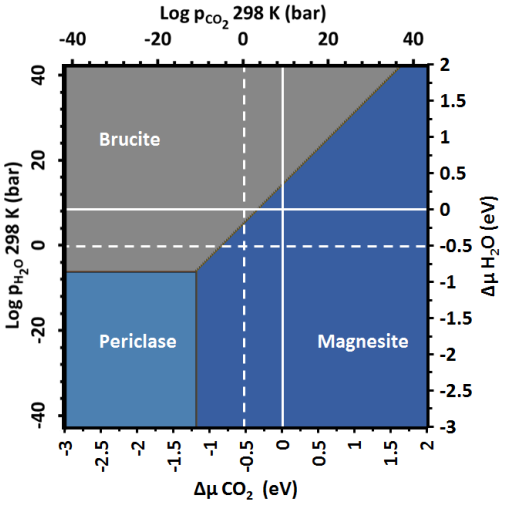

(b) optB88-vdW

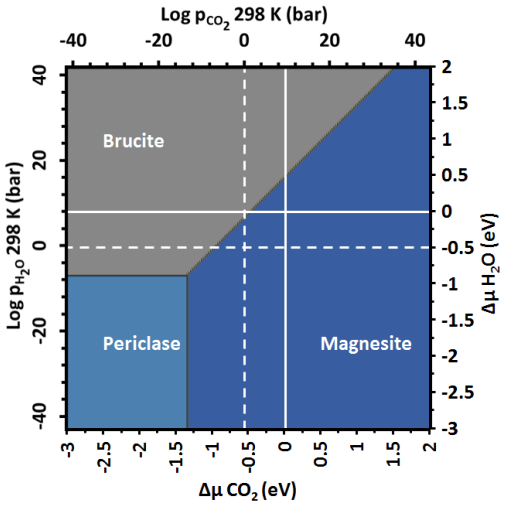

(c) optB86b-vdW

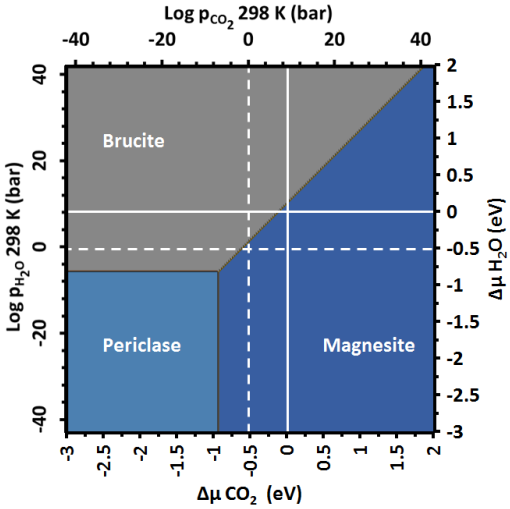

(d) PBE-D3

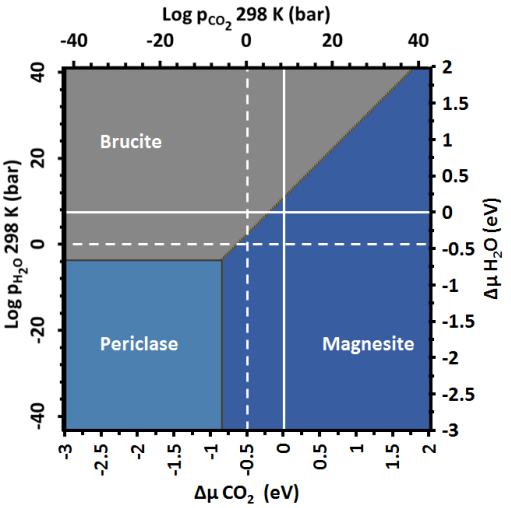

(e) PBE

Figure 4.1: Phase diagrams of ■ Brucite, ■ Periclase and ■ Magnesite a) Experimental (Corrected to 0 K) b) optB88-vdW c) optB86b-vdW d) PBE-D3 e) PBE. Solid and dashed white lines equal to 1 bar pressure at 0 K and 298 K respectively.

4.3 Mg-Rich Mineral Phase Diagram: Neglecting Temperature Dependence of ΔG^0

This section presents the predicted phase diagrams which include all Mg-rich mineral phases considered in this work (Figure 4.2). As before the phase diagrams have been produced using the calculated free energies at 0 K, including ZPE contributions. Due to the limited literature data on Lansfordite and Artinite, an experimental phase diagram cannot be constructed. Therefore, the different DFT methods can only be compared to the others presented here. The predicted phase diagrams have excellent agreement with each other, with small but significant shifts in the location of phase transitions.

In the previous section we demonstrated how optB86b-vdW reproduces the experimental phase diagram, by comparing to experimentally well characterised Mg-rich mineral phases. Based on this we can assume optB86b-vdW will reproduce the experimental phase diagram when all Mg-rich phases are included in the calculation. Figure 4.2 shows that under atmospheric conditions the most thermodynamically stable phase is Magnesite. This agrees well with the work of Chaka *et al.* [23], which states that at atmospheric conditions and 298 K, Magnesite is the most stable phase.

Table 4.2: Predicted thermodynamically most stable Mg-rich phase at a range of reference conditions using different DFT functionals.

Conditions	optB86b-vdW	optB88-vdW	PBE-D3	PBE
400 ppm CO_2 32 mbar H_2O at 298 K	Magnesite	Magnesite	Magnesite	Magnesite
1 bar CO_2, 1 bar H_2O at 298 K	Magnesite	Magnesite	Magnesite	Magnesite
1 bar CO_2, 1 bar H_2O at 0 K	Lansfordite	Lansfordite	Lansfordite	Lansfordite

Table 4.2 shows the predicted most thermodynamically stable phases at three different reference conditions. All DFT techniques predict the same Mg-rich phase to be stable for each set of reference conditions. However, closer inspection of the phase diagrams show small shifts in the location of phase transitions. For a fixed $\Delta\mu_{CO_2}$ all DFT with vdW corrections predict the phase boundaries to occur at a smaller (more negative) $\Delta\mu_{H_2O}$, compared to standard DFT. The results indicate that the inclusion of vdW corrections provide a better representation of weak/medium bonding. For a given $\Delta\mu_{H_2O}$ PBE-D3 and PBE predict that the phase transitions occur at a larger (more positive) $\Delta\mu_{CO_2}$ compared to optB86b-vdW and optB88-vdW. This is due to standard DFT failing to describe the weak vdW interactions accurately. In the case of PBE-D3, there is a slight improvement over standard DFT, however, there is still a shift compared to optB86b-vdW and optB88-vdW. This is due to limitations in the PBE-D3 vdW correction.

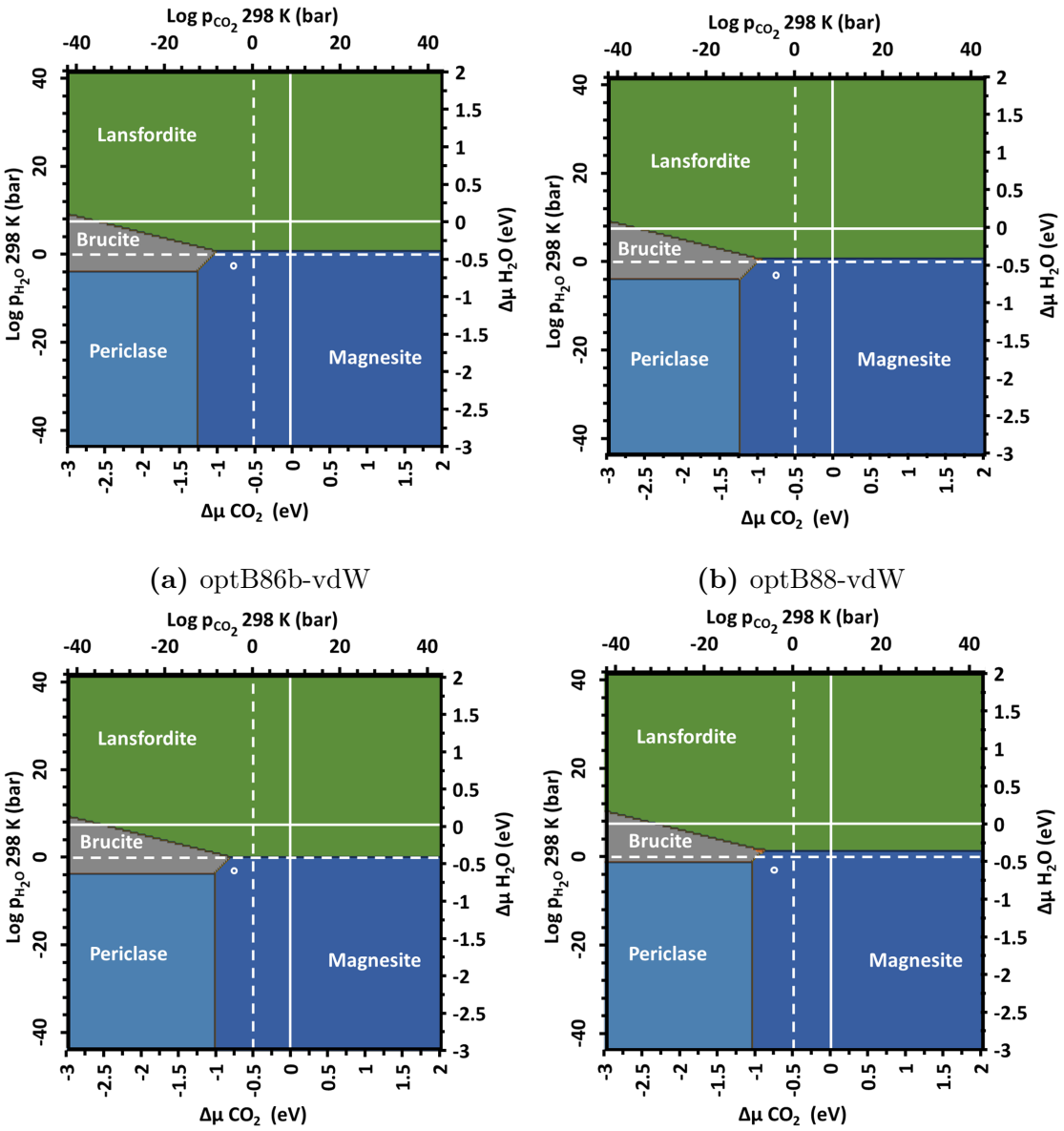

(a) optB86b-vdW

(b) optB88-vdW

(c) PBE-D3

(d) PBE

Figure 4.2: Phase diagram of all Mg-rich phases at 0 K: ■ Periclase, ■ Magnesite, ■ Brucite, ■ Hydromagnesite, ■ Artinite, ■ Nesquehonite and ■ Lansfordite a) optB86b-vdW b) optB88-vdW c) PBE-D3 d) PBE. Solid and dashed white lines equal to 1 bar pressure at 0 K and 298 K. White circle represents; 400 ppm CO_2 and 32 mbar of H_2O at 298 K (atmospheric conditions)

There is good agreement between different DFT functionals for the predicted Mg-rich phase diagrams, where all phases are included. Therefore, as optB86b-vdW describes well the experimental phase diagram (Section 4.2) and as all the phase diagrams, for different techniques, appear to be similar but shifted, we will now on use only optB86b-vdW for our discussion. Figure 4.2 shows that as the $\Delta\mu_{CO_2}$ increases, minerals with a higher carbon content are thermodynamically more stable. This can be seen as Periclase transforms to Magnesite, at $\Delta\mu_{CO_2}$ = -1.3 ($p_{CO_2} = 10^{-13.9}$ bar) eV for the opt functionals and $\Delta\mu_{CO_2}$ = -1 eV ($p_{CO_2} = 10^{-8.8}$ bar) for PBE-D3 and PBE. Similarly as the p_{H_2O} increases, hydrated phases are thermodynamically more stable. This is supported by the transition from Periclase to Brucite $\Delta\mu_{H_2O} \approx -0.9$ eV ($p_{H_2O} = 10^{-7.1}$ bar) and then from Brucite to Lansfordite at $\Delta\mu_{H_2O} \approx -0.5$ eV ($p_{H_2O} = 10^{-0.3}$ bar). Magnesite also transitions to Lansfordite at $\Delta\mu_{H_2O} \approx -0.6$ eV ($p_{H_2O} = 10^{-2.0}$ bar).

To summarise, there is good agreement between different DFT functionals for the predicted Mg-rich phase diagrams. However, the major limitation of this approach is that it ignores the vibrational contributions to the free-energy. The next section will calculate the T using the calculated vibrational contributions and determine the impact on phase diagram predictions.

4.4 Mg-Rich Mineral Phase Diagram: Including Temperature Effects

This section will expand upon the previous phase diagram to also consider temperature effects, as the magnesium phase present may depend on the temperature the nuclear sludge is stored. Hence, we now need to consider the vibrational entropy of the mineral phases. Inclusion of the entropy for both solid and gaseous phases is vital to produce accurate predicted phase diagrams. Entropy values for solid minerals have been calculated from the vibrational contribution using Equations 4.13 to 4.15 and for gaseous states the entropy values where taken from NIST experimental database [90].

4.4.1 Predicted Free Energy Phase Diagrams as a Function of Temperature

This section evaluates the effect of including temperature on the free energy of Mg-rich phases. In addition, this allows a comparison of the stability of different phases under a range of conditions. All phase diagrams use $\Delta\mu_{H_2O} = 0$ eV (p_{H_2O}=1 bar) and three different pressures for CO_2. The three pressures of CO_2 selected are $\Delta\mu_{CO_2} = 0$ eV (p_{CO_2}=1 bar), which corresponds to standard conditions for pressure, and the upper/lower limits of the methodology $\pm\Delta\mu$ = 1 eV *i.e.* high $p_{CO_2} = 10^{25}$ bar and low $p_{CO_2} = 10^{-8.8}$ bar. For all conditions only the phase diagram for optB86b-vdW is presented here, as this method has previously been shown to reproduce experiments. The phase diagrams for all other DFT techniques used are available in Appendix A.1.

1 bar p_{CO_2} and 1 bar p_{H_2O}

DFT optB86b-vdW predicts that at $\Delta\mu_{CO_2} = \Delta\mu_{H_2O} = 0$ eV, which corresponds to 1 bar p_{CO_2} and p_{H_2O}, at all temperatures considered Magnesite is the most thermodynamically stable phase (Figure 4.3). This is consistent with the previous predictions of Chaka *et al.* [23] (Section 4.3), where magnesite was predicted to be the most stable phase at 298 K. If Magnesite is kinetically inhibited, which experimentally has been shown [27], then the metastable phase, Hydromagnesite is the most stable phase under all temperatures simulated.

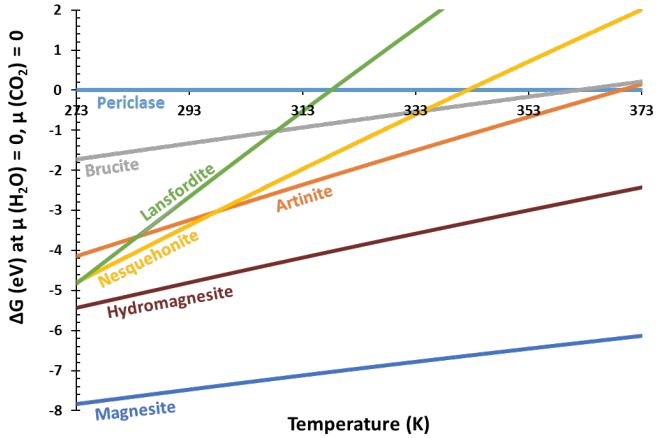

Figure 4.3: ΔG^0 as a function of T phase diagram at 1 bar p_{CO_2} and 1 bar p_{H_2O} for the optB86b-vdW functional.

Table 4.3 shows the predicted phase transitions that occur in the temperature range considered for all functionals. There is good agreement between all methods used, where all agree that Magnesite and Hydromagnesite are the two most thermodynamically stable phases. However, there are small shifts in the predicted temperatures for phase transitions across the different techniques, due to the difference in how vdW corrections are implemented.

Table 4.3: Temperature of phase transitions at 1 bar p_{H_2O} and 1 bar p_{CO_2}, where $>$ represents a phase transition that occurs above and $<$ below the temperature range simulated.

Phase Transition	optB86b-vdW	optB88-vdW	PBE-D3	PBE
Periclase/Brucite	362	$>$	344	326
Periclase/Artinite	369	371	341	322
Periclase/Nesquehonie	342	340	311	306
Periclase/Lansfordite	318	$<$	304	282
Brucite/Artinite	$>$	334	339	320
Brucite/Nesquehonite	334	312	298	299
Brucite/Lansfordite	308	$<$	294	275
Artinite/Nesquehonite	297	289.0	$<$	277
Artinite/Lansfordite	283	$<$	278	$<$
Nesquehonite/Lansfordite	274	$<$	289	$<$

Low p_{CO_2} and 1 bar p_{H_2O}

Figure 4.4 is the Gibbs free energy as a function of temperature phase diagram for optB86b-vdW using the lower limit of p_{CO_2} and 1 bar pressure for H_2O. At $\Delta\mu_{CO_2} = -1$ eV (low pressure conditions $p_{CO_2} = 10^{-8.8}$ bar) and $\Delta\mu_{H_2O} = 0$ eV (p_{CO_2}=1 bar) the most thermodynamically stable phase is predicted to be Brucite with a phase transition to Periclase at 362 K.

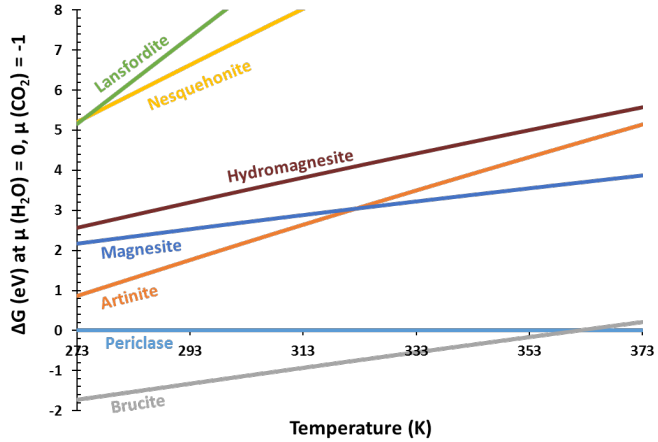

Figure 4.4: ΔG^0 as a function of T phase diagram at $\Delta\mu_{CO_2} = -1$ eV and $\Delta\mu_{H_2O} = 0$ eV for the functional optB86b-vdW.

Table 4.4 shows the predicted phase transitions that occur in the temperature range considered for all techniques. Results show consistent temperatures for phase transitions, across all techniques. Increasing temperature results in phases which contain less water per MgO unit becoming more thermodynamically stable. This is due to the loss of H_2O from these structures via evaporation.

Table 4.4: Temperature of phase transitions at $\Delta\mu_{CO_2} = -1$ eV and $\Delta\mu_{H_2O} = 0$ eV, where $>$ represents a phase transition that occurs above and $<$ below the temperature range simulated.

Phase Transition	optB86b-vdW	optB88-vdW	PBE-D3	PBE
Periclase/Brucite	362	$>$	343	326
Magnesite/Hydromagnesite	$<$	$<$	296	300
Magnesite/Artinite	322	349	$>$	328
Hydromagnesite/Artinite	$>$	$>$	$>$	357
Nesquehonite/Lansfordite	274	$<$	289	$<$

High p_{CO_2} and 1 bar p_{H_2O}

At $\Delta\mu_{CO_2} = 1$ eV (high pressure conditions) and $\Delta\mu_{H_2O} = 0$ eV (p_{CO_2}=1 bar) the most thermodynamically stable phase is predicted to be Magnesite across all temperatures simulated, similarly to $p_{CO_2} = p_{H_2O} = 1$ bar (Figure 4.3). As the formation of Magnesite is kinetically inhibited we must also consider the metastable phases. Whereas, previously (Figure 4.3) predicts that hydromagnesite is the second most thermodynamically stable phase across all temperature, at high pressures of CO_2 there are multiple phase transitions. At the lowest temperatures simulated ($T < 274$ K) Lansfordite is predicted the second most stable phase, between 274-308 K is Nesquehonite and at $T > 308$ K Hydromagnesite. As before increasing the temperature results in phase transitions associated with the loss of H_2O per MgO unit.

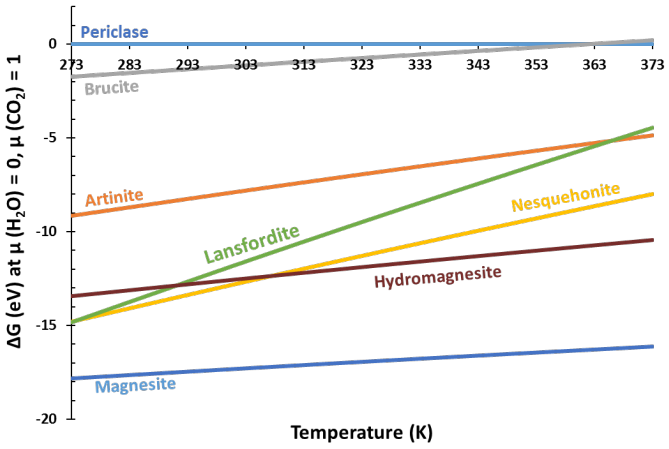

Figure 4.5: ΔG^0 as a function of T phase diagram at $\Delta\mu_{CO_2} = 1$ eV and $\Delta\mu_{H_2O} = 0$ eV for the functional optB86b-vdW.

Table 4.5 shows the predicted phase transitions that occur in the temperature range considered for all techniques. Results shows consistent temperature values for phase transitions, which are independent of the functional used.

Table 4.5: Temperature of phase transitions at $\Delta\mu_{CO_2} = 1$ eV and $\Delta\mu_{H_2O} = 0$ eV, where $>$ represents a phase transition that occurs above and $<$ below the temperature range simulated.

Phase Transition	optB86b-vdW	optB88-vdW	PBE-D3	PBE
Periclase/Brucite	362	$>$	344	326
Periclase/Lansfordite	$>$	337	$>$	$>$
Brucite/Lansfordite	$>$	326	$>$	$>$
Hydromagnesite/Nesquehonite	308	308	300	278
Hydromagnesite/Lansfordite	291	$<$	295	$<$
Artinite/Lansfordite	366	277	360	336
Nesquehonite/Lansfordite	274	$<$	289	$<$

In the long term storage of Magnox sludge only two phases will form (Brucite or Magnesite), under atmospheric p_{H_2O} and varied p_{CO_2}. However, in the intervening time period the phase formed will be a kinetically dominated process. This means that multiple phase transitions will occur, in the process of Magnesite's formation. Ostwald's step rule [92] gives an insight in to the crystallisation process. The rule states that nucleation from solution occurs in steps, where the most thermodynamically unstable phases forms first, followed by a step towards the most thermodynamically stable phase. It is important to note that this rule does not always hold true [93], however, increasing the number of polymorphs available increases the likelihood that Ostwald's rule applies [93]. This has implications for storage conditions, as varying the pressure can result in significantly different behaviour of metastable phases as a function of temperature. As Magnesite's formation is kinetically inhibited we must consider both the thermodynamically stable and the metastable phases.

4.4.2 Mg-Rich Mineral Phase Diagram at $\Delta G^{298\ K}$

In this section phase diagrams of all Mg-rich phases with the inclusion of temperature are presented, this is the next stage in the testing and evaluation of the thermodynamic framework. In addition, valuable insight in to the composition of Magnox sludge at relative atmospheric temperatures and a range of pressures will be gained. As in the previous section the vibrational entropy has been calculated and used to calculate the Gibbs free energy from $\Delta\mu$ = -1 to 1 eV, for all techniques. The range of $\Delta\mu$ has been decreased, to improve the resolution of the phase diagrams. Additionally, all phase transitions observed, occur within this range.

Figure 4.6 shows that at 1 bar pressure for both p_{CO_2} and p_{H_2O}, the most thermodynamically stable phase is Magnesite. This is in agreement with the predictions made in Section 4.3 and Section 4.4.1. In general all techniques simulated show excellent agreement, with small shifts in the pressures at which phase transitions occur. For a fixed $\Delta\mu_{CO_2}$ all phase transitions occur at consistent $\Delta\mu_{H_2O}$ values, however, the phase transition for Periclase/Brucite, using the technique optB88-vdW shows a negative shift relative to the other methods. For a given $\Delta\mu_{H_2O}$ PBE-D3 and PBE predicts that phase transitions occur at a larger (more positive) $\Delta\mu_{CO_2}$. This is due to these approaches failing to represent the weaker vdW interactions accurately.

To test the validity of these phase diagrams through experimental techniques is difficult, as changing the pressure of one reference state independently to the other can be difficult to achieve. One method of testing this is to put Magnesite under a vacuum and decrease the pressure of both CO_2 and H_2O simultaneously. This would be represented as a diagonal line on the phase diagram. The pressure at which Magnesite transforms to MgO could be determined and compared. Alternatively these phase diagrams could be adjusted to represent temperature as a function of pressure of CO_2. This would result in a phase diagram which is easier to compare to experiment, this will be considered in the next section.

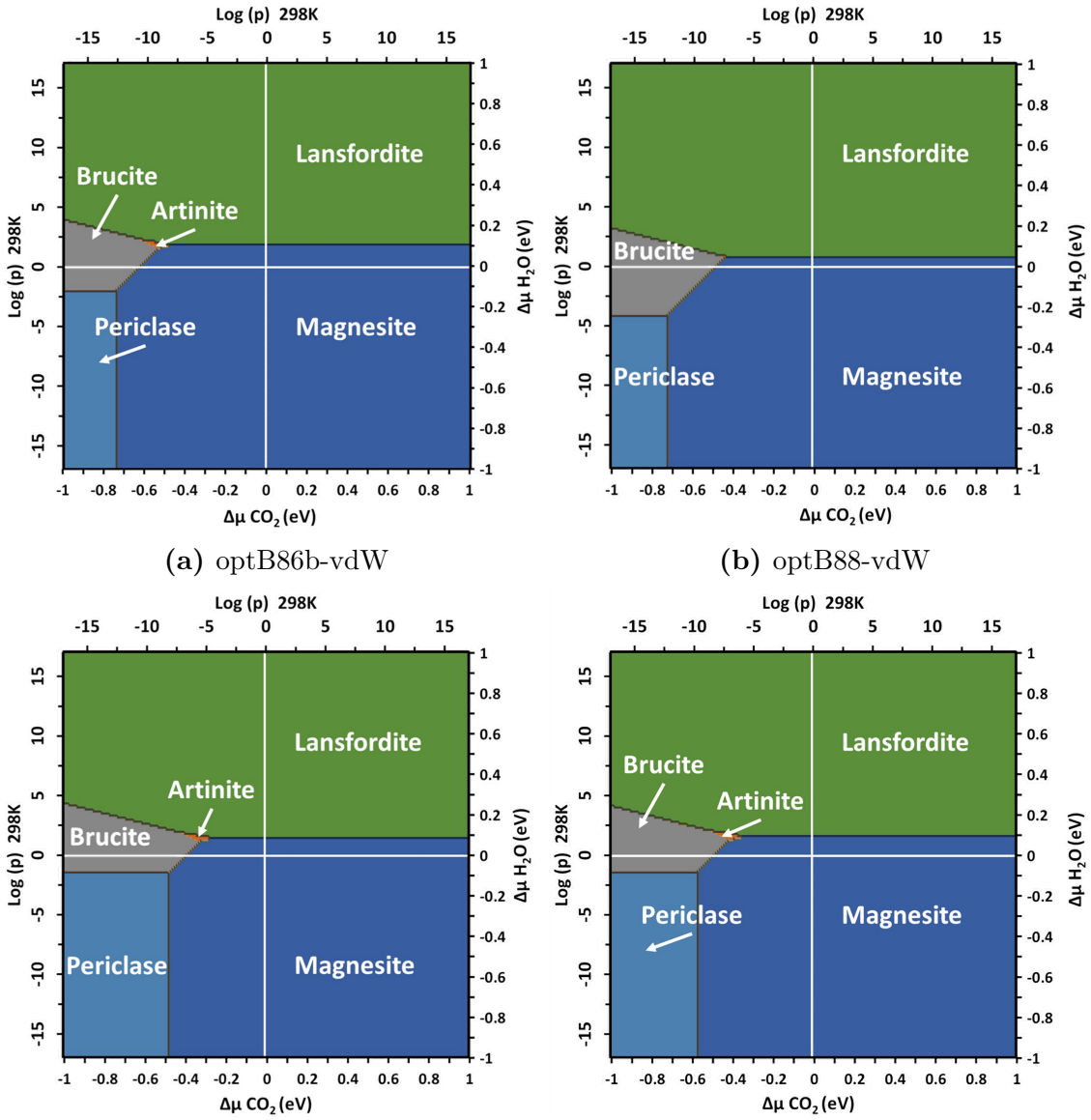

(a) optB86b-vdW **(b)** optB88-vdW

(c) PBE-D3 **(d)** PBE

Figure 4.6: Phase diagram of all Mg-rich phases at 298 K: ■ Periclase, ■ Magnesite, ■ Brucite, ■ Hydromagnesite, ■ Artinite, ■ Nesquehonite and ■ Lansfordite a) optB86b-vdW b) optB88-vdW c) PBE-D3 d) PBE. Solid white lines represents conditions of 1 bar pressure at 298 K.

4.4.3 Mg-Rich Mineral Phase Diagram: Temperature as a Function of $\Delta\mu_{CO_2}$ at $\Delta\mu_{H_2O} = 0$ eV

Figure 4.7 shows experimental phase diagrams of temperature as a function of p_{CO_2} at 1 bar p_{H_2O} [20, 22]. Both phase diagrams are based on the work of Langmuir *et al.* [19], but using new thermodynamic data to produce a more accurate phase diagram. Work by Hill *et al.* [22] shows that there are only two phases that are thermodynamically stable (Brucite and Magnesite). Whereas, Schott *et al.* [20] predicts that Magnesite is unstable and only forms at high p_{CO_2} and high temperatures. Additionally Schott *et al.* predicts a small region of Artinite which contradicts work by Hill *et al.*, although this agrees with work of Parry *et al.* [16]. Recent studies have found that Magnesite is the most thermodynamically stable phase at atmospheric conditions, but is kinetically inhibited [21]. Therefore, in the interim time period the metastable phases also need to be considered. These metastable phase transitions are denoted by a dashed line. It is important to note that although the phase diagrams look different the differences are due to small shifts in the conditions for phase transitions.

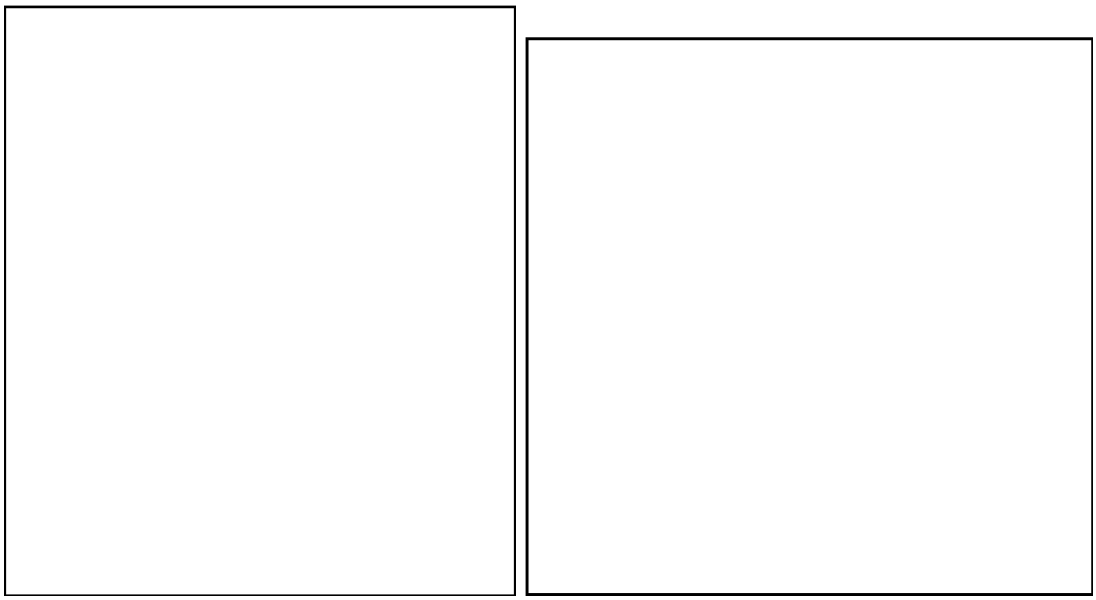

(a) Schott *et al.* [20] **(b)** Hill *et al.* [22]

Figure 4.7: Experimentally determined phase diagrams for selected Mg-rich phases. Temperature as a function - Log p_{CO_2}. Solid and dashed lines represent thermodynamic and metastable phase transitions respectively.

Figure 4.8 shows the optB86b-vdW, temperature as a function of $\Delta\mu_{CO_2}$ at $\Delta\mu_{H_2O} = 0$ eV phase diagram for all Mg-rich mineral phases and a metastable phase diagram. All other techniques simulated can be found in Appendix A.2. Similarly to the previous sections the vibrational entropy has been included in the calculation of the Gibbs free energy.

All functionals show excellent agreement with each other, with small but significant shifts in the values for phase transitions. Comparing the temperature for the phase transition of Periclase/Brucite across all techniques, for all Mg-rich phases, we

see temperature decreases in the order optB88-vdW (T > 373 K) > optB86b-vdW (363 K) > PBE-D3 (349 K) > PBE (325 K). Comparing this transition to experiment we see that optB88-vdW gives the best agreement, with optB86b-vdW also giving good representation of experiment. Additionally examining the metastable phase diagram we see that PBE-D3 and PBE phase transitions occur at lower temperatures compared to optB88-vdW and optB86b-vdW, which appear at similar temperatures. The reason the PBE functional is at such a low temperature is that it does not completely predict the interactions between Brucite layers. These shifts in the values are due to how different techniques represent vdW interactions. Shifts in the representation of Mg-rich phases can lead to different predicted phase diagrams and therefore, it is vital to correct for these shifts.

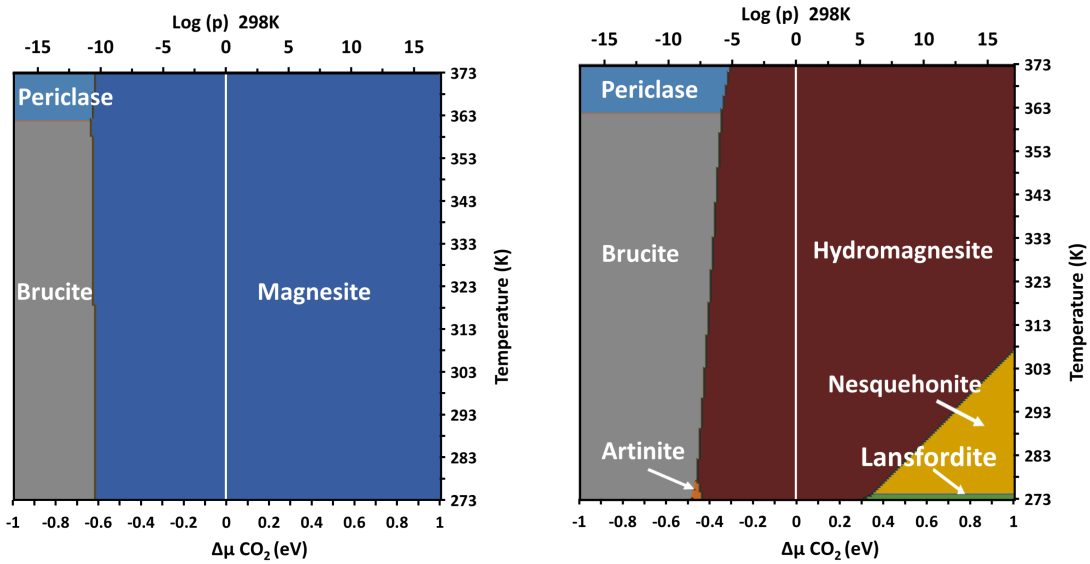

(a) Thermodynamic phase diagram: All Mg-rich phases

(b) Metastable phase diagram: with Magnesite inhibited

Figure 4.8: optB86b-vdW phase diagram of $\Delta\mu_{CO_2}$ as a function of temperature at $\Delta\mu_{H_2O} = 0$ eV: ■ Periclase, ■ Magnesite, ■ Brucite, ■ Hydromagnesite, ■ Artinite, ■ Nesquehonite and ■ Lansfordite. For the optB86b-vdW functional, where solid white line represents 1 bar pressure at 298 K.

It is also important to note that some of the theoretical phase diagrams predict a small region of Artinite at low temperatures, which is only present in some of the experimental phase diagrams [16, 20, 22]. This region of Artinite could be related to the fact that we use models to describe the structure (Section 3.1). Where the model used is not an accurate representation of Artinite's true structure. Alternatively, there is also debates in the literature surrounding the stability of Artinite, with a range values quoted for the entropy. Work by Schott *et al.* [20] predicts that Artinite is stable at low temperatures and p_{CO_2}. From this we can conclude that Artinite is a rare Mg-rich mineral phase with limited accurate thermodynamic data, making it difficult to verify whether Artinite's appearance in the phase diagram is an artefact of the calculation or is in fact an accurate representation of its thermodynamic properties.

Under atmospheric p_{CO_2} and a naturally occurring temperature range (0-30℃), there is only one phase present (Magnesite). Therefore, if the Magnox sludge was removed

from the storage ponds it would naturally form Magnesite. However, experiments have shown that its formation is kinetically inhibited [21] and therefore, in the interim time period we must consider the metastable phases. Under these conditions these calculations predict only one metastable phase will be present Hydromagnesite. Therefore, Hydromagnesite will most likely form a large part of the composition of Magnox sludge for most of its life, unless it is kept away from atmospheric CO_2, in which case it will be Brucite.

4.5 Conclusion

This chapter has enabled the evaluation of the composition of Mg-rich phases under a range of conditions. To summarise:

- Brucite, Magnesite and Periclase phase diagrams show that the methodology can reproduce experimental results accurately.
- optB86b-vdW gives the best agreement with experiment.
- Phase diagram of $\Delta\mu_{H_2O}$ as a function of $\Delta\mu_{CO_2}$ for all Mg-rich Phases shows Magnesite most thermodynamic stable at atmospheric conditions. As also demonstrated by the work of Chaka *et al.* [23].
- Temperature as a function of $\Delta\mu_{CO_2}$ phase diagrams with optB86b-vdW reproduces the experimental phase diagram (Figures 4.1a and 4.1c), with:
  - Constant shift in the pressures due to the different DFT techniques, gives the possibility of applying a correction.
  - At ambient conditions the most thermodynamically stable phase is Magnesite, unless its inhibited which results in Lansfordite/Hydromagnesite being predicted as the most thermodynamically stable.
  - As temperature increases phases with less water per MgO unit are more favoured.

Having established the relative stability of the phases present, the next step is to investigate the adsorption of radio-nuclei. Time constraints means that only one system can be considered, and due to its importance, in terms of the current composition of the sludge, Brucite has been selected.

5 Surface Phase Diagrams

The exact composition of Magnox sludge is currently under discussion in the literature with one study showing that Brucite is the predominate phase present [94]. Hence, this chapter will focus on investigating the absorption of one of the important radio-nuclides, ^{90}Sr, on the two most stable surfaces of Brucite ({001} and {100}), which will enable the effect of surface structure to be considered. In addition, as in the earlier chapters, where the results show that the bulk phases are highly dependant on the partial pressures of H_2O and CO_2 the behaviour of the surfaces will also be investigated. This will provide vital evidence for the composition of Magnox sludge under a range of conditions, which are relevant to storage conditions.

The aims of this chapter are:

- Outline a thermodynamic framework, which can be used to evaluate stability of surfaces.
- Investigate the interactions of H_2O, CO_2 and radio-nuclei with Brucite surfaces.
- Predict the most stable surface and composition of Brucite with adsorbed ^{90}Sr as a function of p_{CO_2} and p_{H_2O}.

5.1 Methodology

The surfaces presented in this chapter have been produced by cutting bulk crystals along Miller indices. However, each cut can have multiple different terminations, which can lead to variation in surface energies and stabilities. Additionally, some cuts will result in a dipole moment perpendicular to the surface, Bertaut *et al.* [95] has shown that the energy, for these surfaces, will diverge and become infinite. Tasker *et al.* [96] has identified that there are three different types of surfaces (Figure 5.1).

- Type I - Has a repeat unit of neutral planes where the cations and anions are in a stoichiometric ratio.
- Type II - Charged planes where the unit cell consists of multiple layers, so that there is no overall dipole perpendicular to the surface.
- Type III - Similar to type II surfaces, however, the unit cell consists of multiple layers with an overall dipole moment perpendicular to the surface.

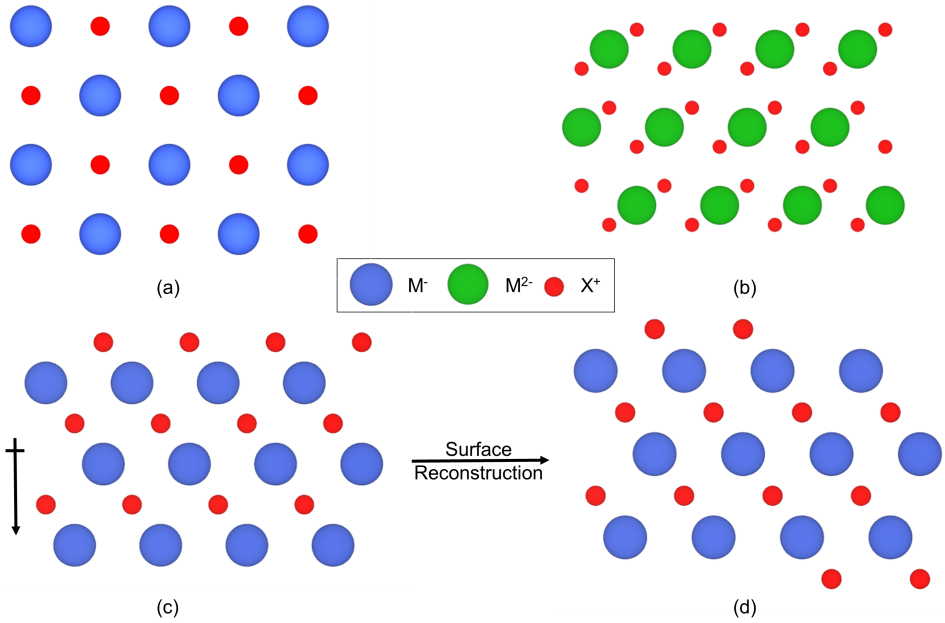

Figure 5.1: Different type of surfaces. (a) Type I, (b) Type II, (c) Type III surface containing a dipole, and (d) Type III surface after reconstruction to remove dipole moment.

Type I and II are both stable surfaces, however, the net dipole moment in type III surfaces needs to be resolved, before converged surface energies can be calculated. In nature these surfaces are stabilised through defects or reconstructions. Practically, in order to allow simulation of these surfaces, the net dipole is removed by taking half of the first layer and moving it to the bottom of the crystal. This has the effect of removing the net dipole from the surface, a consequence of this approach is that it gives rise to a large range of configurations, of which only the most stable configuration is used.

5.1.1 Surface Generation

The DFT code VASP, assumes 3D periodic boundary conditions and hence when modelling surfaces we generally use the slab method. A slab containing two surfaces and a vacuum gap between, is modelled. The surface energy (γ) can be explicitly defined and calculated using Equation 5.1. Where $n_{Mg(OH)_2}$ is the number of repeat bulk units forming the surface and S is the surface area.

$$\gamma = \frac{E_{Surf} - n_{Mg(OH)_2} E_{Mg(OH)_2}}{2S} \tag{5.1}$$

This approach assumes that the top and bottom of the slab is identical and hence the absolute surface energies can be directly compared. If the top and bottom of the slab are not identical we apply a surface approach, where the bottom surface is held fixed in the equilibrium positions, in which case we evaluate the change in surface energy. So if we have a defective surface, $E_{defsurf}$ we can evaluate the

change of surface energy by comparing with the pure slab energy, E_{surf} and the self energy of defect (or dopant), which may be water, CO_2 or ($Sr(OH)_2$ replacing $Mg(OH)_2$) as E_{dop}. It is assumed that this bottom region for all surfaces has the same minimisation and hence surface energies can be calculated using,

$$\gamma = \frac{U_S - U_B}{S} \tag{5.2}$$

$$\delta\gamma = \frac{E_{defsurf} - (E_{Surf} + nE_{dop})}{S} \tag{5.3}$$

Where n is the number of defects added to the surface. This method is less computationally expensive, however, only the relative energies can be compared. The extra consideration when using the VASP code is to remove the effect of the surface dipole created by top and bottom surfaces relaxing differently). In this work all surfaces were created using the METADISE code [97] and surface approach.

5.1.2 Phase Diagrams

The phase diagrams presented in this chapter have been produced using the Surphadia program [98], by calculating surface free energies. The free energy of the surfaces are corrected to account for the adsorbates, added to each surface. Specifically the amount of H_2O and CO_2 absorbed on to the surface (Equation 5.4). Where n is the number of species in the surface calculation and $\Delta\mu$ is the change in chemical potential.

$$\gamma = \frac{1}{S}\left(E_{Surf} - n_{Mg(OH)_2}\mu_{Mg(OH)_2} - n_{H_2O}\mu_{H_2O} - n_{CO_2}\mu_{CO_2}\right) \tag{5.4}$$

As the system is in equilibrium, the energy of the bulk system can be used to calculate the change in chemical potential, this assumes that the entropic effects are negligible (Equation 5.5), where m is he number of unit cells in the bulk system and $E_{Mg(OH)_2}$ is the energy of bulk Brucite.

$$G_{Mg(OH)_2} = E_{Mg(OH)_2} = m\mu_{Mg(OH)_2} \tag{5.5}$$

The excess (Γ) is defined for H_2O and CO_2 in Equation 5.6 and 5.7 respectively.

$$\Gamma_{CO_2} = \frac{1}{S}n_{CO_2} \tag{5.6}$$

$$\Gamma_{H_2O} = \frac{1}{S}n_{H_2O} \tag{5.7}$$

By combining Equations 5.4 to 5.6 we can define an equation for calculating the surface free energy due to a change in the partial pressure of CO_2 and H_2O (Equation 5.8).

$$\gamma = \frac{1}{S}\left(E_{Surf} - \frac{n_{Mg(OH)_2}}{m}E_{Mg(OH)_2}\right) - \Gamma_{H_2O}\Delta\mu_{H_2O} - \Gamma_{CO_2}\Delta\mu_{CO_2} \tag{5.8}$$

The calculation of chemical potentials and the inclusion of temperature use the same methodology as outlined in Section 4.2.

5.2 Brucite Surfaces

The crystal morphology for Brucite has experimentally been shown to be a hexagonal plate like structure. The crystal is comprised primarily of 3 surfaces; {001} is the largest flat surface, {100} form the 6 edges of the hexagon and the {101} is a small surface which occasionally forms between two {100} surfaces.

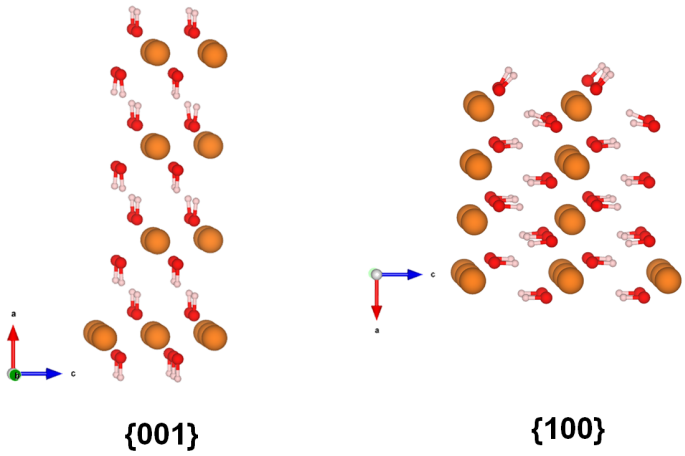

Figure 5.2: Structure of {001} and {100} Brucite surfaces. Mg in orange, H in white and O in red.

This work focuses on the two largest surface present in the crystal morphology ({001} and {100}). To fully understand the composition of Magnox sludge and its interactions, it is vital to extend the study to also include surfaces in addition to bulk analysis. Surfaces are the first point of contact between the sludge and its extended environment and as such analysis of these will provide insights in to this complex problem. The sludge is currently being stored underwater with a high partial pressure of CO_2, hence, the interactions between surfaces and H_2O/CO_2 will be of great importance.

Defect surfaces in this chapter can be split in to four distinct groups:

- Hydrated surfaces (III, V-VII) where there is a variation of 1-4 H_2O molecules adsorbed on to the surface (Figure 5.3).
- Carbonated surfaces (II, IV) where 1-2 CO_2 molecules are adsorbed on to the surface (Figure 5.4).

- Dehydrated surfaces (VIII, XII) where 1-2 H_2O molecules have been removed from the surface leaving 1 or 2 oxygen ions (Figure 5.5 and 5.6).
- Dehydrated surfaces where 1-2 H_2O molecules have been removed from the surface before being hydrated/carbonated (IX-XII, XIV-XVIII) *e.g.* 50% dehydration, 50% carbonation and 100% hydration (Figure 5.5 and 5.6).

Table 5.1 summarises all the different defect surfaces studied and is presented with the surface index, which is used to identify the surface that appears in the phase diagram section and an acronym for each surface to aid in identification. Where 1C represents one additional CO_2, 1H is one additional H_2O, P is the pure structure and X1 is one H_2O molecule removed from the pure surface.

Table 5.1: Composition of defective Brucite surfaces and associated number/label, where P is Pure, nC and nH represent the number of additional CO_2 and H_2O respectively and X is the number of H_2O molecules that have been removed.

Index	**Label**	**Surface**
I	P	Pure Surface
II	1C	50% Carbonation
III	1H	25% Hydration
IV	2C	100% Carbonation
V	2H	50% Hydration
VI	3H	75% Hydration
VII	4H	100% Hydration
VIII	X1	-25% Hydration
IX	X1-1C-1H	50% Carbonation
X	X1-1C-2H	50%,Carbonation, 25% Hydration
XI	X1-1C-3H	50%,Carbonation, 50% Hydration
XII	X1-1C-4H	50%,Carbonation, 75% Hydration
XIII	X2	-50% Hydration
XIV	X2-2C	100%,Carbonation, -50% Hydration
XV	X2-2C-1H	100%,Carbonation, -25% Hydration
XVI	X2-2C-2H	100%,Carbonation
XVII	X2-2C-3H	100%,Carbonation, 25% Hydration
XVIII	X2-2C-4H	100%,Carbonation, 50% Hydration

Figures 5.3 to 5.6 represents the minimised structures for the {001} surfaces of Brucite in different conditions as highlighted by Roman numerals and description in Table 5.1. Additional representations of the {100} surfaces can be found in Appendix B. The carbonation and hydration of the pure sureface result in H_2O and CO_2 molecules being adsorbed on to the surface of Brucite. It is important to note the addition of a CO_2 molecule to the dehydrated surface results in the formation of carbonate ions. Whereas, O^{2-} ions are formed during the dehydration

of stoichiometric surfaces, as for every OH^- ion removed a H atom is removed from the surface to enable a full molecule of water to be extracted from the surface.

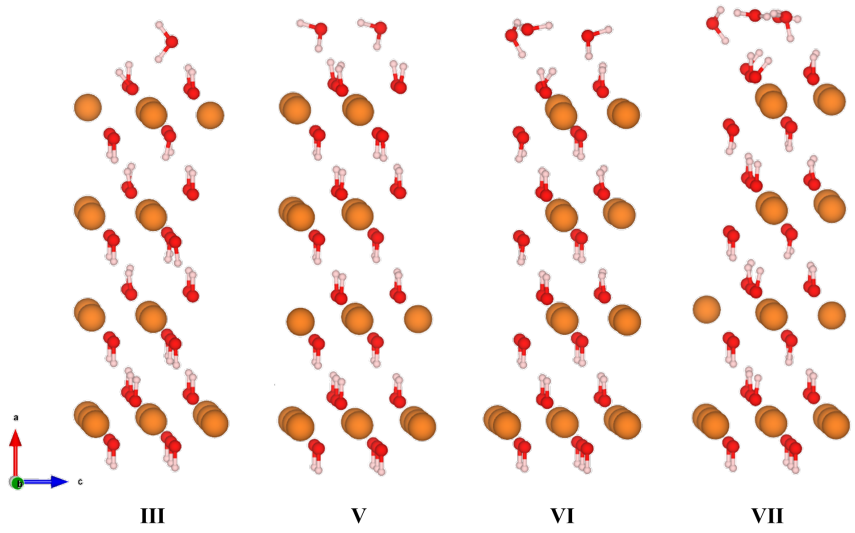

Figure 5.3: Brucite {001} Surface including H_2O: III) 1H, V) 2H, VI) 3H and VII) 4H. Mg in orange, H in white and O in red.

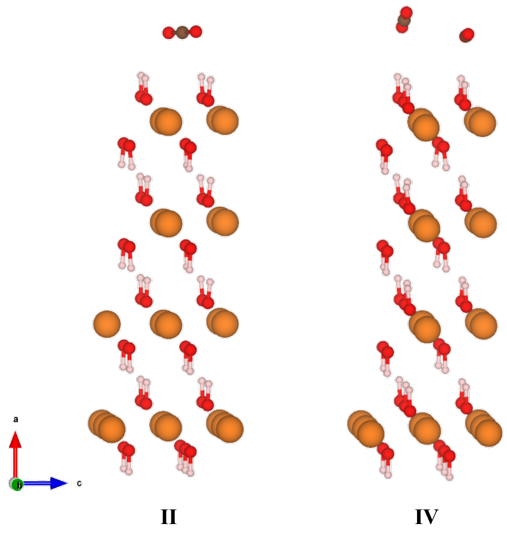

Figure 5.4: Brucite {001} Surface including CO_2: II) 1C and IV) 2C. Mg in orange, C in grey, H in white and O in red.

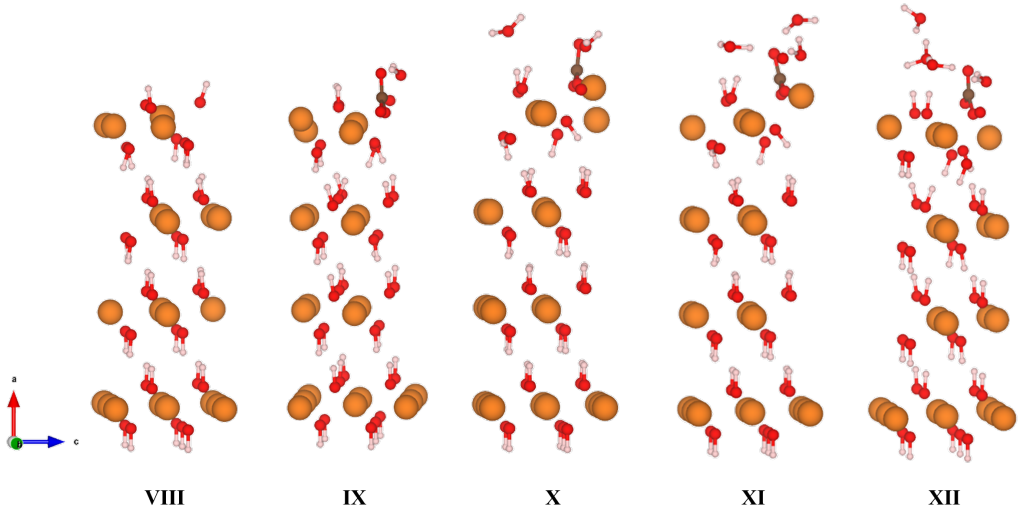

Figure 5.5: {001} X1 surface including varying H_2O with 1 CO_2: VIII) X1, IX) X1-1C-1H, X) X1-1C-2H, XI) X1-1C-3H and XII) X1-1C-4H. Mg in orange, C in grey, H in white and O in red.

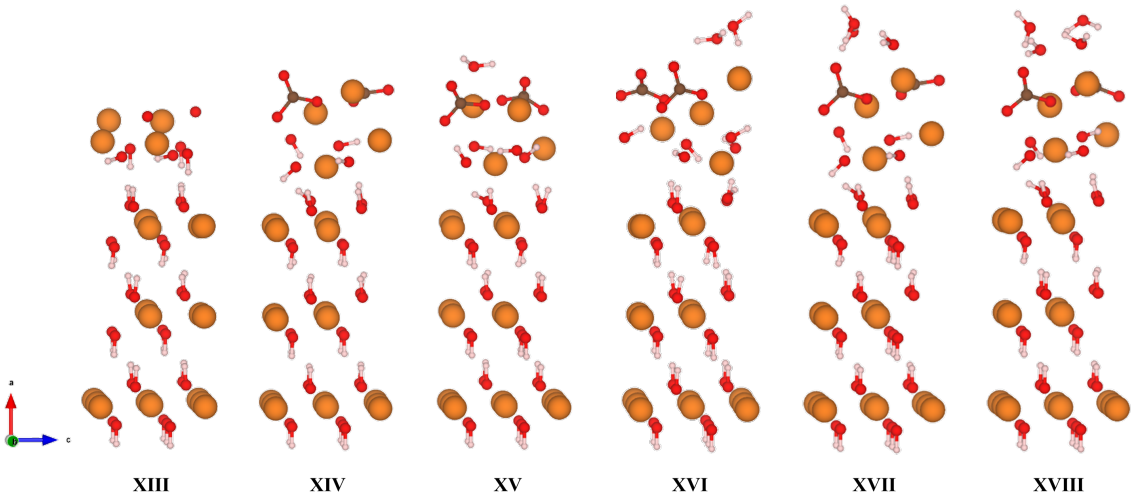

Figure 5.6: {001} X2 surface including varying H_2O with 2 CO_2: XIII) X2, XIV) X2-2C, XV) X2-2C-1H, XVI) X2-2C-2H , XVII) X2-2C-3H and XVIII) X2-2C-4H. Mg in orange, C in grey, H in white and O in red.

5.2.1 Surface Energies

Table 5.2 shows the defect energy (ΔE) which is the difference in E_{Def} for pure and defect surfaces, where E_{Def} is calculated using,

$$E_{\text{Def}} = E_{\text{surf}} - aE_{CO_2} - bE_{H_2O} \tag{5.9}$$

$$\Delta E = E_{\text{Def}} - E_{\text{Pure}} \tag{5.10}$$

This gives relative energies which enables comparison between the different surfaces. The primary difference between the two surfaces is that the {100} surfaces have a more favourable absorption energy for defects compared to the equivalent {001} counterparts. This indicates that the {100} surface is more reactive than the {001}, as the defect surfaces of the {100} has more favourable absorption energies. The increase in defect stability for the {100} surface is due to the higher coordination that surface Mg-ions can achieve. Where all configurations have higher or the same coordination than the {001} equivalents.

The addition of H_2O and CO_2 to both surfaces decreases the energy and increases the defect stability. However, care needs to be taken with the values for H_2O, as the stability changes depending on the reference state for H_2O used *e.g.* relative to gaseous, liquid or solid H_2O. All calculations are calculated relative to the gas phase. However, if we compare to liquid water through the addition of ΔH_f^{Vap} to the energies presented, results in an increase to the surface energy (surfaces being less stable). If we examine surface III for the {001} surface $\Delta E = -0.45\ eV$ relative to gaseous H_2O and for liquid water $\Delta E = 0.01\ eV$, whereas, for the {100} surface $\Delta E = -0.82\ eV$ relative to gaseous H_2O and for liquid water $\Delta E = -0.37\ eV$. The {001} surface now has an unfavourable defect energy by changing the reference point.

Dehydrating the surface, giving compositions (VIII, XIII and XIV in Table 5.2) results in an unstable defect energy for both surfaces suggesting this process is unfavourable. Hydrating/Carbonating the 50% dehydrated surface results in a stabilisation of the defect surface and a favourable defect energy for both surfaces. However, only the {100} is stable when hydrating/carbonating the 100% dehydrated surface (XIII - XVIII). This is due to the higher coordination that {100} surface Mg-ions can achieve. This stabilises the defective surface and indicates that {100} is more reactive that the {001} surface.

Comparing the defect surface energies for both surfaces has shown how coordination of the surface ions impacts the stability of a surface, where more highly coordinated surfaces are more stable. Additionally, simulations predict that hydrating/carbonating a surface helps to stabilise a defective surface, ensuring that the Mg coordination at the surface is as close to 6 as possible. Furthermore, energies calculated in this section can be used to generate phase diagrams under varying partial pressures of H_2O and CO_2. This will enable a visual comparison of surface stability under a range of conditions and will be presented in the next section.

Table 5.2: Defect energies (eV) for Brucite surfaces, where all surface energies are calculated relative to gaseous H_2O and CO_2. P is Pure, nC and nH represent the number of additional CO_2 and H_2O respectively and X is the number of H_2O molecules that have been removed. Surface area (S) for {001} = 34.5 Å and {100} = 58.7 Å.

Index	**Label**	ΔE **(eV)**	
		{001}	**{100}**
I	P	0.00	0.00
II	1C	−0.23	−0.35
IV	2C	−0.53	−0.73
III	1H	−0.45	−0.82
V	2H	−1.10	−1.43
VI	3H	−1.73	−2.27
VII	4H	−2.45	−3.08
VIII	X1	3.31	2.57
IX	X1-1C-1H	0.08	−1.10
X	X1-1C-2H	−0.63	−1.85
XI	X1-1C-3H	−1.30	−3.25
XII	X1-1C-4H	−1.95	−3.22
XIII	X2	6.70	6.04
XIV	X2-2C	2.77	1.05
XV	X2-2C-1H	2.04	−0.63
XVI	X2-2C-2H	0.40	−1.31
XVII	X2-2C-3H	−0.01	−2.62
XVIII	X2-2C-4H	−0.02	−3.26

5.2.2 Surface Phase Diagrams

This section presents the surface phase diagram for {001} and {100} surfaces of Brucite. The free energies for solid phases have been calculated neglecting temperature effects on the surface and using the equations presented in Section 5.1.2. Due to the large size of the simulation cell a complete vibrational analysis has not been performed, hence, the energies do not include the zero point energy (ZPE). The phase diagrams show the most stable configuration under a range of partial pressures of CO_2 and H_2O, where the dashed line is 1 bar pressure at 0 K and the solid line is 1 bar pressure at 298 K. The blue colour represents hydrated phases, grey for dehydrated, red for carbonated and dark red/purple for phases which are both hydrated and carbonated.

Figure 5.7 is the surface phase diagram for the {001} surface. Increasing the partial pressure of CO_2 increases the stability of phases which are carbonated, as expected. This can be seen at a $\Delta\mu_{H_2O} = -1\ eV$, where increasing p_{CO_2} induces a phase

transition from pure surface to a 100% carbonated surface. Additionally, increasing p_{H_2O} favours hydrated surfaces. This can be observed at $\Delta\mu_{CO_2} = 0\ eV$, where increasing p_{H_2O}, induces a phase transition from X2-2C (XIV) to 2C (IV) and then a second transition to a surface with a complete mono-layer of H_2O adsorbed (VII).

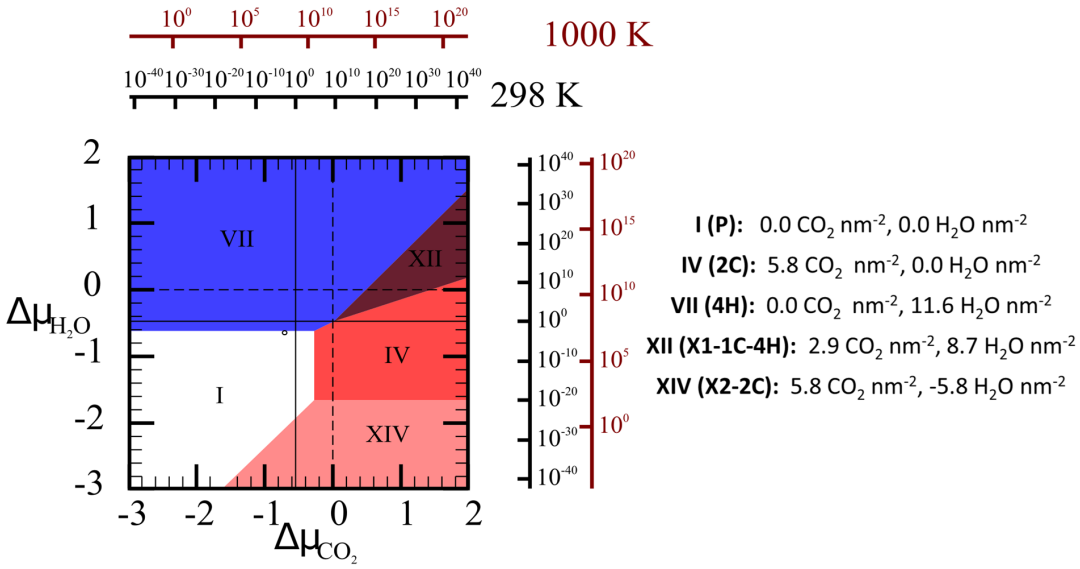

Figure 5.7: {001} surface phase diagram calculated using optB86b-vdW, where the dashed line is 1 bar pressure at 0 K and the solid line is 1 bar pressure at 298 K. White circle represents; 400 ppm CO_2 and 32 mbar of H_2O at 298 K (atmospheric conditions). Visual representations of the different surfaces can be found in Appendix B and Figures 5.3 to 5.6.

Figure 5.8 is the {100} surface phase diagram for Brucite. Similar to the {001} diagram, increasing the p_{CO_2} and p_{H_2O} increases the stability of carbonated and hydrated surfaces, respectively. However, there are a few key differences between the two phase diagrams. The first observation of note is the increased number of defect phases present in the {100} phase diagram. This is a result of the higher coordination numbers which the surface Mg-ion can achieve, which allows for the accommodation of a larger number of defect configurations. Additionally the pure surface has a much smaller area on the {100} phase diagram. Indicating that the pure surface has far fewer conditions at which it is the most thermodynamically stable phase. This implies that the {100} surface is more reactive that the {001} surface, which again can be associated to the larger coordination numbers.

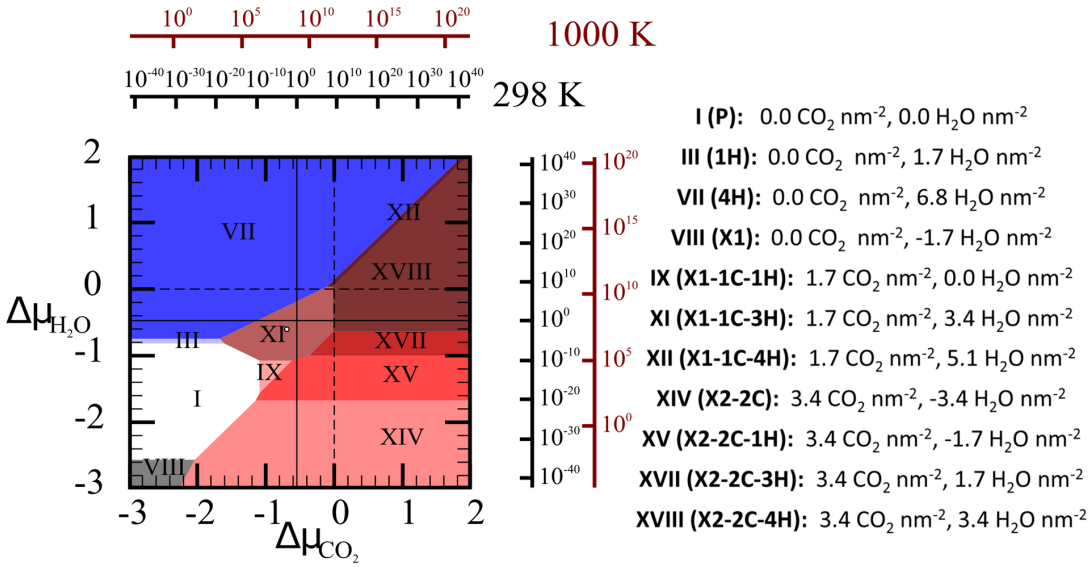

Figure 5.8: {100} surface phase diagram calculated using optB86b-vdW, where the dashed line is 1 bar pressure at 0 K and the solid line is 1 bar pressure at 298 K. White circle represents; 400 ppm CO_2 and 32 mbar of H_2O at 298 K (atmospheric conditions). Visual representations of the different surfaces can be found in Appendix B and Figures 5.3 to 5.6.

Table 5.3 shows the most thermodynamically stable phase at various conditions for the {001} and {100} surfaces. At atmospheric conditions the pure surface for {001} is the most stable, whereas, the {100} is more stable as a partially hydrated and carbonated surface (X1-1C-3H). This indicates that at atmospheric conditions the {100} surface of Brucite would readily adsorb H_2O and CO_2, whereas, the {001} surface would not. Although in the case of the {001} surface, the phase boundary (as noted by the small white circle) is close to ambient conditions, and hence it may be expected that the amount of adsorbed water will be dependent on the humidity, and that at high humidity, water will be seen to adsorb.

Investigation of the surface energies and phase diagrams has given valuable insight in to the surface conformation and interactions of Brucite, with H_2O and CO_2. The next section will expand upon this by doping these surfaces with ^{90}Sr. This will enable us to study Brucite's interactions with radio-nuclei, under wet and carbonated conditions.

Table 5.3: Predicted thermodynamically most stable defective surface pf Brucite at a range of reference conditions for {001} and {100} surfaces. P is Pure, nC and nH represent the number of additional CO_2 and H_2O respectively and X is the number of H_2O molecules that have been removed. Visual representations of the different surfaces can be found in Appendix B and Figures 5.3 to 5.6.

Conditions	**{001}**		**{100}**	
	Surface	**Label**	**Surface**	**Label**
400 ppm CO_2, 32 mbar H_2O at 298 K	I	P	XI	X1-1C-3H
1 bar CO_2, 1 bar H_2O at 298 K	VII	4H	XI	X1-1C-3H
1 bar CO_2, 1 bar H_2O at 0 K	VII	4H	XVIII	X2-2C-4H
			XI	X1-1C-3H

5.3 Strontium Doped Brucite Surfaces

The surfaces minimised in Section 5.2.1 will now be doped with a single ^{90}Sr atom. This will form the foundations of analysing the interactions of Magnox sludge with radio-nuclei. ^{90}Sr has been chosen as the ideal candidate, due to its short half life ($\approx$ 30 years), therefore it will be present in the storage pond in large quantities. Hence, it is vital to understand the interaction with nuclear sludge and determine if it has been incorporated in to the sludge bulk structure. This result would influence the storage strategy required for Magnox sludge and how it is processed.

Table 5.4 Shows the ΔE and solution energies for ^{90}Sr doped surfaces. ΔE is calculated the same as in Section 5.2.1 (Equation 5.9), where the energy for each surface is relative to the doped 'pure' surface (*i.e.* surface with a single ^{90}Sr adsorbed) and values are corrected for additional CO_2 and H_2O molecules adsorbed.

The solution energy is calculated using Equation 5.11, where E_{Surf} is the energy of the undoped surface, $E_{Sr(OH)_2}$ and $E_{Mg(OH)_2}$ are the energy of bulk strontium hydroxide and Brucite, respectively. E^{Sr}_{Surf} is the energy of the doped surface. This enables direct comparison between doped and undoped structures.

$$E_{sol} = E^{Sr}_{Surf} + E_{Mg(OH)_2} - E_{Surf} - E_{Sr(OH)_2} \tag{5.11}$$

Comparing the ΔE values for all doped and undoped structures, indicates that the doped structures (Table 5.4) have a more favourable energy value, compared to the undoped structures (Table 5.2). This is due to the destabilising effect the larger ^{90}Sr ion has on the pure surface. Similar to Section 5.2.1 the ΔE shows that the addition of H_2O and CO_2 decreases the surface energy. This is due to the adsorbate stabilising an unfavourable defect, via increasing the coordination that the ^{90}Sr ion can achieve.

Dehydrated surfaces doped with ^{90}Sr results in a ΔE value which is more favourable than the undoped equivalent. However, both values are still unfavourable in relation

Table 5.4: Defect energies (eV) for doped Brucite surfaces, where all energies are calculated relative to gaseous H_2O and CO_2. P is Pure, nC and nH represent the number of additional CO_2 and H_2O respectively and X is the number of H_2O molecules that have been removed. Surface area (S) for {001} = 34.5 Å and {100} = 58.7 Å.

Surface	**Label**	ΔE		E_{Sol}	
		{001}	**{100}**	**{001}**	**{100}**
I	P	0.00	0.00	1.21	0.53
II	1C	−0.42	−1.04	1.02	−0.16
IV	2C	−0.85	−1.33	0.88	−0.07
III	1H	−0.19	−0.78	1.46	0.57
V	2H	−1.36	−1.93	0.94	0.03
VI	3H	−2.00	−2.91	0.94	−0.11
VII	4H	−2.42	−3.32	1.23	0.29
VIII	X1	2.47	2.11	0.36	0.07
IX	X1-1C-1H	−0.58	−1.37	0.54	0.26
X	X1-1C-2H	−1.36	−2.41	0.48	−0.03
XI	X1-1C-3H	−1.95	−3.26	0.56	0.52
XII	X1-1C-4H	−2.66	−3.66	0.50	0.09
XIII	X2	4.99	4.24	−0.50	−1.27
XIV	X2-2C	0.45	−0.56	−1.12	−1.08
XV	X2-2C-1H	0.01	−1.90	−0.83	−0.74
XVI	X2-2C-2H	−1.84	−2.15	−1.03	−0.31
XVII	X2-2C-3H	−1.96	−2.85	−0.75	0.30
XVIII	X2-2C-4H	−2.51	−3.39	−1.29	0.40

to the 'pure' structures. The addition of a ^{90}Sr ion to the pure surface destabilises the surface increasing its energy, giving a more favourable ΔE between 'pure' and dehydrated surfaces. The removal of H_2O from the surface is even more favourable, due to the ^{90}Sr having more space to relax.

Structures IX-XII for the {001} surface now show ΔE values which are favourable compared to the undoped counterparts (Table 5.2). Hence hydrating/carbonating increases the coordination fo the surface ^{90}Sr-ion, which results in stabilisation of the dopant. For the {100} surfaces the ΔE values are slightly more favourable than the undoped, but are largely unchanged.

The majority of the configurations show an unfavourable solution energy for structures doped with ^{90}Sr. This indicates that under 1 bar p_{H_2O} and p_{CO_2} ^{90}Sr defects are unstable. This is due to the larger size and higher coordination requirements of the ^{90}Sr ion compared to Mg. This induces strain on the structure and increases the energy. There is a fluctuation in some of the values which is a result of the variation

in the coordination number of the ^{90}Sr ion, from 6 to values closer to 8.

The {100} surface has favourable solution energies for carbonated and some hydrated surfaces (II, IV, VI, X), which the {001} does not show, indicating that {100} is more reactive towards ^{90}Sr. The stabilisation is attributed to the H_2O and CO_2 molecules coordinating to the ^{90}Sr ion and increasing the coordination, to that which is closer to ^{90}Sr ideal coordination. Combining this with the {100} favourable free energy for forming hydrated surfaces under wet conditions, discussed in Section 5.2.1, implies that {100} surface will adsorb ^{90}Sr on to the surface. This is important as Magnox sludge has been found to be primarily comprised of Brucite and is stored underwater. Hence, there is a probability that ^{90}Sr is incorporated in to the sludge composition. Therefore, when evaluating plans for the process and storage of the sludge, careful consideration needs to be taken due to the high probability of radio-nuclei being present in the sludge composition. However, surface VII (hydrated) does not show a favourable solution energy. This is likely due to the H-bonding network of water molecules on the surface being broken by the now uneven surface. The addition of multiple layers of water could counteract this effect and again result in a favourable solution energy for the adsorption of ^{90}Sr, in wet conditions.

This section has evaluated the energies associated with the doping of surfaces with a single ^{90}Sr ion. However, they have not been evaluated in relation to partial pressures of CO_2 and H_2O. The next section will address this by applying the phase diagram methodology used for the non-Sr doped surface (Section 5.2.2) to the ^{90}Sr doped surfaces.

5.3.1 Strontium Doped Brucite Surface Phase Diagram

This section presents the surface phase diagrams for ^{90}Sr doped Brucite. As with the undoped surfaces (Section 5.2.2), phase diagrams have been produced without the inclusion of temperature effects and not including the ZPE. The phase diagrams show the most stable configuration under a range of partial pressures of CO_2 and H_2O. Where the dashed line is 1 bar pressure at 0 K and the solid line is 1 bar pressure at 298 K. The blue colour represents hydrated phases, grey for dehydrated, red for carbonated and dark red/purple for phases which are both hydrated and carbonated.

Figure 5.9 and 5.10 are the ^{90}Sr doped phase diagrams for the {001} and {100} surfaces and are comparable to those presented in Section 5.2.2. Where increasing the p_{CO_2} and p_{H_2O} increases the stability of carbonated and hydrated phases respectively. Under ambient conditions ^{90}Sr will co-adsorb with carbonate. The phase diagrams have a few key differences compared to the undoped system. The first observation is the decrease in size of the 'pure' surface region. This is due to the destabilising effect of ^{90}Sr on the pure surface, making it thermodynamically unfavourable. The destabilising effect of the ^{90}Sr can be attributed to the much larger size of the ion, which cannot achieve its optimal coordination, disrupting the surface.

There is an increased number of defect phases present in the doped {001} phase diagram, specifically surfaces which have been dehydrated before being hydrated and

carbonated. These surfaces have the advantage of being able to fully reconstruct. This allows for higher coordination of the ^{90}Sr-ion. The final difference is the decreased stability of the mono-layer (VII), which has been replaced by a surfaces with a lower concentration of adsorbed H_2O molecules. The larger size of the ^{90}Sr-ion has disrupted the flat surface of Brucite, which has resulted in breaking the H-bonding network of the mono-layer, increasing the surface energy. This could possibly be overcome by rearranging the surface H_2O molecules to give better overlap or via increasing the number of solvation layers in the system.

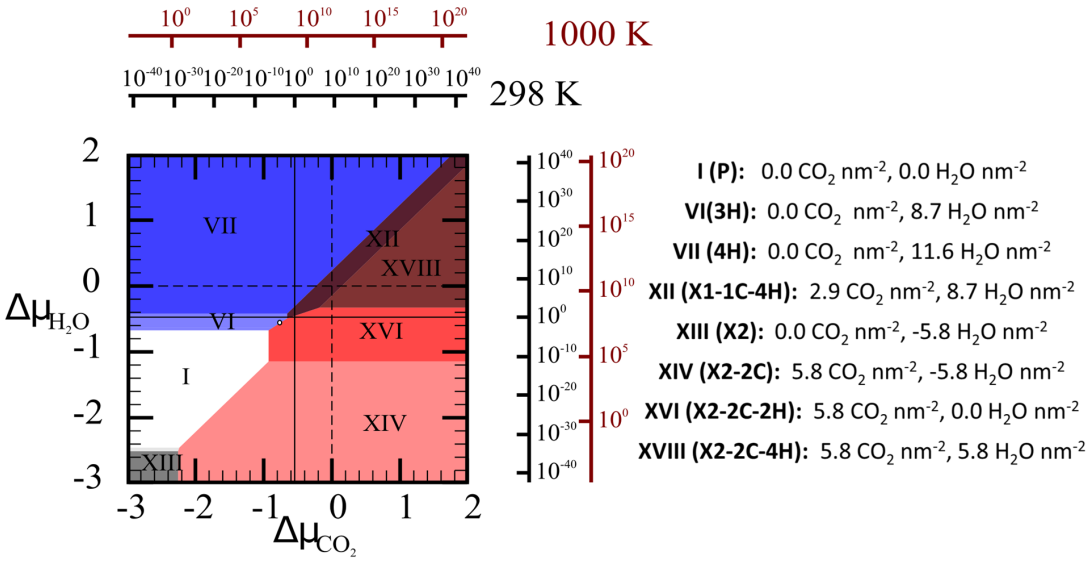

Figure 5.9: {001} ^{90}Sr surface phase diagram calculated using optB86b-vdW, where the dashed line is 1 bar pressure at 0 K and the solid line is 1 bar pressure at 298 K. White circle represents; 400 ppm CO_2 and 32 mbar of H_2O at 298 K (atmospheric conditions). Visual representations of the different surfaces can be found in Appendix B.

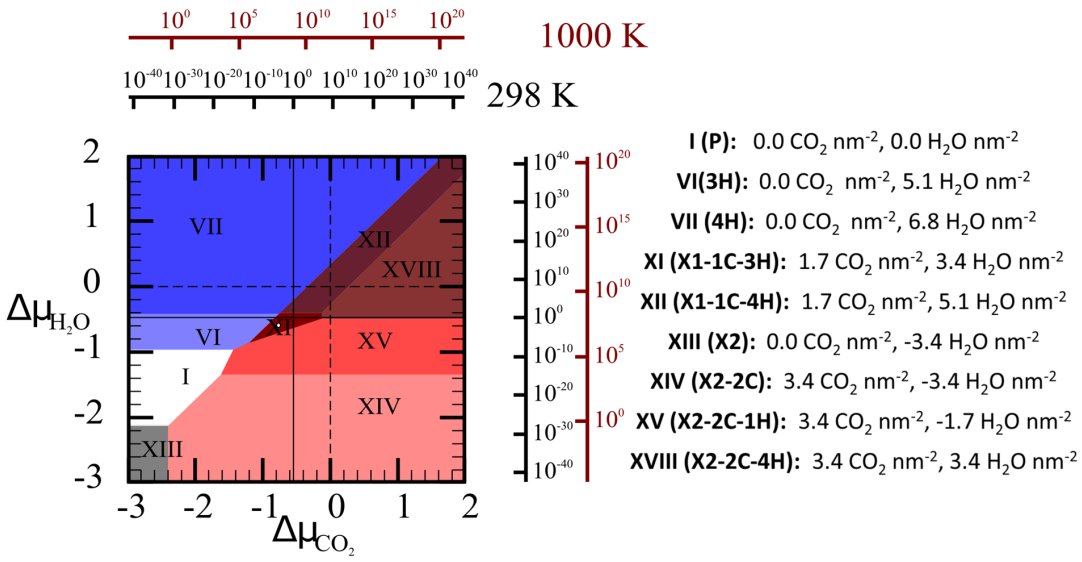

Figure 5.10: {100} ^{90}Sr surface phase diagram calculated using optB86b-vdW, where the dashed line is 1 bar pressure at 0 K and the solid line is 1 bar pressure at 298 K. White circle represents; 400 ppm CO_2 and 32 mbar of H_2O at 298 K (atmospheric conditions). Visual representations of the different surfaces can be found in Appendix B.

Table 5.5 shows the most thermodynamically stable phases under a range of conditions. At atmospheric conditions the most thermodynamically stable phases are VI (3H) for {001} and XI (X1-1C-3H) for {100}. This implies that under these conditions ^{90}Sr doped {001} and {100} will react with H_2O to form a hydrated surface. However, again the {001} shows that ambient conditions are close to a phase boundary, and hence any excess carbonate will stabilise with the adsorption further. Thus, the general result is that while ^{90}Sr adsorption, neglecting the influence of carbonate is unfavourable, once sufficient carbonate is present the adsorption is stabilised.

Table 5.5: Predicted thermodynamically most stable ^{90}Sr doped defect surface at a range of reference conditions for {001} and {100}. P is Pure, nC and nH represent the number of additional CO_2 and H_2O respectively and X is the number of H_2O molecules that have been removed. Visual representations of the different surfaces can be found in Appendix B.

Conditions	**{001}**		**{100}**	
	Surface	**Label**	**Surface**	**Label**
400 ppm CO_2, 32 mbar H_2O at 298 K	VI	3H	XI	X1-1C-3H
1 bar CO_2, 1 bar H_2O at 298 K	XVI	X2-2C-2H	XI	X1-1C-3H
1 bar CO_2, 1 bar H_2O at 0 K	XII	X1-1C-4H	XII	X1-1C-4H

5.4 Conclusions

This chapter has evaluated the surface properties of Brucite and gained valuable information on the interactions with radio-nuclei (^{90}Sr). To summarise, we have outlined a thermodynamic framework, which can be used to evaluate the interaction of H_2O/CO_2 with surfaces and there defects. Using this framework the following conclusions can be made:

- {100} surface display evidence of being more reactive than {001}.
  - Increase in the adsorption energies.
  - Related to the higher coordination number of the Mg surface ions for {100}.
- Changing the reference state of H_2O from gas to liquid can effect the stability of surface configurations.
- At atmospheric conditions the {100} surface would readily adsorb H_2O, whereas for the {001} surface the pure is more favourable.

The same framework can be applied to surfaces which have been doped with radio-nuclei. This enables the evaluation of likely radio-nuclei sites in Brucite surface, for ^{90}Sr defects the framework shows that;

- The stability of ^{90}Sr defects is heavily dependant on the coordination that the surface ions can achieve.
  - Surface reconstruction can aid in achieving higher coordination numbers.
- The larger size of the ^{90}Sr ion disrupts the mono-layer structure, decreasing the stability of the mono-layer.
  - This could potentially be overcome with the inclusion of more water layer or the rearrangement of the adsorbed molecules.
- At atmospheric conditions both ^{90}Sr doped surfaces will readily adsorb H_2O, forming a hydrated surface.
- Co-adsorption of CO_2 increases the likelihood of ^{90}Sr adsorption, hence external conditions need to be considered when modelling surfaces.

Using the same methodology and analysis of the results, it is possible to extend this study to include additional Mg-rich phases. However, due to time constraints this is an area of study in which future research can be based on. Extending to other Mg-rich surfaces would lead to an increased understanding of Magnox sludge and the interaction with radio-nuclei.

6 Conclusions & Future Work

The main conclusions for each of the chapters are summarised here along with proposed future research areas associated with each section are outlined.

6.1 Magnesium Oxides, Hydroxides and Carbonates

The first goal was to investigate the use of DFT and particularly the requirement of van der Waals (vdW) corrected DFT for modelling the structure, elasticity and stability of solid magnesium phases in the $MgO - CO_2 - H_2O$ system. The results show vdW corrections to DFT can successfully evaluate these properties. It quickly became evident that the inclusion of vdW forces offered an improvement to the structural properties over uncorrected DFT. Where all experimental lattice parameters have been reproduced within $\pm$ 5%. In addition to the lattice parameters, elastic constants have also been calculated and where possible compared to literature values. All approaches produce consistent bulk moduli, where all values are within 12 GPa of the other techniques.

To investigate the reliability of the energetics of Mg-rich phases, heats of formation were calculated and compared to experimental values for all functionals. The ability to produce accurate and reliable energies is the first step towards being able to reproduce and predict thermodynamic properties. As such it was vital to choose a method which can reliably calculate the energy of all phases. All vdW techniques improve the representation of ΔH_f compared to PBE, where optB88-vdW and optB86b-vdW give the best agreement with experimental values.

All three vdW techniques have been shown to improve the simulation compared to PBE. This shows that the inclusion of vdW is vital to obtaining accurate representations of Mg-rich phases. However, there are other functionals which also attempt to account for vdW interactions that have not been included in this work. This gives an opportunity to expand upon this research to also include more functionals (*e.g.* Tkatchenko-Scheffler method [99], MBD@rSC [100] and dDsC dispersion correction method [101]). This study could also be expanded to include other Mg-rich phases, which have not been included in this work. Phases not included range from rare mineral forms (*e.g.* Barringtonite $MgCO_3.2H_2O$ and Magnesium Hydroxide Carbonate $Mg(OH)_2CO_3$) to Mg analogues of other well known minerals (*e.g.* Monohydrocalcite $MgCO_3.H_2O$ and Mg-Ikaite $MgCO_3.6H_2O$).

6.2 Mg-Rich Mineral Phase Diagrams

In Chapter 4 the composition of Mg-rich phases have been evaluated under a range of external conditions. To accomplish this goal a thermodynamic methodology was outlined and applied to generate phase diagrams. This has enabled us to evaluate the composition of Mg-rich minerals at different temperatures (T), partial pressures of carbon dioxide (p_{CO_2}) and of water (p_{H_2O}). Identifying which phases are the most thermodynamically stable at a given p_{CO_2}, p_{H_2O}, has given valuable insight into composition of Magnox sludge. Under the time-scales in which the sludge has been stored, these thermodynamically stable phases will be prevalent.

Using the framework it was possible to produce phase diagrams for Mg-rich phases. However, it was vital to first test this methodology and ensure that the phase diagrams produced, are an accurate representation of the experimental data. This was achieved by producing phase diagrams of experimentally well defined phases. This showed that the methodology can reproduce experimental results accurately, where optB88-vdW gives the best agreement with experiment. Expanding this to include all Mg-rich phases studied, showed that Magnesite most thermodynamic stable at atmospheric conditions, as also demonstrated by the work of Chaka *et al.* [23]. All functionals produced the similar results with small consistent shifts in the phase transitions.

The major limitation of using DFT is that it ignores the vibrational contributions to the free-energy and as such does not include entropy. This was accounted for in this work by calculating the vibrational entropy of all phases and producing phase diagrams of temperature as a function of $\Delta\mu_{CO_2}$ at various $\Delta\mu_{H_2O}$. These phase diagrams reproduce the work of Langmuir *et al.* [19], although there is a constant shift in the pressures due to the different DFT techniques, this gives the possibility of applying a correction. Although since much of the experimental data is from solubility studies and the kinetics are slow, there may be issues with the precise experimental values. At ambient conditions the most thermodynamically stable phase is Magnesite, unless its inhibited in which Lansfordite/Hydromagnesite are the most stable. As temperature increases phases with less water per MgO unit are more favoured, which is to be expected.

Calculation of the vibrational entropy allows the vibrational contributions to the free-energy to be calculated. However, the vibrational frequencies are only calculated at the gamma point. Additionally this method does not take in to account the thermal expansion associated with each mineral, as we have assumed that the vibrations are purely harmonic. As such a possible future area of study is to expand the methodology to also include the quasi-harmonic approximation. This approximation introduces the explicit dependence of the phonon frequencies on the volume, allowing the calculation of thermal expansion and vibrational frequencies accurately from the gamma point. This can be implemented through the program Phonopy [102].

6.3 Surface Phase Diagrams

The next step was to explore the effect of the external conditions on adsorption. In Chapter 5, surfaces of Brcuite (one of the major phases) and its interactions with radio-nuclide ^{90}Sr were calculated. We applied the thermodynamic framework, to evaluate the interaction of H_2O/CO_2 with various surfaces. Using this framework we found that the {100} surfaces display evidence of being more reactive than {001}. This results in less favourable adsorption energies of the {001} compared to {100} and can be related to the higher coordination number of the {100} surface. The addition of H_2O to the surfaces of Brucite is favourable, however, changing the reference state of H_2O from gas to liquid can effect the stability of surface configurations. Analysis of the surface phase diagrams has shown that at atmospheric conditions the {100} surface would readily adsorb H_2O, where as, the pure {001} surface is more favourable.

The same framework can be applied to defect surfaces which have been doped with radio-nuclei. This enables the evaluation of likely radio-nuclei sites in Brucite surface. The stability of Sr defects is heavily dependant on the coordination that the surface ions can achieve. Higher coordination can be achieved through larger surface area and surface reconstruction. The larger size of the Sr-ion disrupts the mono-layer structure, decreasing the stability of the mono-layer. This can be overcome with the inclusion of more water layers or the rearrangement of the adsorbed molecules. Thus, re-establishing the complex H-bonding network of adsorbed water molecules and hence increasing the surface stability. Additionally, surfaces could be investigated using molecular dynamics to study the solvation of Brucite surfaces and the interaction with radio-nuclei. Analysis of the Sr surface phase diagram has shown that at atmospheric conditions both Sr doped surfaces will readily adsorb H_2O, forming an hydrated surface.

Using the same methodology and analysis of the results presented in Chapter 5, it is possible to extend this study to include additional Mg-rich phases. However, due to time constraints this is an area of study in which future research can be based. Extending to other Mg-rich surfaces would lead to an increased understanding of Magnox sludge and the interaction with radio-nuclei. Additionally the adsorption of different ions could be investigated. One ion of particular interest is Ca, with a high concentration of Ca-ions present in the pond, interactions of Ca with Magnox sludge is highly likely. Hence, this would provide a more complete understanding of the composition of Magnox sludge.

In summary this work has demonstrated that DFT can be used in association with a thermodynamic model to produce high quality information on the composition of Magnox sludge. However, there is still many unanswered questions regarding the exact composition of the sludge and its interactions with heavy metals. As such this will remain an interesting and active area of research in the years to come.

References

[1] L. A. Hollingbery and T. R. Hull. The Thermal Decomposition of Huntite and Hydromagnesite-A review. *Thermochimica Acta*, 509(1-2):1–11, 2010.

[2] P. De Silva, L. Bucea, and V. Sirivivatnanon. Chemical, Microstructural and Strength Development of Calcium and Magnesium Carbonate Binders. *Cement and Concrete Research*, 39(5):460–465, 2009.

[3] E. Makkos, A. Kerridge, J. Austin, and N. Kaltsoyannis. Ionic Adsorption on the Brucite (0001) Surface: A Periodic Electrostatic Embedded Cluster Method Study. *Journal of Chemical Physics*, 145(20), 2016.

[4] S. Owens, M. Higgins-Bos, M. Bankhead, and J. Austin. Using Chemical and Process Modelling to Design, Understand and Improve an Effluent Treatment Plant., 2015.

[5] World Nuclear Association. Nuclear Development in the United Kingdom, 2016. http://www.world-nuclear.org/information-library/country-profiles/countries-t-z/appendices/nuclear-development-in-the-united-kingdom.aspx, Accessed on 03/06/2017.

[6] The Institution of Electrical Engineers. Nuclear Reactor Types. 2005.

[7] K. R. Hallam, P. C. Minshall, P. J. Heard, and P. E.J. Flewitt. Corrosion of the Alloys Magnox AL80, Magnox {ZR55} and Pure Magnesium in Air Containing Water Vapour. *Corrosion Science*, 112:347–363, 2016.

[8] World Nuclear Association. Nuclear Development in the United Kingdom, 2017. http://www.world-nuclear.org/information-library/current-and-future-generation/outline-history-of-nuclear-energy.aspx, Accessed on 03/06/2017.

[9] World Nuclear Association. Nuclear Development in the United Kingdom, 2017. http://www.world-nuclear.org/information-library/nuclear-fuel-cycle/introduction/nuclear-fuel-cycle-overview.aspx, Accessed on 03/06/2017.

[10] S Barlow. Budge the Sludge. *Nuclear Engineering International*, 49(601): 10–13, 2004.

[11] Sellafield Ltd. Sellafield Integrated Waste Strategy Version 2 Report and Recommendations. 2007. GEN-1880A.

[12] S. Topping and S. Bruce. A Ponderous Hazard. *Nuclear Engineering International*, 51(625):28–32, 2006.

[13] J. J. Hastings, D. Rhodes, A. S. Fellerman, D. McKendrick, and C. Dixon. New approaches for sludge management in the nuclear industry. *Powder Technology*, 174(1-2):18–24, 2007.

[14] Sellafield Ltd. Sellafield Integrated Waste Strategy - 2009 Report. 2009.

[15] S. F. Jackson, S. D. Monk, and Z. Riaz. An Investigation Towards Real Time Dose Rate Monitoring, and Fuel Rod Detection in a First Generation Magnox Storage Pond (FGMSP). *Applied Radiation and Isotopes*, 94:254–259, 2014.

[16] S. A. Parry, F. R. Livens, and L. O'Brien. Corroded Magnox Sludge and Plutonium Waste Cementation. *Geochimica Et Cosmochimica Acta*, 71(15), 2007.

[17] C. R. Gregson, D. T. Goddard, M. J. Sarsfield, and R. J. Taylor. Combined Electron Microscopy and Vibrational Spectroscopy Study of Corroded Magnox sludge from a Legacy Spent Nuclear Fuel Storage Pond . *Journal of Nuclear Materials*, 412(1):145–156, 2011.

[18] D. R. Blackburn, E. J. Thompson, and Asme. The Manufacture and use of Sludge Test Materials for R&D Purpose in the Treatment and Processing of Magnox Based Sludge. *Asme 2013 15th International Conference on Environmental Remediation and Radioactive Waste Management.*

[19] D Langmuir. Stability of Carbonates in the System MgO-CO_2-H_2O. *The Journal of Geology*, 73(5):730–754, 1965.

[20] J. Schott and J. L. Dandurand. Stability of Natural Carbonates: Re-Evaluation of Free-Energy Data in Systems MgO-CO_2-H_2O and CaO-MgO-CO_2-H_2O. *Cr. Acad. Sci. C: Chim.*, 280(20):1247, 1975.

[21] K. Sandengen, L. O. Josang, and B. Kaasa. Simple method for synthesis of magnesite ($MgCO_3$). *Industrial & Engineering Chemistry Research*, 47(4): 1002–1004, 2008.

[22] R. J. Hill, J. H. Canterford, and F. J. Moyle. New Data for Lansfordite. *Mineralogical Magazine*, 46(341):453–457, 1982.

[23] A. M. Chaka and A. R. Felmy. Ab Initio Thermodynamic Model for Magnesium Carbonates and Hydrates. *Journal of Physical Chemistry A*, 118: 7469–7488, 2014.

[24] T. Woods and R. Garrels. *Thermodynamic Values at Low Temperature for Natural Inorganic Materials: An Uncritical Summary.* Oxford University Press: New York, New York, 1987.

[25] E. Königsberger, L. Königsberger, and H. Gamsjäger. Low-Temperature Thermodynamic Model for the System Na_2CO_3-$MgCO_3$-$CaCO_3$-H_2O. *Geochimica et Cosmochimica Acta*, 63(19-20):3105–3119, 1999.

[26] A. De Visscher, J. Vanderdeelen, E. Königsberger, B. R Churagulov, M. Ichikuni, and M. Tsurumi. IUPAC-NIST Solubility Data Series. 95. Alkaline Earth Carbonates in Aqueous Systems. *Journal of Physical and Chemical Reference Data*, 41(1):013105–013105, 2012.

[27] M Haenchen, V Prigiobbe, R Baciocchi, and M Mazzotti. Precipitation in the Mg-Carbonate System - Effects of Temperature and CO_2 Pressure. *Chemical Engineering Science*, 63(4):1012–1028, 2008.

[28] K. S. Lackner, C. H. Wendt, D. P. Butt, E. L. Joyce, and D. H. Sharp. Carbon Dioxide Disposal in Carbonate Minerals. *Energy*, 20(11):1153 – 1170, 1995.

[29] A. A. Olajire. A Review of Mineral Carbonation Technology in Sequestration of $\{CO_2\}$. *Journal of Petroleum Science and Engineering*, 109:364 – 392, 2013.

[30] R. Zevenhoven, S. Teir, and S. Eloneva. Heat Optimisation of a Staged Gas-Solid Mineral Carbonation Process for Long-Term $\{CO_2\}$ Storage. *Energy*, 33 (2):362–370, 2008.

[31] H.T. Schaef, C.F. Windisch, B.P. McGrail, P.F. Martin, and K.M. Rosso. Brucite $[Mg(OH)_2]$ Carbonation in Wet Supercritical CO_2: An in situ High Pressure X-Ray Diffraction Study. *Geochimica et Cosmochimica Acta*, 75(23): 7458–7471, 2011.

[32] S. Teir, R. Kuusik, C. J. Fogelholm, and R. Zevenhoven. Production of Magnesium Carbonates from Serpentinite for Long-Term Storage of $\{CO_2\}$. *International Journal of Mineral Processing*, 85(1-3):1–15, 2007.

[33] Fixation of Carbon Dioxide by Producing Hydromagnesite from Serpentinite. *Applied Energy*, 86(2):214 – 218, 2009.

[34] K. S. Lackner. Carbonate Chemistry for Sequestering Fossil Carbon. *Annual Review of Energy and the Environment*, 27:193–232, 2002.

[35] V. E. Barnes, D. A. Shock, and W. A. Cunningham. Utilization of Texas serpentine. *University of Texas Publications.*, pages 5020–5052, 1950.

[36] C. H. Wendt, D. P. Butt, K. S. Lackner, R. U. Vaidya, and H. J. Ziock. *Thermodynamic Calculations for Acid Decomposition of Serpentine and Olivine in MgCl Melts, 3: Heat Consumption in Process Design.* Los Alamos National Laboratory ; November 25, 1998., 1998.

[37] G.B. Harris and J.G. Peacey. Production of Magnesium Metal from Magnesium Containing Materials, 1990. CA Patent 1,277,144.

[38] US DOE. Title 40 CFR Part 191 Compliance Certification Application for the Waste Isolation Pilot Plant, 1996. 21 vols. DOE/CAO 1996-2184.

[39] Y. Xiong and A. S. Lord. Experimental Investigations of the Reaction Path in the MgO-CO_2-H_2O System in Solutions with Various Ionic Strengths, and their Applications to Nuclear Waste Isolation. *Applied Geochemistry*, 23(6): 1634–1659, 2008.

[40] L. H. Thomas. The Calculation of Atomic Fields. *Mathematical Proceedings of the Cambridge Philosophical Society*, 23(5):542–548, 1927.

[41] E. Fermi. Eine statistische Methode zur Bestimmung einiger Eigenschaften des Atoms und ihre Anwendung auf die Theorie des Periodischen Systems der Elemente. *Zeitschrift für Physik*, 48(1):73–79, 1928.

[42] P. Hohenberg and W. Kohn. Inhomogeneous Electron Gas. *Physical Review*, 136:B864–B871, 1964.

[43] J. P. Perdew, J. A. Chevary, S. H. Vosko, K. A. Jackson, M. R. Pederson, D. J. Singh, and C. Fiolhais. Atoms, Molecules, Solids, and Surfaces - Applications of the Generalized Gradient Approximation for Exchange and Correlation. *Physical Review B*, 46(11):6671–6687, 1992.

[44] J. P. Perdew, K. Burke, and M. Ernzerhof. Generalized Gradient Approximation made Simple. *Physical Review Letters*, 77(18):3865–3868, 1996.

[45] S. Grimme, J. Antony, S. Ehrlich, and H. Krieg. A Consistent and Accurate Ab Initio Parametrization of Density Functional Dispersion Correction (DFT-D) for the 94 Elements H-Pu. *The Journal of Chemical Physics*, 132(15): 154104, 2010.

[46] M. Dion, H. Rydberg, E. Schroder, D. C. Langreth, and B. I. Lundqvist. Van der Waals density functional for general geometries. *Physical Review Letters*, 92(24), 2004.

[47] G. Kresse and J. Furthmüller. Efficiency of Ab-Initio Total Energy Calculations for Metals and Semiconductors using a Plane-Wave Basis Set. *Computational Materials Science*, 6(1):15–50, 1996.

[48] G. Román-Pérez and José M. S. Efficient Implementation of a van der Waals Density Functional: Application to Double-Wall Carbon Nanotubes. *Physical Review Letters*, 103:096102, 2009.

[49] J. Klimes, D. R. Bowler, and A. Michaelides. Chemical Accuracy for the van der Waals Density Functional. *Journal of Physics-Condensed Matter*, 22(2), 2010.

[50] J. Klimes, D. R. Bowler, and A. Michaelides. Van der Waals Density Functionals Applied to Solids. *Physical Review B*, 83:195131, 2011.

[51] A. D. Becke. On the Large-Gradient Behaviour of the Density Functional Exchange Energy. *Journal of Chemical Physics*, 85(12):7184–7187, 1986.

[52] A. D. Becke. Density-Functional Exchange-Energy Approximation with Correct Asymptotic Behaviour. *Physical Review A*, 38:3098–3100, 1988.

[53] M. C. Payne, M. P. Teter, D. C. Allan, T. A. Arias, and J. D. Joannopoulos. Iterative minimization techniques for ab initio total-energy calculations: molecular dynamics and conjugate gradients. *Rev. Mod. Phys.*, 64: 1045–1097, Oct 1992. doi: 10.1103/RevModPhys.64.1045. URL `https://link.aps.org/doi/10.1103/RevModPhys.64.1045`.

[54] P. E. Blöchl. Projector Augmented-Wave Method. *Physical Review B*, 50: 17953–17979.

[55] R. Fletcher and M. J. D. Powell. A Rapidly Convergent Descent Method for Minimization. *The Computer Journal*, 6(2):163, 1963.

[56] C. G. Broyden. Convergence of Single-Rank Quasi-Newton Methods. *Mathematics of Computation*, 24(110):365, 1970.

[57] R. Fletcher. A New Approach to Variable Metric Algorithms. *The Computer Journal*, 13(3):317, 1970.

[58] D. Goldfarb. A Family of Variable-Metric Methods Derived by Variation Means. *Mathematics of Computation*, 24(109):23, 1970.

[59] D. F. Shanno. Conditioning of Quasi-Newton Methods for Function Minimization. *Mathematics of Computation*, 24(111):647, 1970.

[60] P. Pulay. Convergence Acceleration of Iterative Sequences. the Case of Scf Iteration. *Chemical Physics Letters*, 73(2):393–398, 1980.

[61] D. A. Andersson, G. Baldinozzi, L. Desgranges, D. R. Conradson, and S. D. Conradson. Density functional theory calculations of uo2 oxidation: Evolution of uo2+x, u4o9â€“y, u3o7, and u3o8. *Inorganic Chemistry*, 52(5):2769–2778, 2013.

[62] J. M. Flitcroft, M. Molinari, N. A. Brincat, M. T. Storr, and S. C. Parker. Hydride ion formation in stoichiometric uo2. *Chem. Commun.*, 51:16209–16212, 2015.

[63] M. Nolan, S. Parker, and G. Watson. Vibrational properties of co on ceria surfaces. 600:175–178, 07 2006.

[64] D. J. Cooke. Surface structure of (100) and (110) surfaces of zno with density functional theory and atomistic simulation. *The Journal of Physical Chemistry B*, 110(15):7985–7991, 2006.

[65] S. Sasaki, K. Fujino, and Y. Takeuchi. X-Ray Determination of Electron-Density Distributions in Oxides, MgO, MnO, CoO, and NiO, and Atomic Scattering Factors of their Constituent Atoms. *Proceedings of the Japan Academy, Series B*, 55(2):43–48, 1979.

[66] A. E. Ringwood. *Composition and Petrology of the Earth's Mantle*. 1975.

[67] S. Iwai K. D. Oh, H. Morikawa and H. Aoki. The Crystal Structure of Magnesite. *American Mineralogist*, 58(11):480–494, 1973.

[68] M. Catti, G. Ferraris, S. Hull, and A. Pavese. Static Compression and H Disorder in Brucite, $Mg(OH)_2$, to 11 GPa: a Powder Neutron Diffraction Study. *Physics and Chemistry of Minerals*, 22(3):200–206, 1995.

[69] W. R. Busing and H. A. Levy. Neutron Diffraction Study of Calcium Hydroxide. *Journal of Chemical Physics*, 26(3):563–568, 1957.

[70] P. D'Arco, M Causà, C Roetti, and B Silvi. Periodic Hartree-Fock study of a weakly bonded layer structure: Brucite $Mg(OH)_2$. *Physical Review B*, 47: 3522–3529, 1993.

[71] M.B Kruger, Q Williams, and R Jeanloz. Vibrational-Spectra of $Mg(OH)_2$ and $Ca(OH)_2$ Under Pressure. *Journal of Chemical Physics*, 91(10):5910–5915, 1989.

[72] M. Akao and S. Iwai. The Hydrogen Bonding of Hydromagnesite. *Acta Crystallographica Section B*, 33(4):1273–1275, 1977.

[73] M. Akao, F. Marumo, and S. Iwai. The Crystal Structure of Hydromagnesite. *Acta Crystallographica Section B*, 30, 1974.

[74] D. Bhattacharjya, T. Selvamani, and I. Mukhopadhyay. Thermal Decomposition of Hydromagnesite. *Journal of Thermal Analysis and Calorimetry*, 107 (2):439–445, 2012.

[75] V. Vágvölgyi, R. L. Frost, M. Hales, A. Locke, J. Kristóf, and E. Horváth. Controlled Rate Thermal Analysis of Hydromagnesite. *Journal of Thermal Analysis and Calorimetry*, 92(3):893–897, 2008.

[76] G. Giester, C. L. Lengauer, and B. Rieck. The crystal structure of nesquehonite, $MgCO_3.3H_2O$, from Lavrion, Greece. *Mineralogy and Petrology*, 70(3): 153–163, 2000.

[77] B. N. Liu, X. T. Zhou, X. S. Cui, and J. G. Tang. Synthesis of Lansfordite $MgCO_3.5H_2O$ and its Crystal Structure Investigation. *Science in China*, B33: 1350–1356, 1990.

[78] K. Burke. *The ABC of DFT*. University of California, Department of Chemistry, University of California, 2007.

[79] N. A. Brincat, S. C. Parker, M. Molinari, G. C. Allen, and M. T. Storr. Ab Initio Investigation of the UO_3 Polymorphs: Structural Properties and Thermodynamic Stability. *Inorganic Chemistry*, 53(23):12253–12264, 2014.

[80] N. A. Brincat, S. C. Parker, M. Molinari, G. C. Allen, and M. T. Storr. Density Functional Theory Investigation of the Layered Uranium Oxides U_3O_8 and U_2O_5. *Dalton Transactions*, 44:2613–2622, 2015.

[81] D. G. Isaak, O. L. Anderson, and T Goto. Measured Elastic Moduli of Single-Crystal MgO up to 1800 K. *Physics and Chemistry of Minerals*, 16(7):704–713, 1989.

[82] B. B. Karki, L Stixrude, S. J. Clark, M. C. Warren, G. J. Ackland, and J Crain. Structure and elasticity of MgO at high pressure. *American Mineralogist*, 82 (1-2):51–60, 1997.

[83] M. M. P. HUMBERT and F. PLICQUE. Propriétés Elastiques de Carbonates Rhomboédriques Monocristallins : Calcite, Magnésite, Dolomie. *G. R. Acad. Se. Paris Série B*, 275:391, 1972.

[84] M. G. Brik. First-Principles Calculations of Structural, Electronic, Optical and Elastic Properties of Magnesite $MgCO_3$ and Calcite $CaCO_3$. *Physica B: Condensed Matter*, 406(4):1004 – 1012, 2011.

[85] M. Catti, A. Pavese, R. Dovesi, and V. R. Saunders. Static Lattice and Electron Properties of $MgCO_3$ (Magnesite) Calculated by Ab Initio Periodic Hartree-Fock Methods. *Physical Review B*, 47:9189–9198, 1993.

[86] Z. J. Liu, X. W. Sun, T. Song, Y. Guo, C. R. Zhang, and Z. R. Zhang. Atomistic Simulation of the Structural and Elastic Properties of Magnesite. *Bulletin of Materials Science*, 39(5):1319–1325, 2016.

[87] F Jiang, S Speziale, and T. S. Duffy. Single-Crystal Elasticity of Brucite, $Mg(OH)_2$, to 15 GPa by Brillouin Scattering. 91(11-12):1893–1900, 2006.

[88] X. Xia, D. J. Weidner, and H. Zhao. Equation of State of Brucite: Single-Crystal Brillouin Spectroscopy Study and Polycrystalline Pressure-Volume-Temperature Measurement. *American Mineralogist*, 83(1-2):68–74, 1998.

[89] P. T. Jochym, A. M. Oleś, K. Parlinski, J. Łażewski, P. Piekarz, and M. Sternik. Structure and Elastic Properties of $Mg(OH)_2$ from Density Functional Theory. *Journal of Physics: Condensed Matter*, 22(44):445403, 2010.

[90] M. W. Chase, National Institute of Standards, and Technology (U.S.). *NIST-JANAF Thermochemical Tables*. Journal of physical and chemical reference data Monograph. American Chemical Society ; American Institute of Physics for the National Institute of Standards and Technology, Washington, D.C. Woodbury, N.Y., 4th edition, 1998.

[91] G. A. Jeffrey. *An Introduction to Hydrogen Bonding*. Oxford University Press, Oxford, 1997.

[92] W. Ostwald. Studies on the Formation and Transformation of Solid Bodies. *Journal of Physical Chemistry*, 22:289–330, 1897.

[93] T. Threlfall. Structural and Thermodynamic Explanations of Ostwald's Rule. *Organic Process Research & Development*, 7(6):1017–1027, 2003.

[94] Stephen A. Parry, Luke O'Brien, Andy S. Fellerman, Christopher J. Eaves, Neil B. Milestone, Nicholas D. Bryan, and Francis R. Livens. Plutonium behaviour in nuclear fuel storage pond effluents. *Energy Environmental Sciences*, 4:1457–1464, 2011.

[95] F. Bertaut. Le Terme Electrostatique de L'Energie de Surface. *Compte Rendus Hebdomadaire des Séances de l'Académie des Sciences*, 246:3447–3450, 1958.

[96] P. W. Tasker. The Stability of Ionic Crystal Surfaces. *Journal of Physics C Solid State Physics*, 12:4977–4984, 1979.

[97] G. W. Watson, E. T. Kelsey, N. H. de Leeuw, D. J. Harris, and S. C. Parker. Atomistic Simulation of Dislocations, Surfaces and Interfaces in MgO. *Journal of Chemical Society, Faraday Transactions*, 92:433–438, 1996.

[98] J.P. Allen, A. Marmier, and S.C. Parker. Atomistic Simulation of Surface Selectivity on Carbonate Formation at Calcium and Magnesium Oxide Surfaces. *Journal of Physical Chemistry C*, 116(24):13240–13251, 2012.

[99] A. Tkatchenko and M. Scheffler. Accurate Molecular van der Waals Interactions from Ground-State Electron Density and Free-Atom Reference Data. *Physical Review Letters*, 102:073005, 2009.

[100] T. Bučko, S. Lebègue, T. Gould, and J. G. Ángyán. Many-Body Dispersion Corrections for Periodic Systems: an Efficient Reciprocal Space Implementation. *Journal of Physics: Condensed Matter*, 28(4):045201, 2016.

[101] S. N. Steinmann and C. Corminboeuf. A Generalized-Gradient Approximation Exchange Hole Model for Dispersion Coefficients. *The Journal of Chemical Physics*, 134(4):044117, 2011.

[102] A Togo and I Tanaka. First Principles Phonon Calculations in Materials Science. *S. Materialia*, 108:1–5, 2015.

A Phase Diagrams

A.1 Predicted Free Energy Phase Diagrams as a Function of Temperature

A.1.1 1 bar p_{CO_2} and 1 bar p_{H_2O}

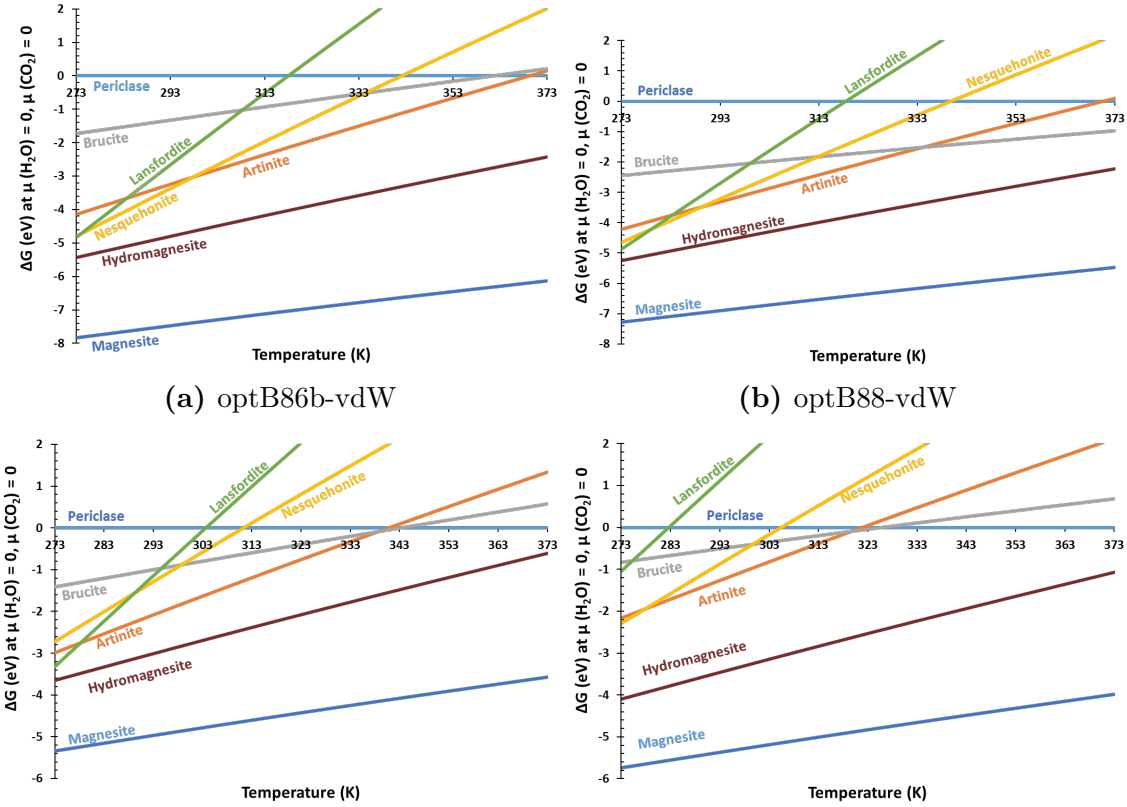

(a) optB86b-vdW **(b)** optB88-vdW

(c) PBE-D3 **(d)** PBE

Figure A.1: ΔG^0 as a function of T Phase Diagram at 1 bar p_{CO_2} and 1 bar p_{H_2O}.

A.1.2 Low p_{CO_2} and 1 bar p_{H_2O}

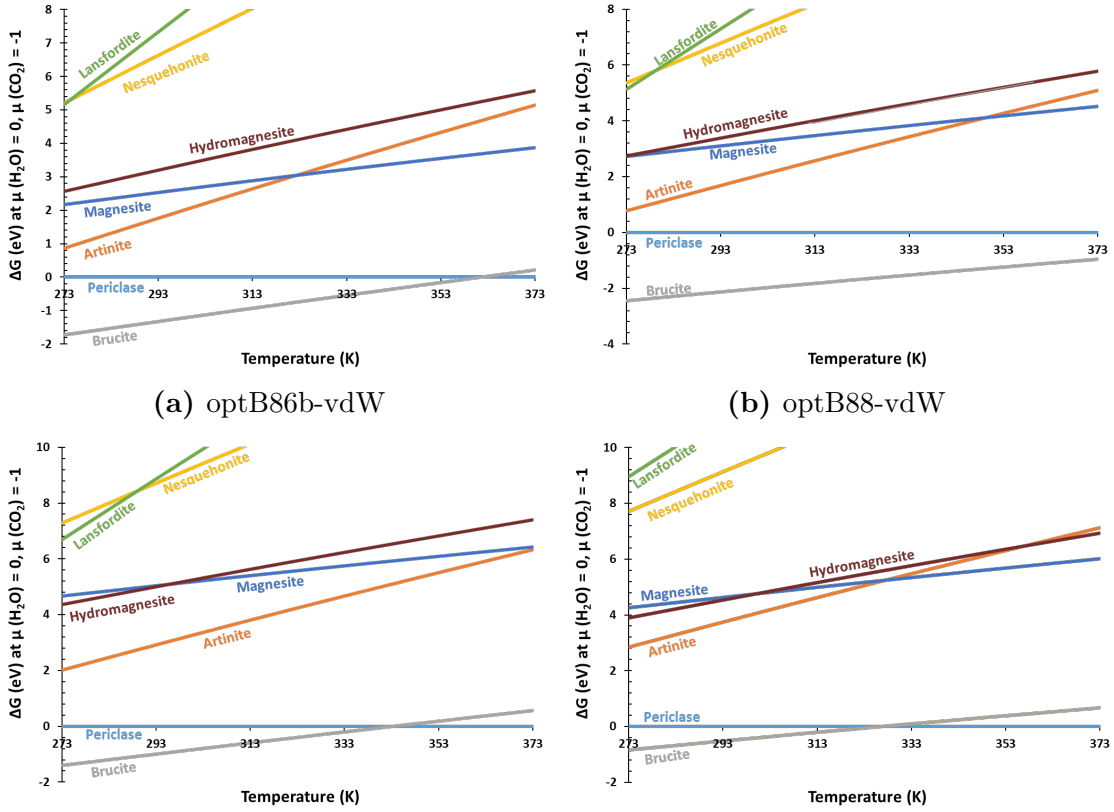

(a) optB86b-vdW **(b)** optB88-vdW

(c) PBE-D3 **(d)** PBE

Figure A.2: ΔG^0 as a function of T Phase Diagram at $\Delta\mu_{CO_2} = -1$ eV and $\Delta\mu_{H_2O} = 0$ eV.

A.1.3 High p_{CO_2} and 1 bar p_{H_2O}

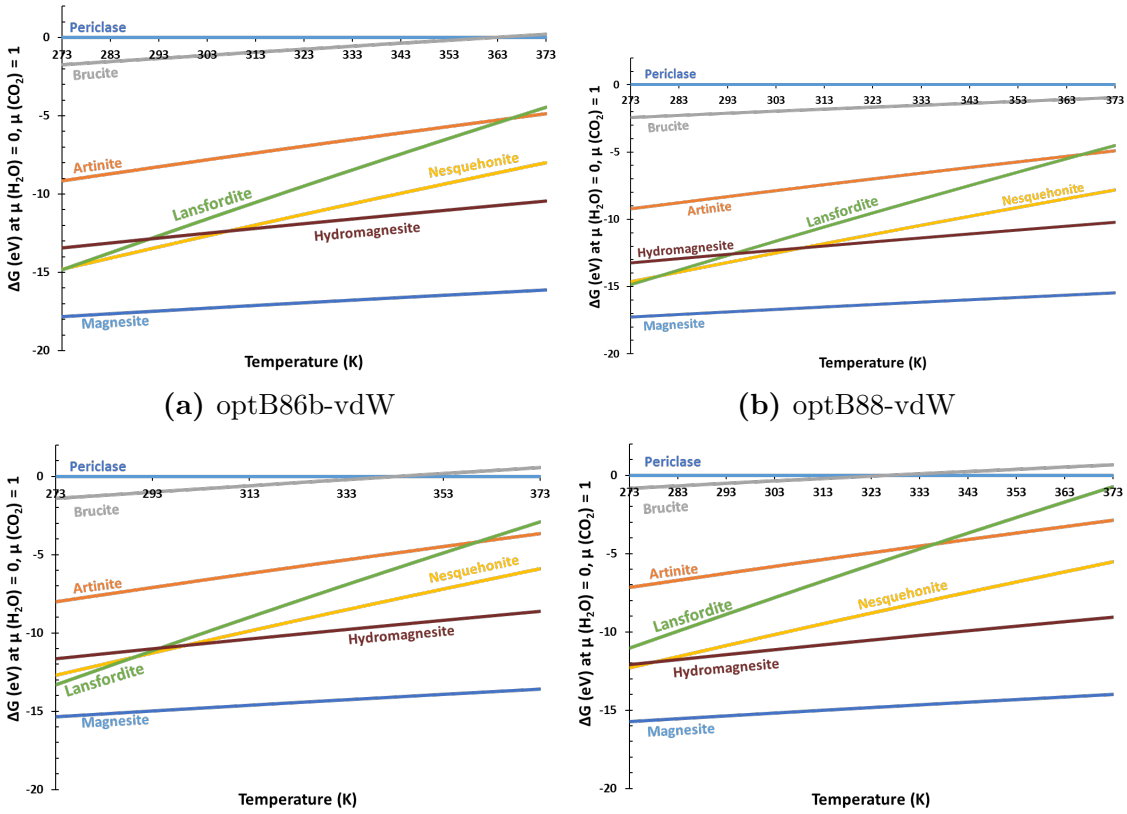

(a) optB86b-vdW **(b)** optB88-vdW

(c) PBE-D3 **(d)** PBE

Figure A.3: ΔG^0 as a function of T phase diagram at $\Delta\mu_{CO_2} = 1$ eV and $\Delta\mu_{H_2O} = 0$ eV.

A.2 Mg-Rich Mineral Phase Diagram: Temperature as a function of $\Delta\mu_{CO_2}$ at $\Delta\mu_{H_2O} = 0$ eV

A.2.1 Thermodynamic phase diagram: All Mg-rich phases

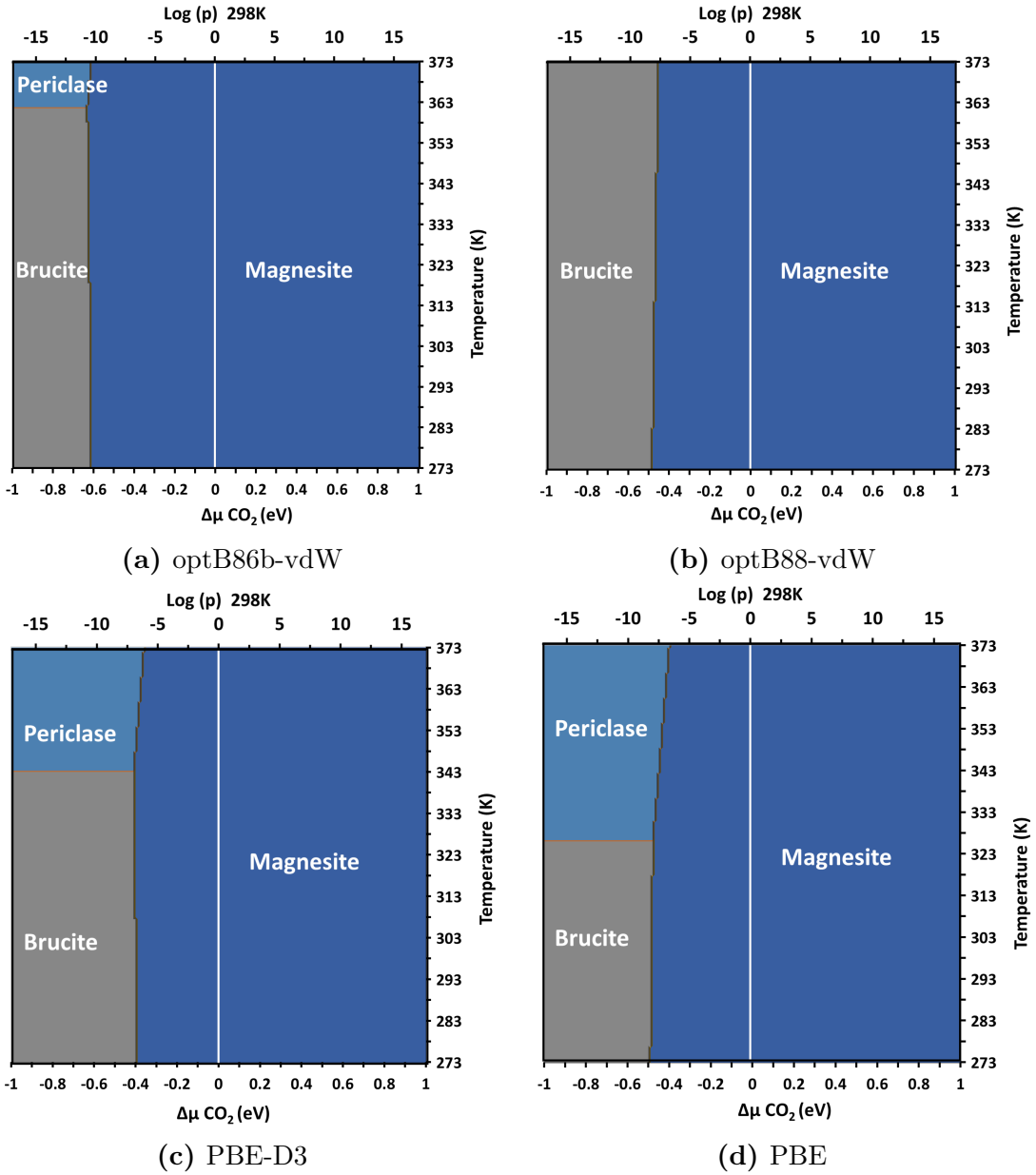

(a) optB86b-vdW

(b) optB88-vdW

(c) PBE-D3

(d) PBE

Figure A.4: Mg-rich phase diagram of $\Delta\mu_{CO_2}$ as a function of temperature at $\Delta\mu_{H_2O} = 0$ eV: Periclase, Magnesite, Brucite, Hydromagnesite, Artinite, Nesquehonite and Lansfordite a) optB86b-vdW b) optB88-vdW c) PBE-D3 d) PBE. Solid white line represents 1 bar pressure at 298 K.

A.2.2 Metastable phase diagram: with Magnesite inhibited

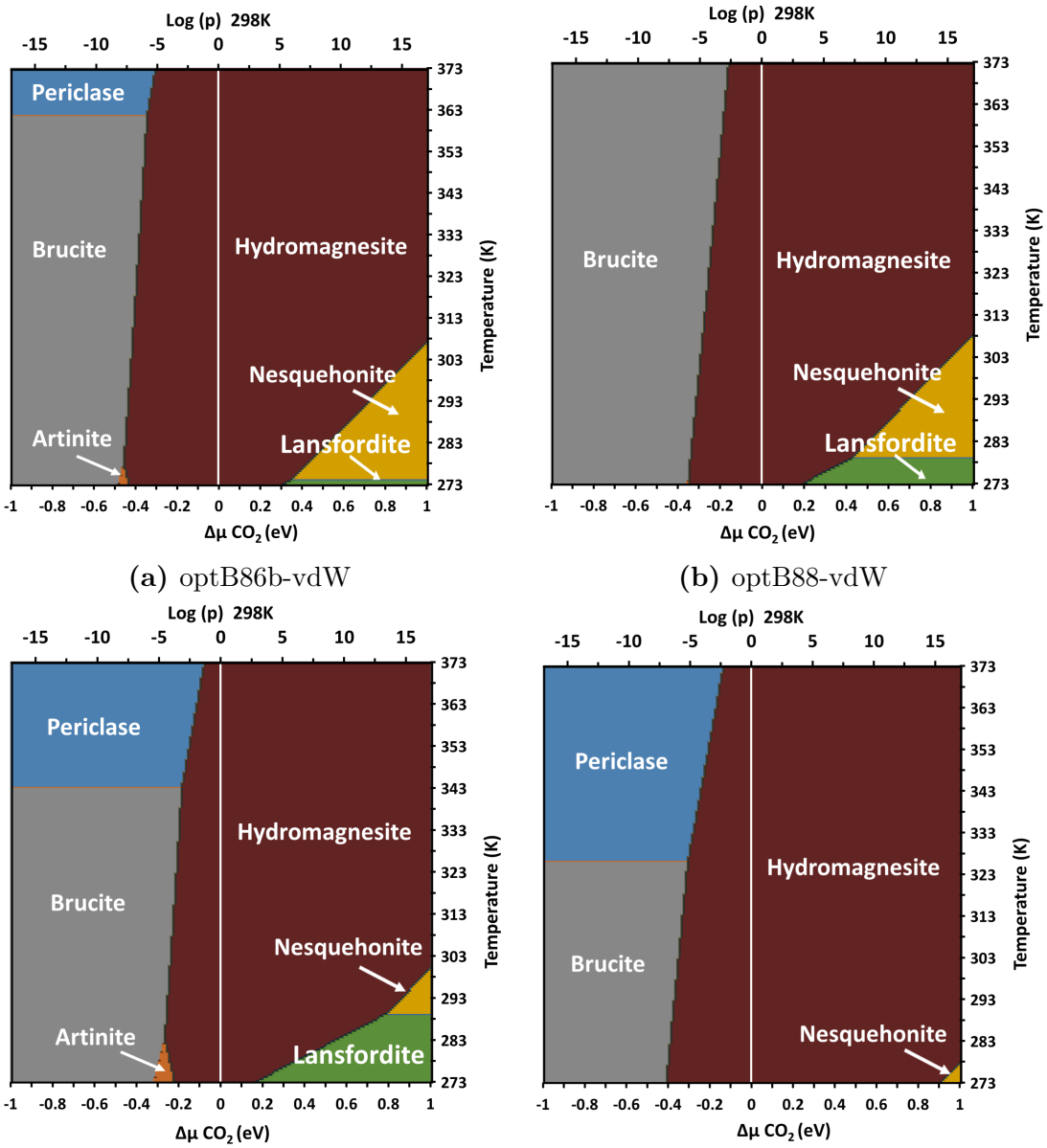

(a) optB86b-vdW

(b) optB88-vdW

(c) PBE-D3

(d) PBE

Figure A.5: Meta-stable phase diagram of $\Delta\mu_{CO_2}$ as a function of temperature at $\Delta\mu_{H_2O} = 0$ eV: Periclase, Magnesite, Brucite, Hydromagnesite, Artinite, Nesquehonite and Lansfordite a) optB86b-vdW b) optB88-vdW c) PBE-D3 d) PBE. Solid white line represents 1 bar pressure at 298 K.

B Surfaces

B.1 {001} Surface

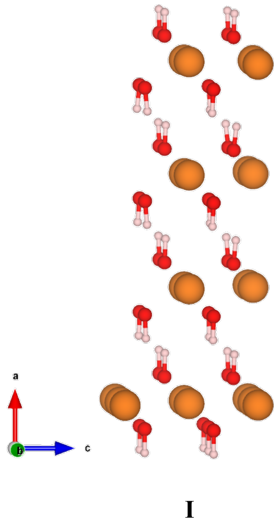

Figure B.1: Brucite {001} Surface (P): Mg in orange, H in white and O in red.

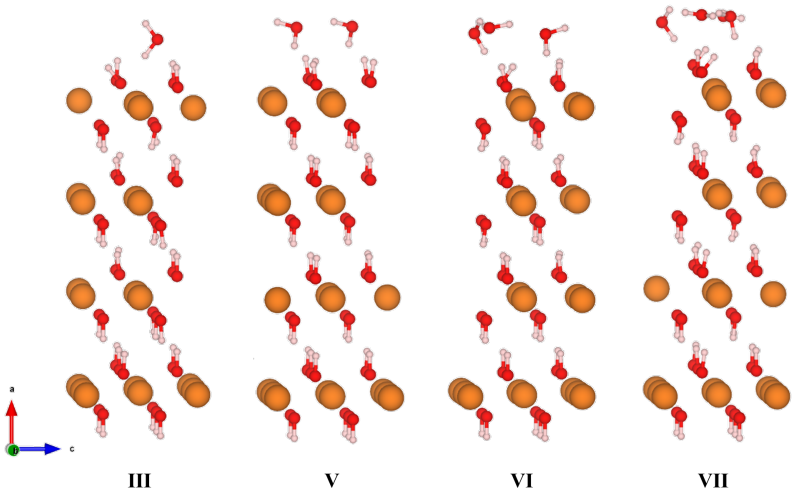

Figure B.2: Brucite {001} Surface including H_2O: III) 1H, V) 2H, VI) 3H and VII) 4H. Mg in orange, H in white and O in red.

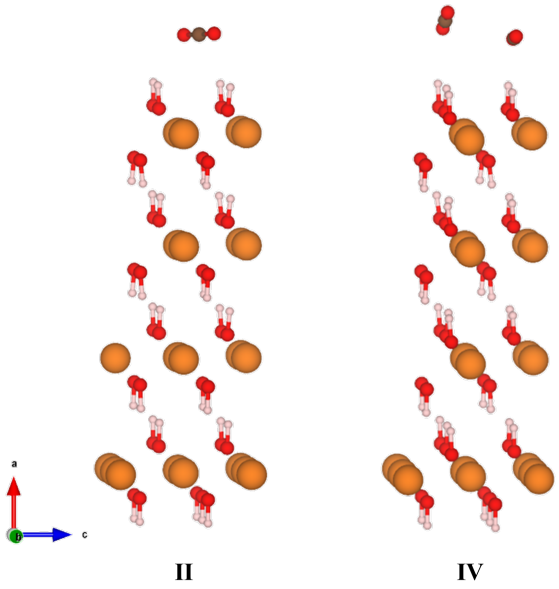

Figure B.3: Brucite {001} Surface including CO_2: II) 1C and IV) 2C. Mg in orange, C in grey, H in white and O in red.

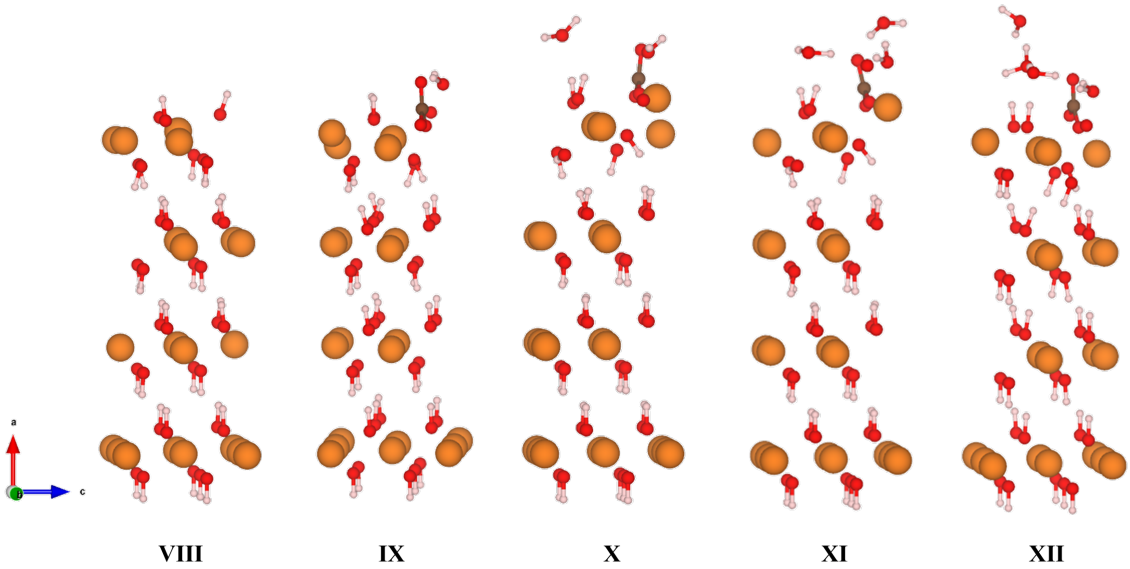

Figure B.4: {001} X1 surface including varying H_2O with 1 CO_2: VIII) X1, IX) X1-1C-1H, X) X1-1C-2H, XI) X1-1C-3H and XII) X1-1C-4H. Mg in orange, C in grey, H in white and O in red.

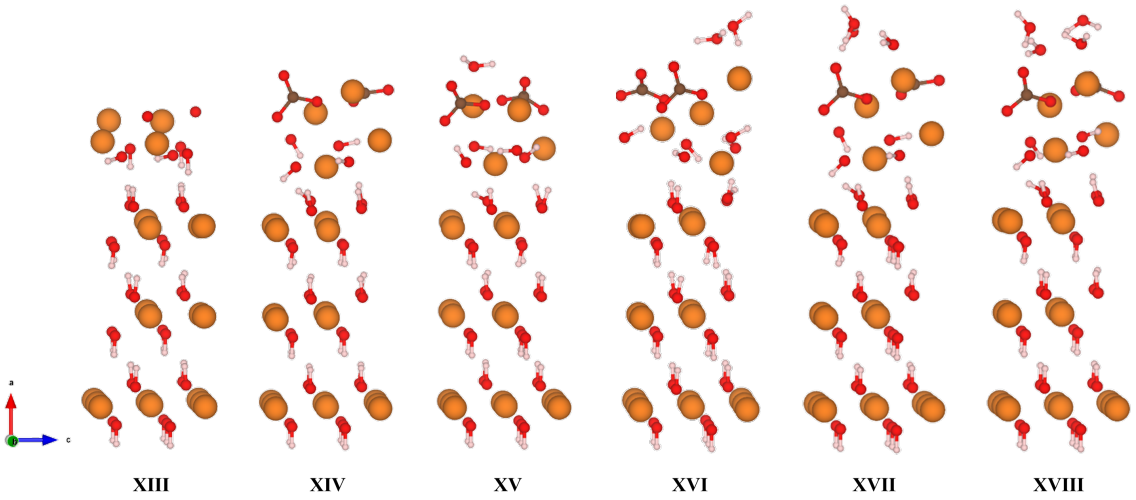

Figure B.5: {001} X2 surface including varying H_2O with 2 CO_2: XIII) X2, XIV) X2-2C, XV) X2-2C-1H, XVI) X2-2C-2H , XVII) X2-2C-3H and XVIII) X2-2C-4H. Mg in orange, C in grey, H in white and O in red.

B.2 {100} Surface

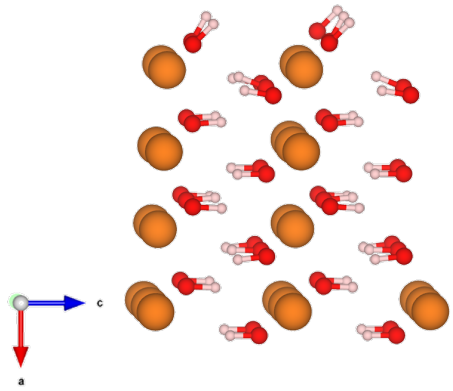

I

Figure B.6: {001} Surface (P): Mg in orange, H in white and O in red.

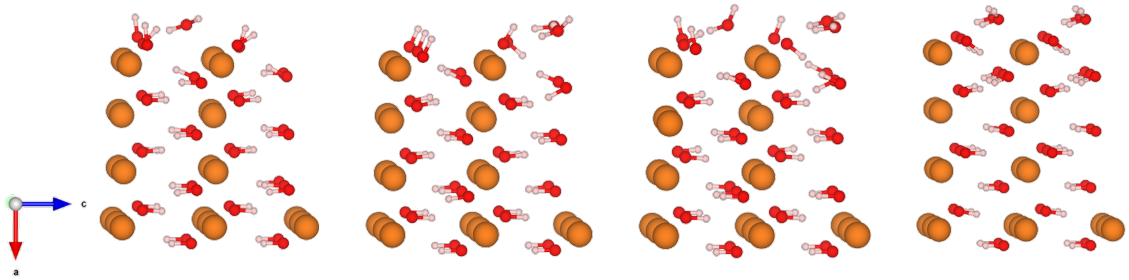

III V VI VII

Figure B.7: {100} Surface doped with H_2O: III) 1H, V) 2H, VI) 3H and VII) 4H. Mg in orange, H in white and O in red.

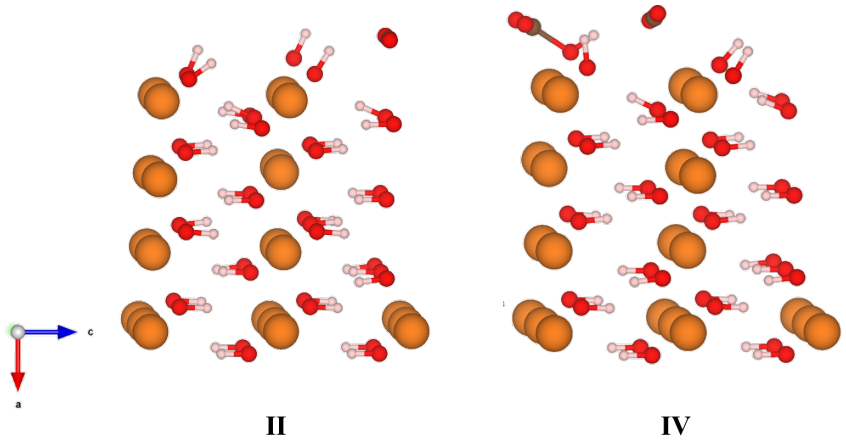

Figure B.8: {100} Surface doped with CO_2: II) 1C and IV) 2C. Mg in orange, C in grey, H in white and O in red.

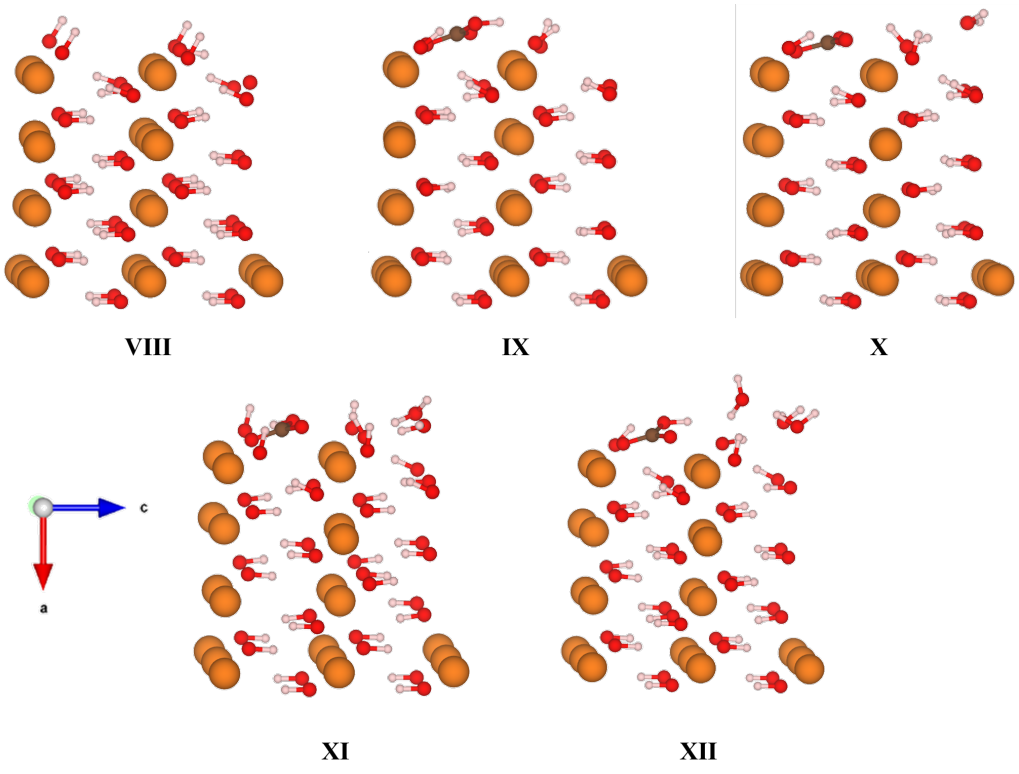

Figure B.9: {001} X1 surface with varying H_2O with 1 CO_2: VIII) X1, IX) X1-1C-1H, X) X1-1C-2H, XI) X1-1C-3H and XII) X1-1C-4H. Mg in orange, C in grey, H in white and O in red.

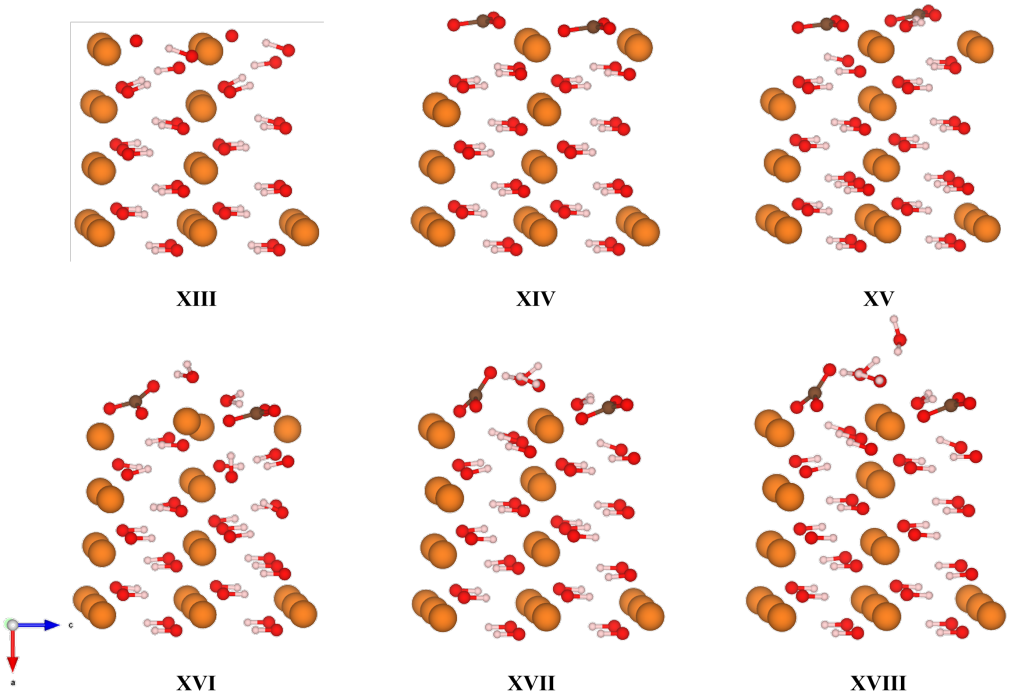

Figure B.10: {100} X2 surface including varying H_2O with 2 CO_2: XIII) X2, XIV) X2-2C, XV) X2-2C-1H, XVI) X2-2C-2H , XVII) X2-2C-3H and XVIII) X2-2C-4H. Mg in orange, C in grey, H in white and O in red.

B.3 {001} Surface Strontium Defect

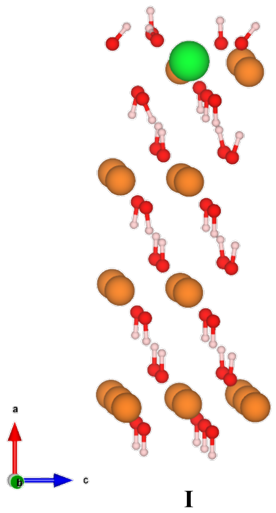

Figure B.11: {001} Surface (P): Mg in orange, Sr in green, H in white and O in red.

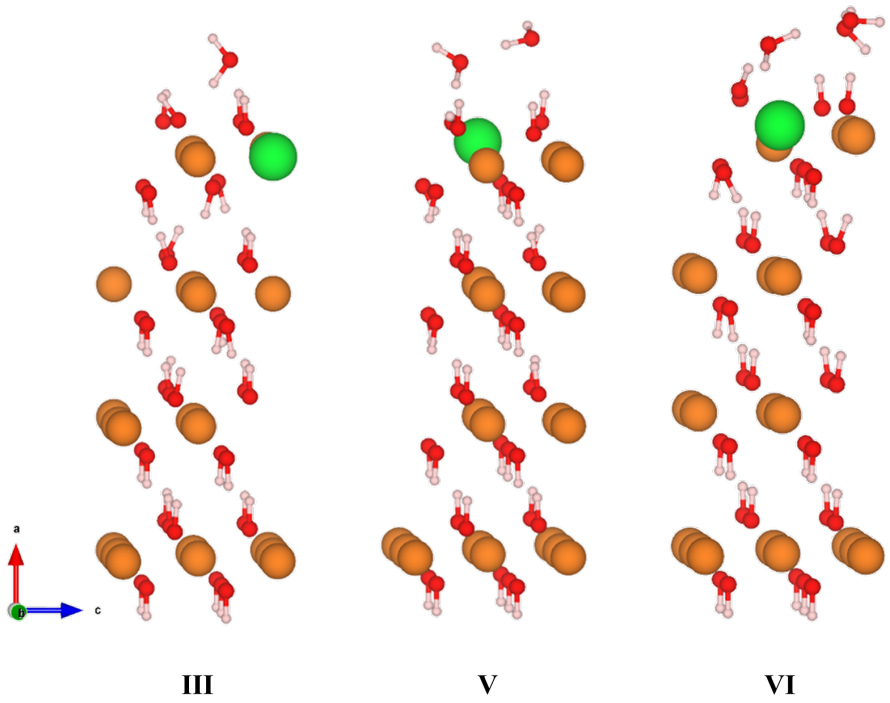

Figure B.12: {001} Surface doped with H_2O: III) 1H, V) 2H, VI) 3H and VII) 4H. Mg in orange, Sr in green, H in white and O in red.

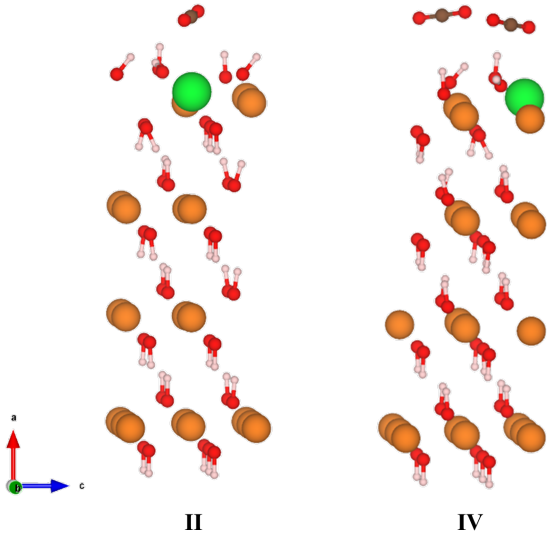

Figure B.13: {001} Surface doped with CO_2: II) 1C and IV) 2C. Mg in orange, Sr in green, C in grey, H in white and O in red.

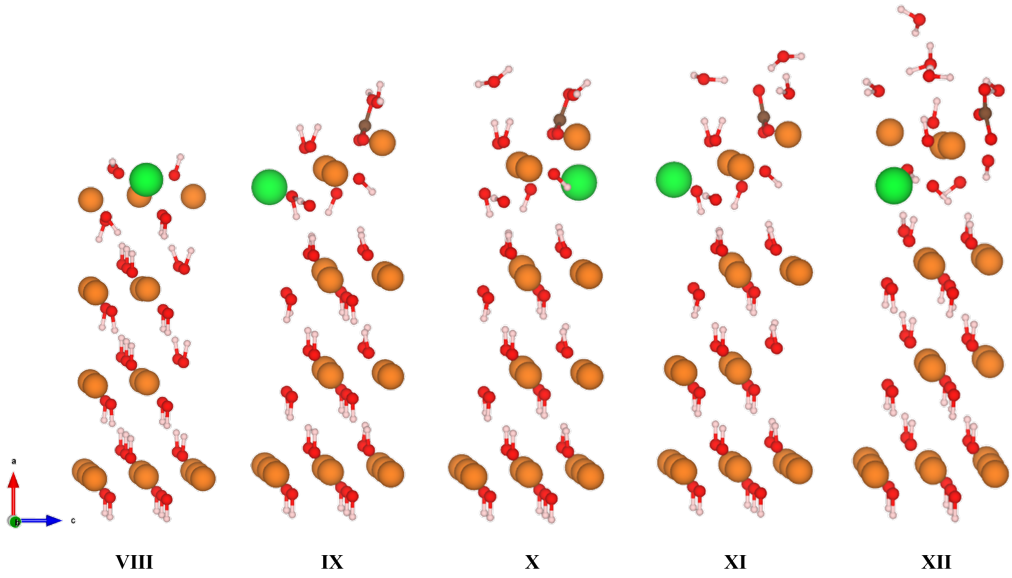

Figure B.14: {001} X1 surface including varying H_2O with 1 CO_2: VIII) X1, IX) X1-1C-1H, X) X1-1C-2H, XI) X1-1C-3H and XII) X1-1C-4H. Mg in orange, Sr in green, C in grey, H in white and O in red.

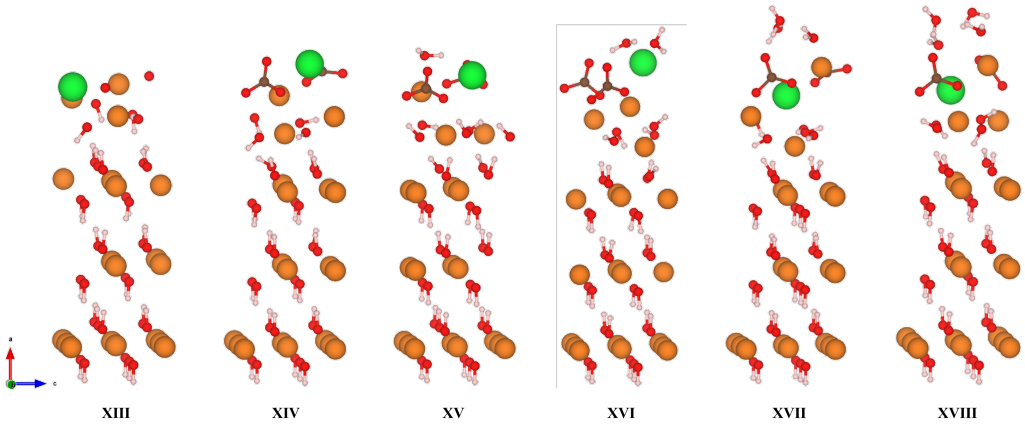

Figure B.15: {001} X2 surface including varying H_2O with 2 CO_2: XIII) X2, XIV) X2-2C, XV) X2-2C-1H, XVI) X2-2C-2H , XVII) X2-2C-3H and XVIII) X2-2C-4H. Mg in orange, Sr in green, C in grey, H in white and O in red.

B.4 {100} Surface Strontium Defect

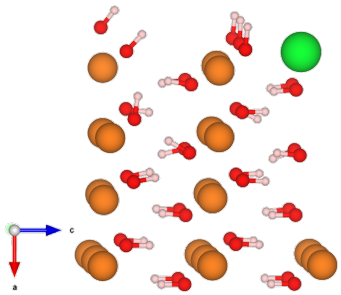

I

Figure B.16: {100} Surface (P): Mg in orange, Sr in green, H in white and O in red.

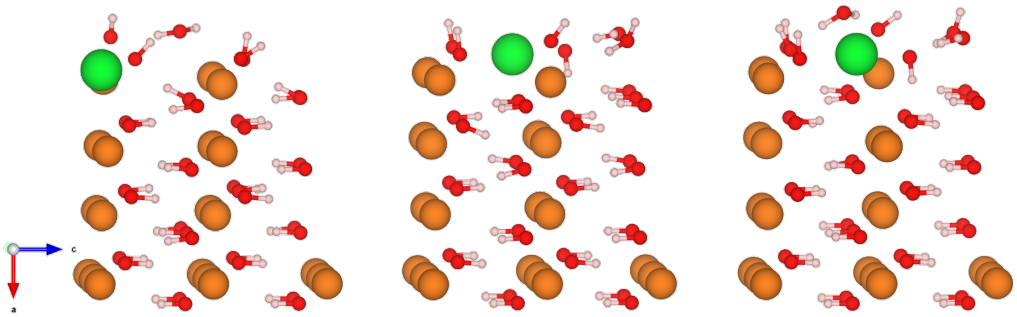

III V VI

Figure B.17: {100} Surface doped with H_2O: III) 1H, V) 2H, VI) 3H and VII) 4H. Mg in orange, Sr in green, H in white and O in red.

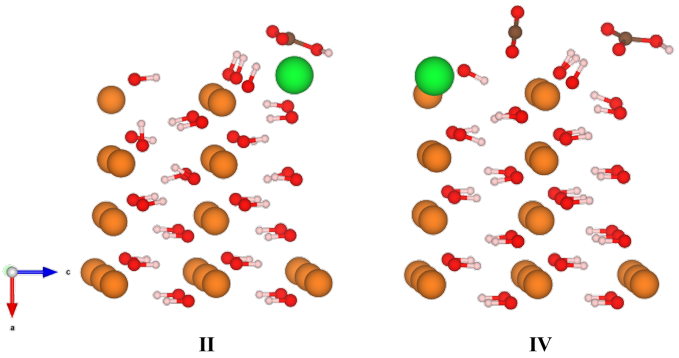

Figure B.18: {100} Surface doped with CO_2: II) 1C and IV) 2C. Mg in orange, Sr in green, C in grey, H in white and O in red.

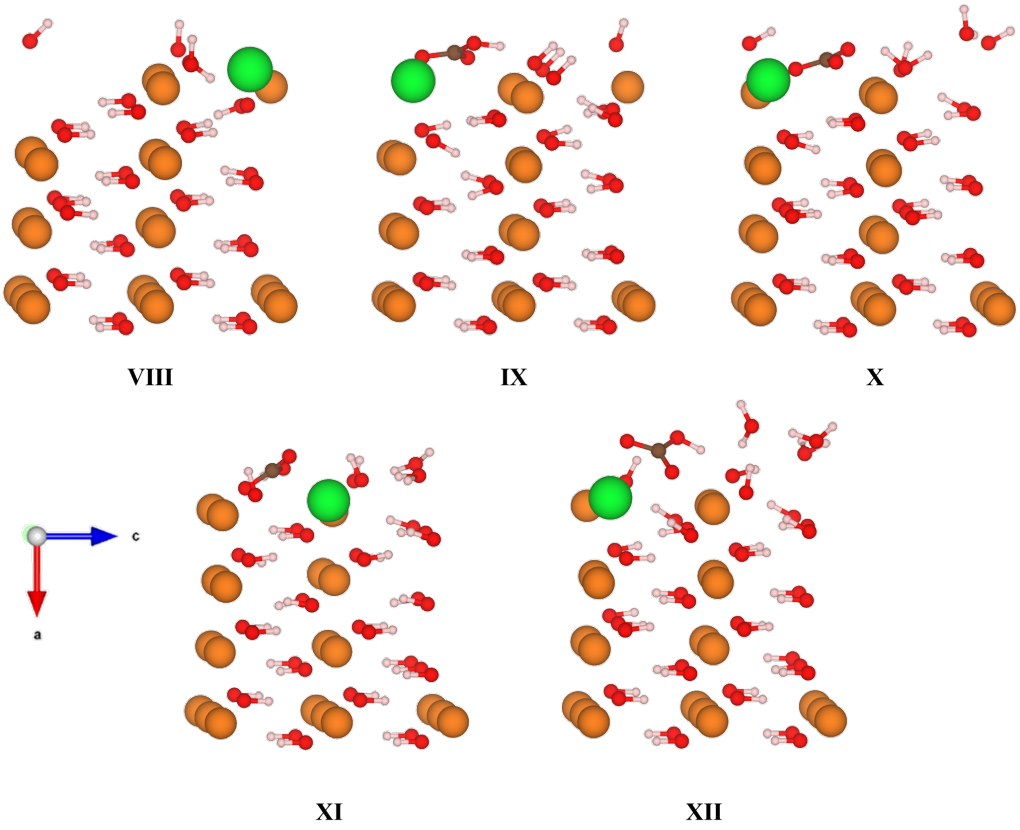

Figure B.19: {100} X1 surface including varying H_2O with 1 CO_2: VIII) X1, IX) X1-1C-1H, X) X1-1C-2H, XI) X1-1C-3H and XII) X1-1C-4H. Mg in orange, Sr in green, C in grey, H in white and O in red.

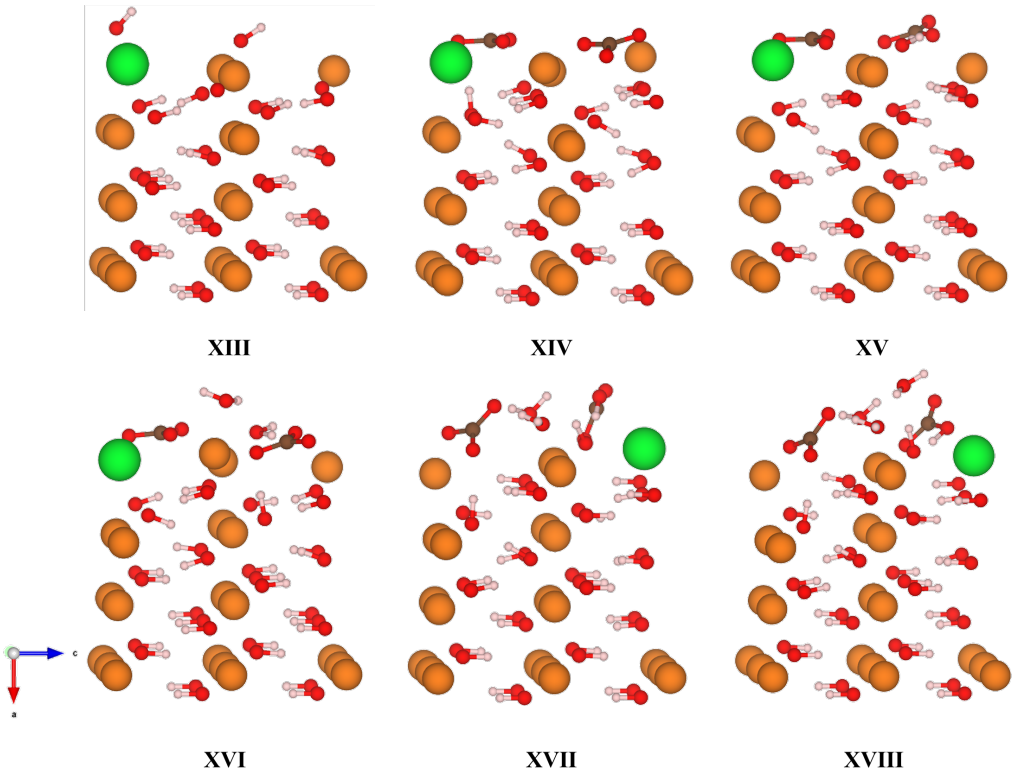

Figure B.20: {100} X2 surface including varying H_2O with 2 CO_2: XIII) X2, XIV) X2-2C, XV) X2-2C-1H, XVI) X2-2C-2H , XVII) X2-2C-3H and XVIII) X2-2C-4H. Mg in orange, Sr in green, C in grey, H in white and O in red.

B.5 Brucite Surface Phase Diagrams

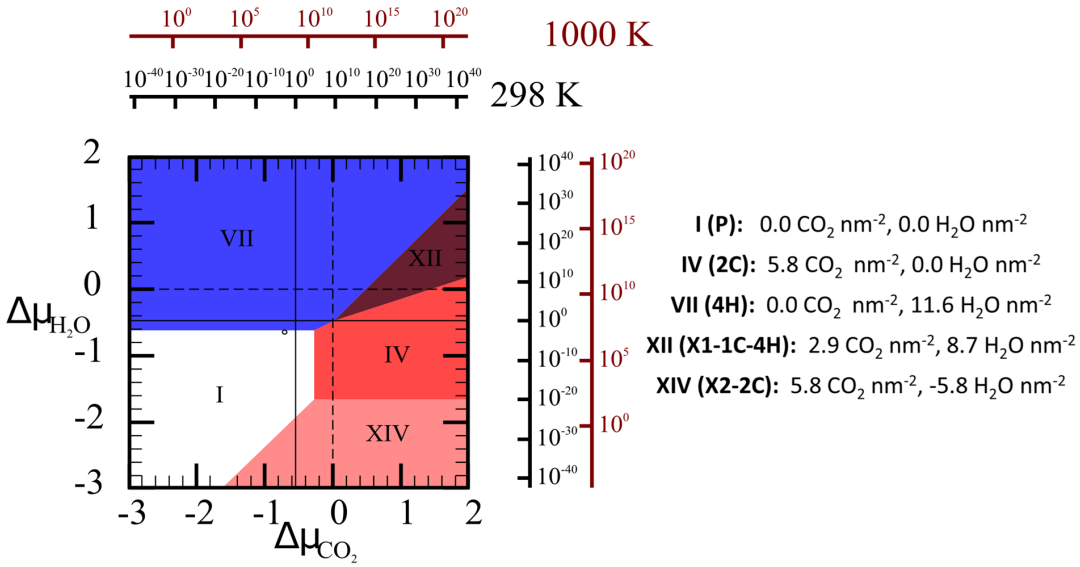

Figure B.21: {001} surface Phase Diagram calculated using optB86b-vdW, where the dashed line is 1bar pressure at 0K and the solid line is 1bar pressure at 298 K. White circle represents; 400 ppm CO_2 and 32 mbar of H_2O at 298 K (atmospheric conditions).

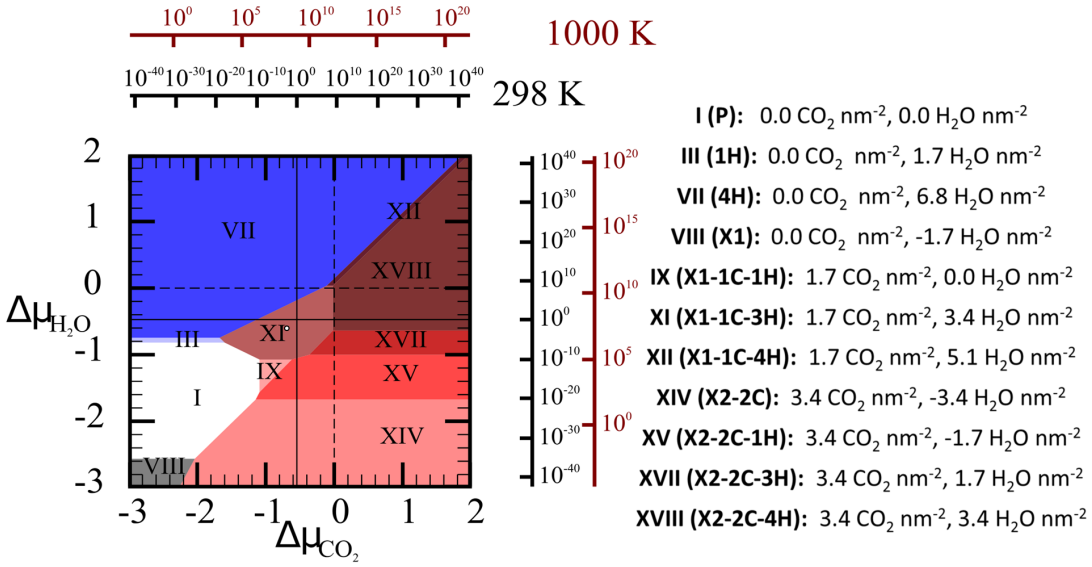

Figure B.22: {100} surface Phase Diagram calculated using optB86b-vdW, where the dashed line is 1bar pressure at 0K and the solid line is 1bar pressure at 298 K. White circle represents; 400 ppm CO_2 and 32 mbar of H_2O at 298 K (atmospheric conditions).

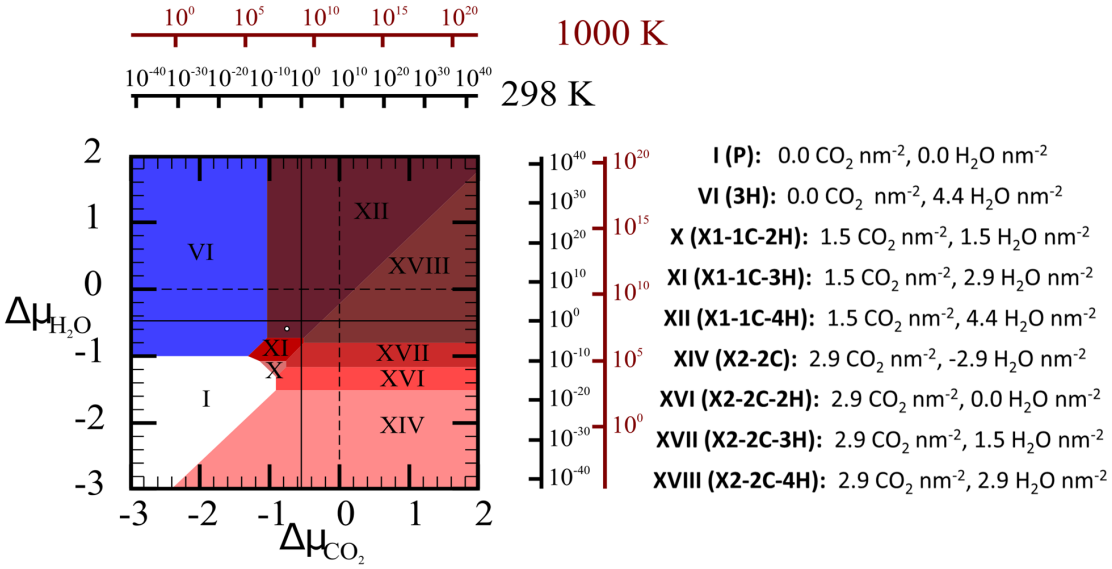

Figure B.23: {101} surface Phase Diagram calculated using optB86b-vdW, where the dashed line is 1bar pressure at 0K and the solid line is 1bar pressure at 298 K. White circle represents; 400 ppm CO_2 and 32 mbar of H_2O at 298 K (atmospheric conditions).

B.6 Strontium Doped Surface Phase Diagram

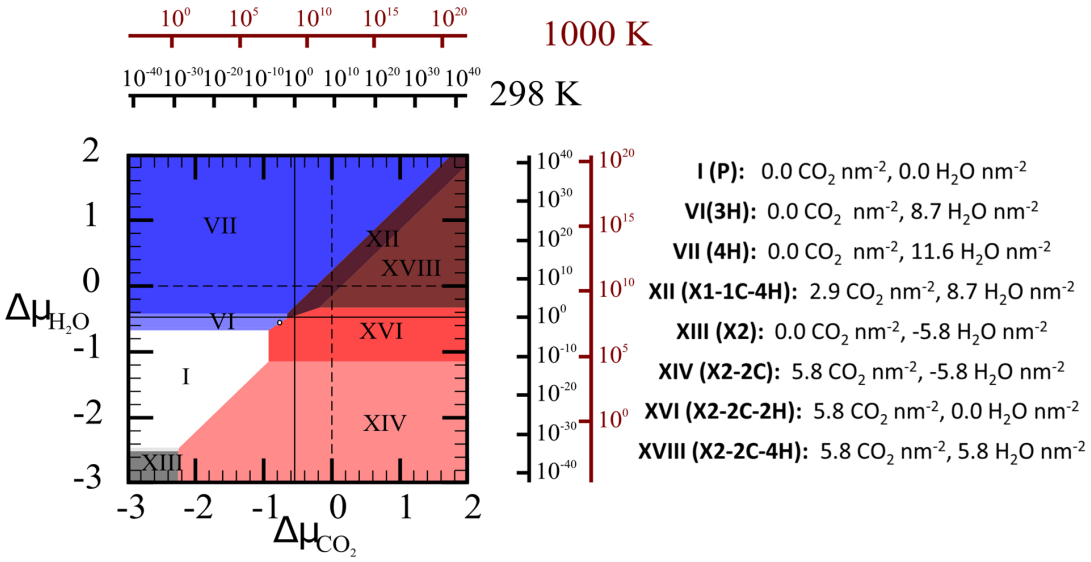

Figure B.24: {001} surface Phase Diagram calculated using optB86b-vdW, where the dashed line is 1bar pressure at 0K and the solid line is 1bar pressure at 298 K. White circle represents; 400 ppm CO_2 and 32 mbar of H_2O at 298 K (atmospheric conditions).

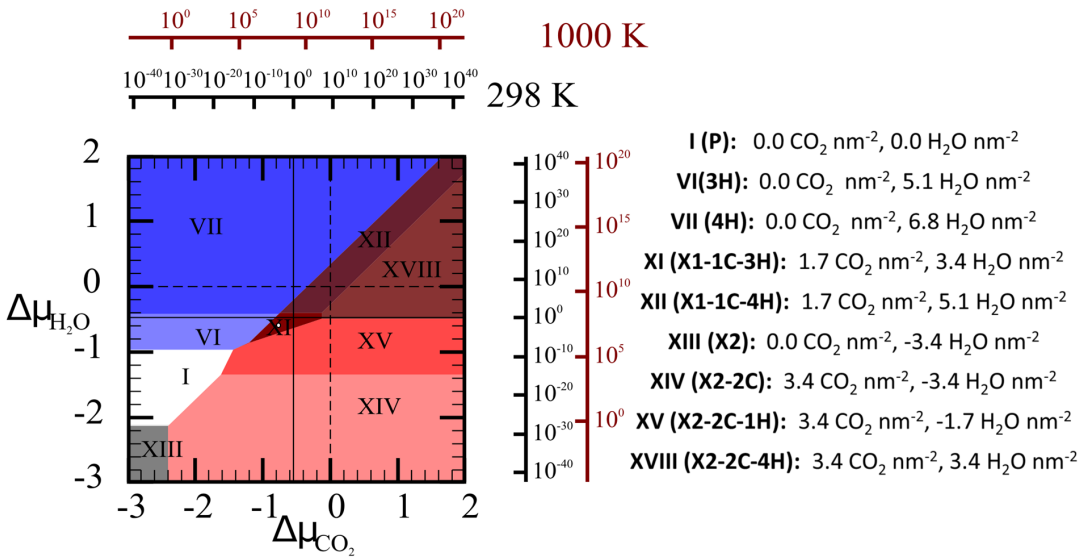

Figure B.25: {100} surface Phase Diagram calculated using optB86b-vdW, where the dashed line is 1bar pressure at 0K and the solid line is 1bar pressure at 298 K. White circle represents; 400 ppm CO_2 and 32 mbar of H_2O at 298 K (atmospheric conditions).

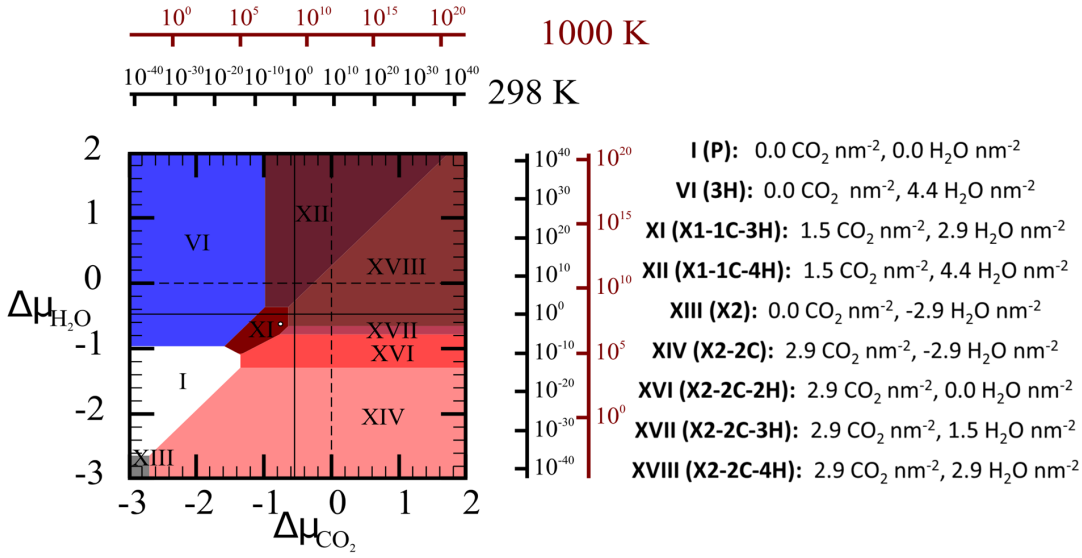

Figure B.26: {101} surface Phase Diagram calculated using optB86b-vdW, where the dashed line is 1bar pressure at 0K and the solid line is 1bar pressure at 298 K. White circle represents; 400 ppm CO_2 and 32 mbar of H_2O at 298 K (atmospheric conditions).